UNIVERSITY OF CALIFORNIA, SAN DIEGO

Solar Energy Resourcing and Forecasting for Optimized Grid Integration

A dissertation submitted in partial satisfaction of the
requirements for the degree
Doctor of Philosophy

in

Engineering Sciences (Mechanical Engineering)

by

Lukas Nonnenmacher

Committee in charge:

Professor Carlos F. M. Coimbra, Chair
Professor Jan Kleissl
Professor George R. Tynan
Professor David G. Victor
Professor Kraig B. Winters

2015

The dissertation of Lukas Nonnenmacher is approved, and it is acceptable in quality and form for publication on microfilm and electronically:

_____

_____

_____

_____

_____

Chair

University of California, San Diego

2015

DEDICATION

This dissertation is dedicated to Barbara, Lisa, Nora & Albert Nonnenmacher.

EPIGRAPH

The belief that one's own view of reality is the only reality is the most dangerous of all delusions.
— *Paul Watzlawick*

Use the power of the mind, it will make you fly.
— Otto Lilienthal

I'd put my money on the sun and solar energy. What a source of power! I hope we don't have to wait until oil and coal run out before we tackle that.
— Thomas Alva Edison

TABLE OF CONTENTS

LIST OF FIGURES

LIST OF TABLES

ACKNOWLEDGEMENTS

I feel very privileged to have worked with my academic adviser, Professor Carlos F. M. Coimbra. In 2010, he gave me the opportunity to work with him for five months at University of California, Merced and supported me and my ideas ever since. I would like to thank my committee Jan Kleissl, Gorge R. Tynan, David G. Victor, and Kraig Winters for providing support and sharing thoughts on how to develop this work. Many insights occurred during discussions with other group members, namely Amanpreet Kaur, Rich H. Inman, Hugo T.C. Pedro, David Larson and Athanassios Zagouras. Thanks for this support. I thank Prof. Frank Behrendt for supporting me in my transition form the TU Berlin to California and Dr. Andreas Arlt from EnBW for sparking my interest in solar energy. Additionally, I would like to express my gratitude to Matthias Müller, for 13 years of shared class experience and providing support throughout. Warm thanks go to Christian Tomp for assisting me in the first years of college and continuously sharing well-kept notes. Several last-minute crash courses from Dr. Lisa Abele and Dr. Anja Müller helped to pass exams against the odds. Last but not least, special thanks go to Pedro F. Navarro, Daniele Cavaglieri, Andres I. Cortes, Alexander J. Cooper and Ricardo Medina for keeping me sane in San Diego and sharing all the fun times.

This dissertation contains parts of the following publications with Amanpreet Kaur and Carlos F.M. Coimbra as co-authors:

- L. Nonnenmacher, A. Kaur, C. F. M. Coimbra, "Day-Ahead Resource Forecasting for Concentrated Solar Power Integration", (submitted), *Renewable Energy*, Apr. 2015.

- L. Nonnenmacher, A. Kaur, C. F. M. Coimbra, "Benchmarking and Valuation of Day-Ahead Forecasts for Direct Normal Irradiance", (submitted), *Solar Energy*, submitted, Oct. 2014.

- L. Nonnenmacher, C. F. M. Coimbra, "Streamline-Based Method for Intra-Day Solar Forecasting Through Remote Sensing", *Solar Energy*, 108, pp. 447-459, 2014.

- L. Nonnenmacher, A. Kaur and C. F. M. Coimbra, "Verification of the SUNY direct normal irradiance model with ground measurements,", *Solar Energy*, pp. 246-258, 2014.

- L. Nonnenmacher, "Implementing a Solar Radiation Measurement Network in California and Data Quality Assessment" - Diplomarbeit, *Technische Universität Berlin, Fakultät III*, 2011.

The specific publication from where content was used can be found at the end of each chapter.

VITA

2011	Dipl.- Ing. in Mechanical Engineering, Technical University of Berlin, Germany.
2015	Ph.D in Engineering Sciences (Mechanical Engineering), University of California, San Diego.

PUBLICATIONS

L. Nonnenmacher, A. Kaur, C. F. M. Coimbra, "Day-Ahead Resource Forecasting for Concentrated Solar Power Integration," (submitted), *Renewable Energy*, Apr. 2015.

L. Nonnenmacher, A. Kaur, C. F. M. Coimbra, "Benchmarking and Valuation of Day-Ahead Forecasts for Direct Normal Irradiance," (submitted), *Solar Energy*, submitted, Oct. 2014.

L. Nonnenmacher, C. F. M. Coimbra, "Streamline-Based Method for Intra-Day Solar Forecasting Through Remote Sensing," *Solar Energy*, 108, pp. 447-459, 2014.

L. Nonnenmacher, A. Kaur and C. F. M. Coimbra, "Verification of the SUNY direct normal irradiance model with ground measurements," *Solar Energy*, pp. 246-258, 2014.

A. Kaur, L. Nonnenmacher, H. T. C. Pedro, C. F. M. Coimbra, "Benefits of Solar Forecasting for Energy Imbalance Markets," (submitted), *Renewable Energy*, Mar. 2015.

A. Kaur, L. Nonnenmacher, C. F. M. Coimbra, "Net Load Forecasting for High Renewable Energy Penetration Grids," (submitted), *Energy*, Dec. 2014.

Y. Chu, H. T. C. Pedro, L. Nonnenmacher, R. H. Inman, Z. Liao, and C. F. M. Coimbra, "A Smart Image-Based Cloud Detection System for Intra-Hour Solar Irradiance Forecasts," *Journal of Atmospheric and Oceanic Technology*, pp. 1995-2007, 2014.

ABSTRACT OF THE DISSERTATION

Solar Energy Resourcing and Forecasting for Optimized Grid Integration

by

Lukas Nonnenmacher

Doctor of Philosophy in Engineering Sciences (Mechanical Engineering)

University of California, San Diego, 2015

Professor Carlos F. M. Coimbra, Chair

Solar and wind energy have the potential to power the world's energy needs. However, the variable and uncertain power generation from these sources are posing a major challenge for the reliable and economic integration in the existing electric power system. For solar energy, the problem consists of two related parts, (1) variability in the resource (determined by the location of a solar plant) and (2) uncertainty in power output, (determined by the local meteorological conditions). First, this work presents a verification of the accuracy of satellite image based irradiance models, used to globally assess the solar resource. The focus is placed on the direct normal irradiance (DNI) component of solar radiation and its variability. Second, we develop two solar forecasting methods, necessary for grid integration

and market participation of solar energy generators. For intra-day forecasting, a satellite imagery based global horizontal irradiance (GHI) forecast methodology is proposed. For day-ahead forecasting, we present a numerical weather prediction (NWP) based model to predict hourly values of DNI, necessary for power output scheduling of concentrated solar power (CSP) plants. The proposed day-ahead forecast is extensively validated for regions in North America with high and medium potential for the deployment of CSP. The benefits of this forecast for large scale grid integration of CSP plants, combined with optimized siting to reduce variability and uncertainty, are shown. Results include the quantification of errors in satellite based DNI assessment, the successful application of cloud tracking in satellite images for forecasts up to 3h ahead and the significant reduction of power output uncertainty for day-ahead market participation of CSP plants.

Chapter 1

Introduction

Electricity generation from renewable sources, such as wind and solar, showed remarkable growth rates in the last decades. This paradigm shift to clean energy generation has many rationals behind it, most notably the reduction of emissions, regional self-sufficiency and the general advances to decentralize energy systems. Solar and wind power are intermittent in nature, causing challenging integration and reliability characteristics which demand technically complex and costly solutions. Additionally, the resource availability and intermittency for both, the solar and the wind resource, are strongly dependent on location specific meteorological characteristics. In many regions in the United States, solar power generation has a significantly higher potential than wind [83], with political incentives that promote large scale deployment [123]. Hence, we expect that the impact of renewable resource intermittency on the power grid will increase and needs to be addressed, especially with regards to solar. The mitigation of the impact of solar power variability is the main driver behind the research presented in this dissertation.

The location specific resource variability is determined with the siting decision for solar power generators. Highly accurate resource assessment tools are required to compare potential sites with regards to variability and technology choices. The acquisition of ground data and the accuracy assessment of remote sensing based irradiance models is the first of three main parts of this work. Besides siting optimization, many concepts to mitigate the negative impact of intermittency were

proposed and are subject to current research, for example: increased storage; demand side management; increased ramping capabilities of conventional plants; and increased operating reserves. Beside these solutions, power resource forecasting has gained attention in the past decades. On the background of large-scale wind integration in many regions in Europe, wind speed forecasting started to evolve as a rewarding topic in academia and the power industry. Early advances to forecast the wind resource emerged around the 1970s [122], as reported in [17]. Since then, continuous improvements based on a broad variety of models were made [56]. Solar forecasting dates back to the 1980s, notably advanced by studies from J. Jensenius (1981 & 1989) [54, 53], B.H. Chowdhury (1987) [14] and P.W. Heck (1987) [41], as reported in [42]. Revisiting the literature, the oldest reference on forecasting of solar radiation data appeared in 1977 and outlines the application of stochastic time series modeling in a technical note [28]. Many solar resource forecasting methodologies were proposed since then and most authors agree that different forecast horizons require different methodologies [68, 101, 12, 73, 52, 106, 63]. Forecast horizons below 1 hour typically require ground based sky imagery and sophisticated time series and machine learning models. These intra-hour forecasts advanced the most in recent years, mainly based on significant advances in ground based sky image acquisition and improved modeling techniques [13, 25, 74, 22, 39].

Intra-day horizons, normally forecasting irradiance values up to 4 or 6 hours ahead, require satellite images and irradiance models [80, 76]. Forecast horizons exceeding 6 hours usually rely on outputs from numerical weather prediction (NWP) models. Intra-day and day-ahead forecasts are crucially important for energy trading schedules. Nevertheless, these forecast horizons gained little attention in the past. This dissertation attempts to fill into this gap and presents methods to forecast solar irradiance 1-3 hours and 12-72 hours ahead. Intra-day and day-ahead solar forecasts are the second and third main parts of this work. This dissertation is structured as follows: Chapter 2 covers the instrumentation for ground based solar resource assessment. Chapter 3 is dedicated to remote sensing based resource assessment and especially covers the validation of modeling solar resource variability. Chapter 4 presents an intra-day solar forecast based on advanced satellite image

processing. Two models to forecast direct normal irradiance (DNI) are compared in Chapter 5 and optimized in Chapter 6. Chapter 7 describes the implications of the optimized forecasts for the integration of concentrated solar power (CSP) in the electric grid. Chapter 8 contains the conclusions of this dissertation.

Chapter 2

Solar resourcing

Solar energy power plants are designed, sized and optimized based on the availability of the solar resource at the site of deployment. Hence, it heavily relies on short and long term weather fluctuations and seasonal cycles. The most accurate approach to solar resource assessment is based on ground measurements, especially with regards to the location specific variability and uncertainty. To understand the process of ground based solar resource assessment, this chapter describes the physical characteristics of solar irradiance, the available instrumentation as well as the deployed solar observatories.

2.1 Solar irradiance

Solar irradiance at the top of the atmosphere can be considered constant, with an estimated value of 1366.1 Wm^{-2} and $\pm 3.4\%$ variation due to changes in the Sun-Earth distance [30]. If solar radiation propagates through the atmosphere, it interacts with atmospheric molecules causing absorption and scattering. Molecular scattering (also referred to as Rayleigh scattering) causes diffuse radiation (DIF). Radiation, measurable on a horizontal surface is called global horizontal irradiance (GHI). The unobscured beam, directly passing trough the atmosphere, is called the beam (B) or direct normal irradiance (DNI). (Note: the fact that DNI is measured normal to the beam is crucial. Ambiguity errors are frequent since the term direct irradiance occasionally refers to the part of global horizontal irradiance coming

directly from the Sun, measured on a non-inclined surface. Hence, this would represent the global horizontal irradiance minus the diffuse irradiance (GHI-DIF). To avoid ambiguity, DNI, B and direct irradiance are used as synonyms. The other definition of direct irradiance is never used in this work.)

In general, PV applications rely on GHI, while all concentrating solar power technologies rely on DNI. Figure 2.1 is an illustration of the atmospheric effects on radiation. The relation between solar irradiance components can be approximately calculated by:

$$GHI = DNI \cdot cos(\theta) + DIF, \tag{2.1}$$

where θ indicates the incidence angle.

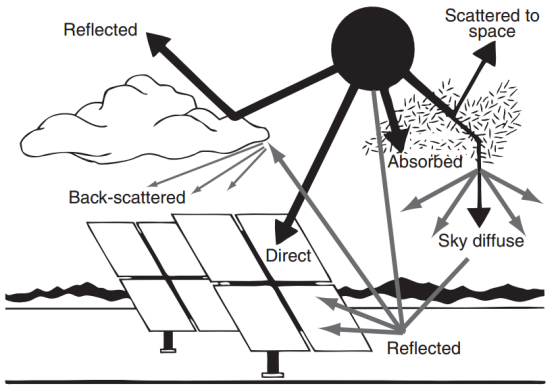

Figure 2.1: Illustration of the atmospheric effects on radiation, causing decomposition into global horizontal irradiance (GHI), direct normal irradiance (DNI) and diffuse irradiance (DIF) (illustration from [1])

2.2 Instrumentation

The following instruments are deployed to measure the different components of solar irradiance. The descriptions are included for completeness and resemble parts from [89].

2.2.1 Pyranometer

A pyranometer measures GHI or DIF, depending on if a shading device is used or not. Highly accurate pyranometers use thermal detectors. Thermal detectors (thermopiles) sense temperature variations between a surface exposed to radiation and a neutral sensor. The thermopile deployed in a pyranometer receives the measured irradiation from the entire 180° dome of the hemisphere, protected against the environment by a characteristic glass dome. High quality glass domes are transparent to up to 250 nm - 4500 nm radiation. The deployed precision spectral pyranometer from the make Eppley meets the accuracy specifications to be a a first class radiometer by World Meteorological Organization Standards (see figure 2.2). Photodiode detectors are available as well, but are mostly for budget constrained or short term studies, since the accuracy of photodiode sensors decays over time.

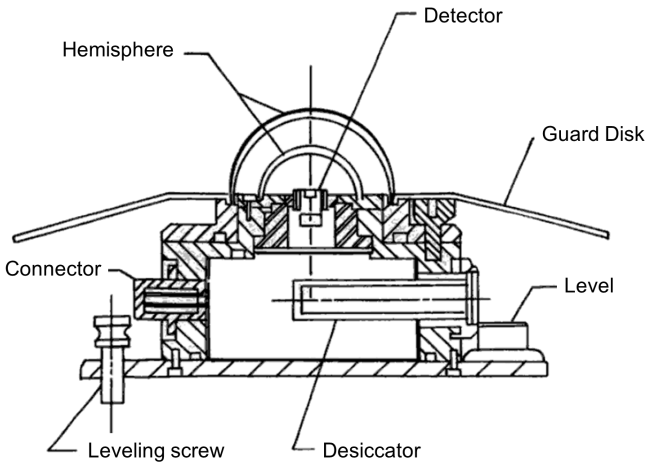

Figure 2.2: Cross section of an Eppley precision spectral pyranometer to measure GHI (illustration from [118]).

2.2.2 Tracker

The device to measure DNI (pyrheliometer) has to be pointed directly to the Sun. For our solar observatories, an automatic solar tracker named SMT-

3 made by the Eppley Laboratories is used. This tracker is designed for up to two pyroheliometers and up to two PSP's and shading devices (to measure DIF). The tracker is controlled by a HP 200 LX palmtop computer calculating the current solar position after entering the longitude and altitude of the location with a QuickBasic program.

2.2.3 Pyrheliometer

DNI is measured with a pyrheliometer. While the sensor is a thermopile as for the described pyranometer, the design of the instrument is vastly different (see figure 2.3). Depending on the specific design, pyrheliometers have an aperture angle of between 5° and 6°. Through this narrow aperture, only the direct part of the radiation can penetrate the thermophile sensor. Hence, diffuse radiation is excluded from the irradiance and only the direct beam is measured. This is only possible if the pyrheliometer is pointed normal to the sun. This is achieved with a two axis tracker. For our observatroies, an Eppley Laboratory normal incidence pyrheliometer (NIP) are deployed. Figure 2.4 shows an operational setup from 1926 (Marvin pyrheliometer).

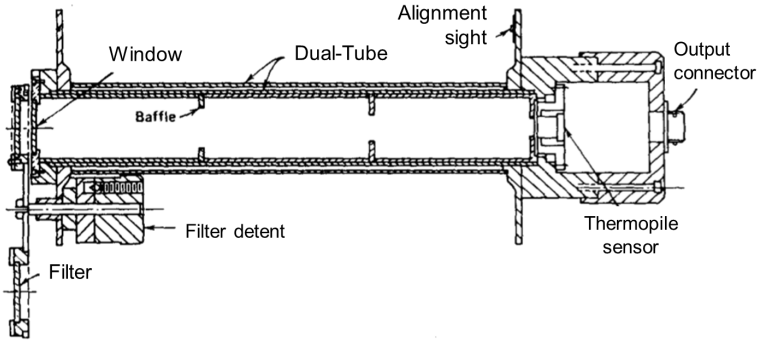

Figure 2.3: Cross-section of an Eppley normal incidence pyrheliometer to measure DNI [119].

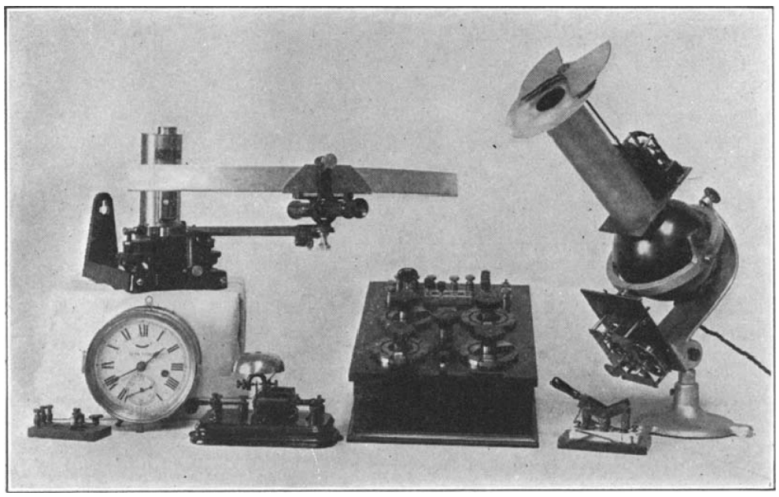

Figure 2.4: Picture of the Marvin pyrheliometer from 1926 [78].

2.2.4 MFR-7

A multi-filter radiometer (MFR-7) by the make Yankee Enviornmental Systems is used at some observatories. The advantage of a MFR-7 is that it measures global, diffuse, and direct solar radiation in only one device, with less moving parts than required for the tracker setup. It only has one rotating shadow-band, reducing maintenance and alignment requirements. The control unit of the device calculates the rotation of the shadow-band based on the location of the Sun and moves the shadow-band to the right position four times a minute. The first measurement of a cycle is made when the sensor is not shaded, assessing GHI. If the shadow-band shades the sensor, the DIF measurement is made (the direct beam is completely blocked from the sensor). Two more measurements are made when the shadow-band is rotated 9° to each side of the Sun. These two additional measurements are used to assess sky that is blocked while shaded. DNI is calculated according to equation 2.1 with additional corrections by the proprietary software embedded in the data logger [89]. The general error of this devices is below 5% for $0 - 80°$ Solar Zenith Angle (SZA) and below 1% with corrections applied [126]. The MFR-7 and the Eppley Setup were placed less than $5m$ apart.

2.2.5 Rotating shadow-band radiometer (RSR2)

This device follows the principle of the MFR-7 by periodically shading a pyranometer, but the deployed sensor is a photoiode (from the make LiCor model LI-200SZ). DNI values are calculated according to 2.1. Hence, DNI is an approximation rather than an accurate measurement. Figure 2.5 shows a scheme of the deployed instrument.

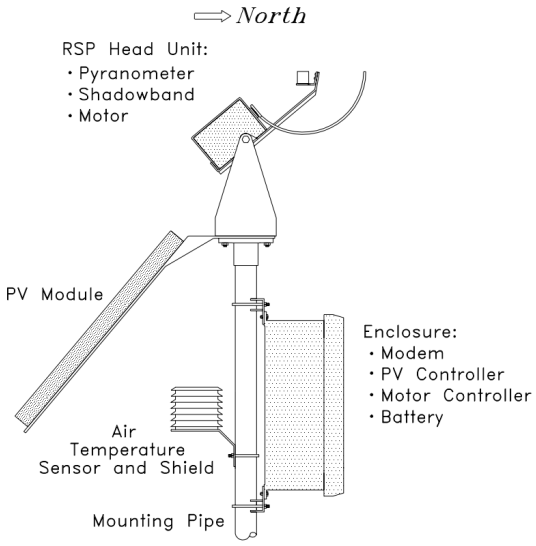

Figure 2.5: Scheme of the rotating shodowband radiometer (RSR2) by the make Irradiance Inc. [59].

2.3 Ground observatories

As mentioned earlier, high-quality DNI ground based measurements are notoriously sparse. DNI data from a two different networks of observatories maintained by NREL and UCSD are available and described below. Figure 2.6 shows all locations across the United States. All ground experiments are executed at the specified UCSD observatories. External data from the ISIS network is also used, especially in chapter 6.

Figure 2.6: Map of sites with ground DNI measurements. Red markers are Integrated Surface Irradiance Study (ISIS) locations. Data from NOAA is available online. Blue markers show UCSD DNI observatories. Exact coordinates and data set length are in table 6.1 (map from Openstreetmap contributors).

2.3.1 ISIS observatories

The Integrated Surface Irradiance Study (ISIS) network is part of a project to monitor surface radiation in the United States as part of a collaboration with the surface radiation budget measurement network (SURFRAD) from the National Oceanic and Atmospheric Administration (NOAA). The sampling rate of this data set is 3 minutes. Averages have been created where necessary. Details of this data set and the applied data quality control is described in [43]. The ISIS network also acquires DNI data at Bismarck, North Dakota; Madison, Wisconsin; Seattle, Washington and Sterling, Virginia but these sets are not considered since CSP deployment in those regions is unlikely. Tallahassee, Florida was excluded due to a lack usable data. Table 6.1 summarizes the ground data sets and figure 2.6 shows the locations.

2.3.2 UCSD observatories

Ground DNI measurements have been obtained from the network of solar observatories deployed and maintained by the University of California, San Diego (UCSD) at four locations in California, namely Merced, Berkeley, Davis and San Diego. Data was acquired with MFR-7 instruments by the make Yankee Environmental Systems. The applied data quality control is described in [92]. Table 6.1 describes the solar observatories maintained by the Center for Energy Research at UCSD. The locations of these observatories are represented with blue markers in figure 2.6.

2.3.2.1 Merced

The Merced solar observatory is located on the University of California (UC) Merced campus (latitude: 37.36; longitude: -120.42). The Köppen climate classification scheme describes the climate as *Csa* (main climate C=warm, precipitation s=steppe and temperature a=hot summer) based on [60]. These climate conditions are characterized by hot, dry summers and wet, cold winters. Merced is located close to the geodesic center of California. A weather phenomenon in this area is the occurrence of tule fog, a dense formation of ground fog that can be observed frequently between November and April and that causes significant ground cooling and drizzling conditions. Data sets in Merced were collected from April 2010 until May 2012 by a setup of two Eppley Precision Spectral Pyranometers and an Eppley Normal Incidence Pyrheliometer (NIP). One pyranometer is used to measure GHI. The second pyranometer is mounted on an Eppley Tracker (Model SMT-3) with a shade disk kit to measure DHI. The same tracker carries the NIP to measure DNI. Data sets were logged every second with a Campbell Scientific CR-1000 data-logger and saved as 30 second average values. The calculated system accuracy for each component of this setup is $\pm 1.6\%$ given perfect alignment and cleanliness (for details, see [9]).

Additionally to the Eppley setup, a MFR-7 was deployed in Merced from March 2011 until May 2012. Besides the solar observatory, a 1 MW solar photovoltaic (PV) farm is also available on the campus. The solar array consists of $4,900$

mono-crystalline silicon, single-axis tracking PV panels. Power output data from the solar farm were recorded as 15 minute averages. To match this resolution with the SUNY data, 30-minute averages were calculated.

2.3.2.2 San Diego

There are two solar observatories located at the University of California, San Diego campus in La Jolla, CA. Both are on rooftops (latitude: 32.88; longitude: -117.23), approximately 100m apart. The San Diego DNI solar observatory was established in March 2012 and includes two MFR-7s as well as two full setups of Eppley instruments (including two pyranometers and a pyrheliometer, mounted on two independent trackers). The climate in La Jolla can be described as semi-arid with inherently large variations over short distances due to the topography of the coastal region, leading to distinct microclimates in close proximity. The sensors are located within 2 km of the coastline, on about 100 m elevation above the mean sea level. Therefore, they lie well within the region influenced by coastal marine layer clouds. Under certain conditions, these marine layer clouds form over the Pacific Ocean and advect onshore, where they can remain for days, a distinctive feature of the La Jolla region from May through August. Based on the Köppen climate classification scheme this location is either referred to as *BSk* (B=arid, S=steppe, k=cold arid) or *Csa*. At these sites, shading occurs during partial times of the year. Days with shading have been removed entirely from the analysis. The devices have been checked for alignment and cleanliness several times per week. Figure 2.7 and 2.8 show images of the observatories in San Diego.

2.3.2.3 Davis

Data at the location in Davis was acquired with a MFR-7 (latitude: 38.53; longitude: -121.78). Data was collected from May 2011 until September 2012. Located in the northern portion of the Central Valley of California, the climate in Davis is similar to Merced (also characterized as *Csa* on the Köppen scheme). Davis is a remote location with no on-site staff, therefore we expect soiling effects over time.

Figure 2.7: Solar observatory at UCSD on the $CalIT^2$ building. The Eppley tracker on the left carries a pyrheliometer, a pyranometer and a precision infrared radiometer with a shade disk kit. Additionally, a sun facing camera (Vivotek FE8171V) was installed on the tracker for sky imagery. On the right, an MFR-7 is installed (middle). The device on the right is a fisheye-lens sky camera.

2.3.2.4 Berkeley

The Berkeley solar observatory is located on the University of California, Berkeley campus on top of a building (latitude: 37.88; longitude: -122.26). The climate is often referred to as *Csb* on the Köppen scheme (C=warm temperature, S=steppe, b=warm summer). However, summers tend to be cooler than for typical Mediterranean climate due to the closeness to the San Francisco Bay. Additionally, the proximity to the ocean causes frequent coastal fog and light rain (see, e.g. [26] for more details). As the other locations, the Berkeley observatory is equipped with a MFR-7. Data collection at this locations started in May 2011. Although only 90 km apart, ground irradiance at Berkeley differs substantially from the ground irradiance at Davis. Due to suspected misalignment of the Berkeley MFR-7, data from 01 August 2011 to 04 September 2011 have been removed from this analysis.

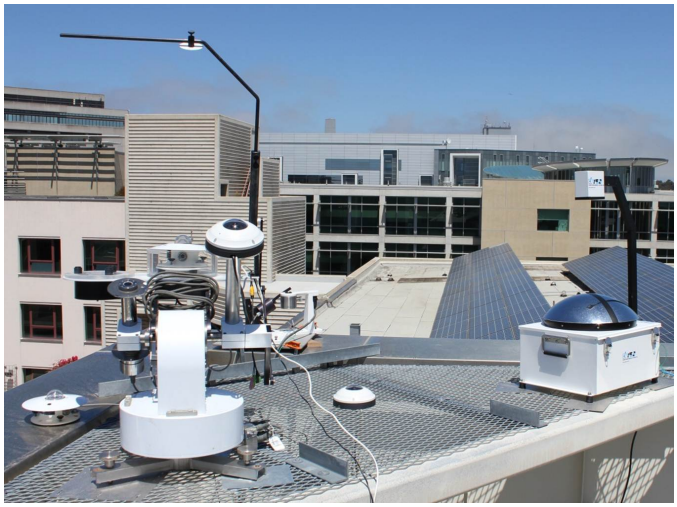

Figure 2.8: Solar observatory at UCSD on the EBU-II building. A pyranometer to measure GHI is located on the very left. The Eppley tracker carries a pyrheliometer and a pyranometer as well as a sun facing camera (Vivotek FE8171V). Behind the tracker, a MFR-7 is placed (shading does not occur). Additionally, a fish-eye camera and sky imager can be seen.

2.3.2.5 Folsom

At the observatory in Folsom (latitude: 38.64; longitude: -121.14), a rotating shadow-band radiometer (RSR-2 from the make Irradiance Inc.) is installed. The deployed PSP follows the principle of the MFR-7 with periodically shading a pyranometer, but the deployed sensor is a photodiode (from the make LiCor model LI-200). DNI values are calculated according to 2.1. Hence, DNI is an approximation rather than an accurate measurement. Data from the Folsom observatory is not included in the evaluation below since the DNI measurements do not meet the accuracy standards.

2.4 Summary

This chapter provided the physical background of ground based solar resource assessment with regards to high-quality measurements. The efforts necessary to measure DNI are significantly higher than for GHI, mainly due to the

required Sun tracking and the resulting moving parts in the environment. Hence, ground measured GHI data is more available than high quality DNI ground truth data. This implies that the uncertainty in resource assessment for PV plants is generally lower then for CSP technologies. Several ways to reduce the complexity of DNI assessment are provided with the MFR-7 and the RSR devices. To address the lack of high quality ground measurements, five observatories were equipped with GHI, DNI, DIF and sky imaging devices. Furthermore, data from four externally maintained observatories in the United States was acquired. The inherent shortcomings of ground-based assessment motivated the development of several remote sensing techniques to model solar irradiance at the ground level. In North America, data for all three irradiance components from a satellite models is publicly (low-resolution) and commercially (high-resolution) available. In the next chapter, the satellite model for DNI is validated with the acquired ground data, discussed in this chapter.

Note: This chapter contains work, previously published in:

- L. Nonnenmacher, A. Kaur, C. F. M. Coimbra, "Day-Ahead Resource Forecasting for Concentrated Solar Power Integration", (submitted), *Renewable Energy*, Apr. 2015.

- L. Nonnenmacher, A. Kaur and C.F.M. Coimbra "Verification of the SUNY direct normal irradiance model with ground measurements,", *Solar Energy*, pp. 246-258, 2014.

- L. Nonnenmacher, "Implementing a Solar Radiation Measurement Network in California and Data Quality Assessment" - Diplomarbeit, *Technische Universität Berlin, Fakultät III*, 2011.

Chapter 3

Satellite model verification

As discussed above, solar irradiance instrumentation is costly and challenging to maintain, especially with regards to DNI and remote locations. Satellite models provide an opportunity to fill in the gap caused by spare ground measurements. Several satellite-to-irradiance models were developed in the past, including the Heliosat Model, BRASIL-SR Model, DLR-SOLEMI Method and the SUNY model, discussed in [10], [97], [110] and [100]. These different models emerged based on different characteristics of geostationary satellites covering different regions on the globe. All these models are cognate and mainly take different technical specifications of the satellites into account to fine tune the irradiance models. North America is covered by the GOES-West and GOES-East satellite series. The SUNY model was specifically developed as the satellite-to-irradiance model for these satellites.

3.1 Satellite models for irradiance

In general, satellite-to-irradiance models utilize observed cloud reflectivity and atmospheric conditions in combination with a clear sky model, requiring additional inputs like the Aerosol Optical Depth (AOD), elevation, ozone and water vapor. Since ground-based GHI measurements are more available than DNI measurements, many previous studies focused on the verification of accuracy of the GHI component [121, 93, 35, 21]. In contrast, the performance and characteristics

of the satellite-to-irradiance models for DNI are still poorly validated, particularly with regards to variability. Especially in California, the importance of reliable DNI data is evident because of its potential for Concentrated Solar Power (CSP) deployment in proximity to population centers ([114]). This chapter fills in this gap by providing an assessment of the DNI modeling accuracy of the SUNY model with ground truth data. This verification includes the evaluation of modeling solar variability for given locations. A more detailed quantification of solar variability became more important in recent years due to its significance for grid integration at higher penetration levels, e.g design of smart inverters, transmission analysis as well as the sizing of ancillary and spinning reserves ([95], [44], [74], [6]). Additionally, the performance and evaluation of solar forecasting technologies are strongly dependent on local solar variability [75].

3.1.1 SUNY model data

Data for this study was provided by SolarAnywhere® for all of California (Enhanced Resolution, (spatial: 1 km, temporal: 30 minutes)) as gridded data. Time series for the locations mentioned above have been extracted by taking the data of the pixel representing the area on the ground that includes the sensor for the ground truth measurements. For this study, SUNY data was available from January 2011 until September 2012.

3.2 Ground truth quality control

3.2.1 Operational errors

Quality Control for solar irradiance was discussed in-depth by several authors. The following sources that introduce errors into solar radiation measurements: (1) cosine response of the sensor, (2) azimuth response of the sensor, (3) temperature response of the sensor, (4) spectral selectivity, (5) stability, (6) nonlinearity of the sensor response, (7) shading band or kit misalignment and (8) dark offset long wave radiation error [127]. All of these errors are addressed by

the design of the measurement instruments. ISO 9060 provides specification and classification for GHI and DNI instruments and distinguishes between three quality grades for radiometers: secondary standard, first class and second class (ISO 9060 section 4.3.2). These are compliant to classifications made by the World Meteorological Organization (WMO). All instruments used to verify the satellite to irradiance model meet the highest standards. To address the well known issues with the cosine response of sensors and to exclude night values from the analysis, data collected during times when the solar elevation was below 5° has been excluded from the data sets.

In addition, [127] identified the most common operation related problems and errors as: (1) Complete or partial shade-ring misalignment, (2) Dust, snow, dew, water-droplets, bird droppings, etc., (3) Incorrect sensor leveling, (4) Shading, (5) electric fields in the vicinity of cables, (6) mechanical loading of cables, (7) orientation and/or improper screening of the vertical sensors from ground-reflected radiation and (8) station shut-down. The likelihood of occurrence of any of these disturbances have been minimized by a careful installation at all the locations and a regular maintenance.

3.2.2 Post-measurement quality control

In addition to the pre-measurement error minimization procedures, a post-measurement quality control is necessary in order to exclude compromised measurements. Two methods are used, ground truth assessment with redundant DNI measurements in Merced and a semi-automatic QC methodology proposed by [55] for the other locations.

3.2.3 Redundant measurements (ground truth)

To ensure the highest data quality, the values measured with the Eppley instruments were compared with the measurements from the MFR-7 deployed at the same location (la Jolla). Measurements with differences in half hourly

averaged values larger than 5% were flagged and excluded from the data sets. 5% was chosen as the sum from the 2.6% error introduced by the NIP and the MFR-7 instruments plus a systematic bias of 2.4% to allow for short time shading, horizontal misalignment or error due to spatial distance and soiling effects. A scatter plot of the ground truth DNI data for Merced, is shown in Fig. 3.1 (grey markers), combined with DNI data from the SUNY model (blue markers). We consider the strongly redundant data sets as ground truth measurements.

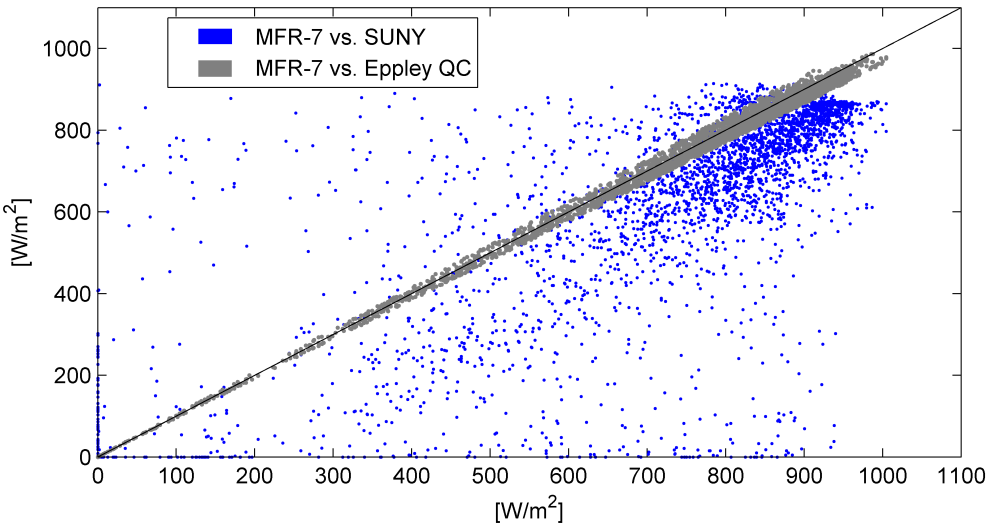

Figure 3.1: Scatter plot of MFR-7 ground truth data versus SUNY modeled DNI data for the quality controlled data set in Merced. Ground values with a difference larger than 5% of MFR-7 and Eppley setup measurements have been removed from the study. The black diagonal line has been added to show the 1:1 relationship.

3.2.4 Semi-automatic quality control

Since it is very rare that redundant ground data measurements are available at the same location, highly accurate data quality control options or usually not available. To address this, [55] proposed various procedures for post-measurement data quality control not based on redundant measurements. These procedures include physical threshold tests, step, persistence, quality envelope, spatial consistency, and sunshine tests. When applicable, these tests were implemented into a

post-measurement data quality control algorithm and were applied here. Several tests have not been used because they addressed problems that did not apply to our ground measurements (e.g to detect snow cover events). The following instrument characteristic issues were addressed manually before application of the quality control algorithm.

3.2.5 Instrument characteristics

MFR-7

The two most common sources for the MFR-7s, are shadow-band malfunction and horizontal misalignment. If the shadow-band does not shade the sensor correctly, the DHI is not measured correctly, leading to an error in DNI assessment with a characteristic diurnal shape of irradiance and some patterns of noise. Misalignment leads to a distinct rippled shape in the diurnal curve of DNI and DHI irradiance. All days in the MFR-7 data sets have been checked for misalignment manually since the rippled shape does not get detected with the automatic quality assessment scripts. Additionally to the semi-automatic quality control mentioned below, manual inspection of the all data set collected with MFR-7s are performed to remove periods where either misalignment or soiling compromised the data quality.

Eppley Setup Likewise to the alignment issues that apply to the MFR-7, the most frequent source of error for the DNI measurements with a pyrheliometer relates to the precise tracking of the Sun. To automatically identify days with tracker malfunction, measured DNI (DNI_m) is compared to the calculated DNI (DNI_c) according to equation 2.1 solved for DNI for SZA $< 85°$ based on the measurements from the two PSPs. Days get flagged for misalignment when the difference between measured and calculated values exceeded 10%. This procedure is only applied to identify days with tracker misalignment. The procedure to identify ground truth data is still based on the quality assessment from 3.2.3. The meteorological conditions in Merced cause occasional formation of ground fog during the night and in the early morning hours. Occasionally, these conditions lead to condensed moisture on the glass of the pyrheliometer, especially because the

observatory in Merced is surrounded by farmland. If that occurs, a characteristic dent is visible in the DNI graph in the morning hours. Days that showed this characteristic have been removed completely from the analysis.

3.2.6 Estimation of accuracy for other locations

To estimate the capabilities of the semi-automatic data quality control, the Merced data set from the MFR-7 and the Eppley setup have both been cleaned with the semi-automatic quality control described above. This procedure includes addressing the problems described above including removing data with obvious and suspected misalignment and shading problems, data where soiling issues are known as well as data with the two described issues of misalignment and moisture mentioned above. The statistics of the semi-automatic data quality controlled data sets are compared to the statistics of the ground truth data set to verify the semi-automatic data quality control (see Table 3.1). Especially the high cross correlation ($\rho = 0.9888$) and the low MBE and MAE indicate that the semi-automatic quality control is able to identify high quality data, however the error is slightly higher than with the automated quality control. Hence, all our data sets are of high quality and suitable for the verification of the SUNY DNI model.

Table 3.1: Statistics for automated quality control based on redundant measurements and the semi-automatic quality control algorithm. As expected, the automated quality control generates a higher quality data set. However the semi-automatic quality control still derives good results.

	Size of data set	Mean MFR-7 (W/m^2)	Mean Eppley (W/m^2)	MBE (W/m^2)	MBE (%)	MAE (W/m^2)	MAE (%)	RMSE (W/m^2)	RMSE (%)	ρ (-)	σ (W/m^2)	σ_p (%)
Redundant QC	4111	636.5	553.7	7.4	1.1	14.3	2.2	18.5	2.9	0.998	16.9	2.7
Semi-automatic QC	6863	490.5	449.4	13.9	2.8	28.8	5.7	50.2	10.0	0.9888	48.3	9.8

3.3 Error metrics & indices

3.3.1 Statistical tools

Well established statistical measures are used to evaluate the accuracy of models and forecasts. These error metrics will be used in this chapter to evaluate the SUNY satellite-to-irradiance model and in the following chapters to evaluate the performance of forecasts. The statistical metrics used throughout this work are Mean Bias Error (MBE), Mean Absolute Error (MAE), Root Mean Square Error (RMSE), Standard Deviation (σ) and Correlation Coefficient (ρ) calculated as in Equations (3.2),(3.3),(3.4) and (3.7). For a more compact notation we first define ΔI as:

$$\Delta I = I_{GT} - I_M \tag{3.1}$$

where I_{Gt} represents irradiance considered as ground truth, either DNI or GHI. If available, ground measurements are used. Where stated, satellite derived data is considered to represent ground truth when forecasts are validated in remote locations (e.g. in Chapter 5). I_{Mo} is irradiance obtained with a model or forecast, depending on the context. I can be both, DNI or GHI. It then follows:

$$MBE = \frac{1}{N}\sum_{n=1}^{N}\Delta I_n, \tag{3.2}$$

$$MAE = \frac{1}{N}\sum_{n=1}^{N}|\Delta I_n|, \tag{3.3}$$

$$RMSE = \sqrt{\frac{1}{N}\sum_{n=1}^{N}\Delta I_n^2}, \tag{3.4}$$

variables with an over-bar indicate the mean value of that variable. These metrics are commonly applied to evaluate solar energy models and forecasts (e.g. [21],[121], [72]). In many instances it is advantageous to calculate relative values. Unless specifically noted, all relative and percentage error values are calculated

with respect to the mean value of the variable and indicated with a prescript r. E.g. the relative RMSE is calculated as

$$rRMSE = \frac{RMSE}{\overline{I}}, \tag{3.5}$$

Additionally, the cross correlation ($xcorr$ or ρ) and standard deviation (σ), are used, defined as:

$$xcorr = \rho = \frac{\sum_{n=1}^{N}(I_{Gt,n} - \overline{I_{Gt}})(I_{Mo,n} - \overline{I_{Mo}})}{\sqrt{\sum_{n=1}^{N}(I_{Gt,n} - \overline{I_{Gt}})^2 \sum_{n=1}^{N}(I_{Mo,n} - \overline{I_{Mo}})^2}}, \tag{3.6}$$

$$\sigma = \sqrt{\frac{1}{N}\sum_{n=1}^{N}(\Delta I_n - \overline{\Delta I})^2}. \tag{3.7}$$

3.3.2 Forecasting skill (s)

To provide an important evaluation criteria to measure the forecast quality and to make results comparable to other forecast approaches (e.g. [75, 15, 106]), the forecasting skill is calculated as:

$$s = 1 - \frac{RMSE_{\widehat{I}}}{RMSE_{persistence}}, \tag{3.8}$$

where $\widehat{I}$ represents the irradiance forecast and *persistence* the reference forecast model as defined in 4.3.5 and 5.3.1, depending on the forecast horizon. For a perfect forecast $s = 1$ would be obtained, while a negative forecasting skill occurs as soon as $RMSE_{\widehat{GHI}} > RMSE_{k_t-pers.}$. A negative forecasting skill indicates that the assumptions of the upcoming sky conditions are strongly erroneous.

3.3.3 Cloud index (k_t)

It is frequently useful to directly draw conclusions about the sky conditions form the irradiance time series. For GHI time series, the cloud index k_t is defined

as:

$$k_t = \frac{GHI_{Gt}}{GHI_{clear}}, \tag{3.9}$$

as mentioned above, GHI_{Gt} represents GHI measured with the MFR-7s or pyrheliometers (as described in section 3.2) and GHI_{clear} refers to the GHI under clear sky conditions for the same time period.

3.3.4 Clearness index (k_b)

Similar to the cloud index for GHI, the clearness index k_b is defined for DNI time series as:

$$Clearness = Ci = k_b = \frac{DNI_{Gt}}{DNI_{clear}}, \tag{3.10}$$

where DNI_{Gt} are the values considered as ground truth and DNI_{clear} is derived from a clear sky model. In general, kt and Ci values range between 0 and 1, where 0 indicates complete overcast conditions while 1 indicates clear skies. However, due to cloud edge effects and inaccuracies in the clear sky model, values higher than 1 occur. In those cases, the values are set to 1 (or 1.3 where noted). This does not interfere with the purpose of quantifying the error related to the transmissivity of the atmosphere. All clear sky values are calculated with the method proposed by Ineichen and Perez (models proposed and discussed in [47], [50], [32]).

3.3.5 Solar variability

Besides high yearly average irradiance values, variability is an important factor for determining the quality of the solar resource at a certain location. Detailed information about the expected variability at a given location is also necessary to size components of solar systems accurately. Below we discuss different metrics for the assessment of variability.

3.3.5.1 Variability events

To quantify the capabilities of a irradiance model or forecast in providing an accurate picture of solar variability and ramp events, we first can detrend the solar irradiance time series by removing the deterministic parts in the diurnal cycle of irradiance. Therefore, we subtract the expected clear sky irradiance values from the ground truth data and calculate the difference between two consecutive data points:

$$V_{I,n} = (I_{Gt} - I_{CS})_{n+1} - (I_{Gt} - I_{CS})_n, \tag{3.11}$$

where V_{Gt} stands for the ground truth variability. To take the inaccuracies for the clear sky model into account, variability values $|V| < 15W/m^2$ are removed from out variability analysis. This measure of variability is often normalized by the expected clear sky values where noted. However, if it is not normalized, it provides a more intuitive understanding of the magnitude of variability events.

To quantify solar variability in frequency and magnitude as in figure 3.6, we describe the variability $(V)Gt)$ with a probability density function (p) for variability events (v_i) and $i = 1...n$. Therefore, we can write:

$$p(a \leq v_i \leq b) = P(a \leq V \leq b), \tag{3.12}$$

where a and b represent the ramps between the limits where the number of bins has been set to 100 (N=100). This analysis is performed with a reduced but continuous data set.

3.3.5.2 Variability index

The Variability Index (VI) was proposed by [112], as a method to quantify the variability in the solar resource. Originally, the VI was introduced for GHI measurements but it works equally well for DNI. The VI can be calculated according to:

$$VI = \frac{\sum_{N=1}^{n} \sqrt{(I_{n+1} - I_n)^2 + \Delta t^2}}{\sum_{N=1}^{n} \sqrt{(I_{CS,n+1} - I_{CS,n})^2 + \Delta t^2}}. \tag{3.13}$$

The VI can be calculated for arbitrary time sample rates and different lengths of data sets. Based on these characteristics, the VI is examined for different time resolution and compared to V.

3.3.6 Ramp rates in power output

In addition to the analysis of variability, the solar variability of a location is related to ramp rates in the power output of solar farms in section 3.4.5. In particular, the spatial averaging between the irradiance measurements and the size of a PV farm is of interest. The PV array deployed in Merced covers an area of approximately $34,000\ m^2$. In contrast, the ground measurements are point measurements (area $\sim 1cm^2$) while satellite data represents a vast area of approximately 1 km by 1 km or $1,000,000\ m^2$. A ramp event in both power output or ground irradiance can be defined as the difference between two consecutive values (see Eq. 3.14). The deployment of a single axis tracking system makes the relation to DNI important since variability and ramp rates in DNI are inherently larger than in GHI. However, the expected correlation between the ramp events from the DNI data to ramp events in power output is limited since the deployed tracking system is only single axis. This means that the PV array utilizes a varying relation of GHI and DNI depending on the mode of operation of the power output optimized tracking controls. Ramp rates in power output and irradiance are characterized as follows:

$$Rr_{PO} = PO_{n+1} - PO_n, \tag{3.14}$$

$$Rr_I = I_{n+1} - I_n, \tag{3.15}$$

where Rr represent ramps in power output and irradiance. This is also be referred to as the step changes in a time series. The correlation of two time series of ramp rates can be calculated as by using this definition of Rr instead of I in equation 3.6.

3.4 Satellite model verification results

3.4.1 Statistical results

The statistical results for the whole SUNY data evaluation are summarized in Table 3.2. An MBE between −6.39% and 14.21% indicates a good estimation of the average irradiance by the SUNY model with a small location-dependent bias. For 3 of the 4 locations (Berkeley, Davis and Merced), the SUNY model tends to underestimate the DNI. Overestimation of DNI occurs in San Diego. Previously, [35] reported results for sites of different characteristics than ours. Since none of the sites under study had long overcast periods or extended snow cover during winter, our results are consistent with the conclusions reached by [35] that greater difficulties for the SUNY model are only likely to occur at locations with long periods of continuous cloud and snow cover.

The MAE ranging from 15.34% to 24.12% represents the magnitude of the error for each location. Modeling DNI is more complex than modeling GHI due to the larger parameter space and the strong dependence of DNI on atmospheric turbidity. However, the MAEs are comparable to MAEs for the GHI model found by [93]. The RMSE for the different locations range from 21.67% to 42.24%. Previous validations found a RMSE of GHI between 20% and 35% ([93]) and a RMSE for DNI between 34% and 41% DNI ([121]). [21] found a daily average RMSE of 52% and and RMSE of 67% for hourly DNI averages derived from remote sensing. The range of cross correlation values between 0.9063 and 0.9557 shows good agreement between ground measurements and the SUNY data sets. A high cross correlation is especially important because of the representation of solar variability in both data sets. The error in solar variability is discussed further in Section 3.4.3.

Results for the error distribution with different parameters are summarized in Figure 3.2 as an example for Davis. The scatter plot in Figure 3.2 (left) shows the modeled DNI versus the measured DNI. The accumulation of values on the right side of the diagonal in the scatter plot suggests that the SUNY model tends to underestimate the DNI at this location. Furthermore, it is obvious that there is a wide spread of data in the scatter plot which indicates frequent random errors of

different magnitude. This result is consistent with the results from the statistics in Table 3.2, especially the RMSE.

Table 3.2: Results of the applied error metrics (Equations: 3.2, 3.3, 3.4, 3.6, 3.7) to compare DNI data measured on the ground with data from the satellite-to-irradiance model SUNY. The errors for all stations are within the same order of magnitude, however there are different characteristics for each location. All percentage values have been calculated with regards to the mean MFR-7 values. Note that the mean values of the data set are not yearly averages as the data sets for each location cover different time periods.

Location	Size of data set	Mean measured (W/m^2)	Mean SUNY (W/m^2)	MBE (W/m^2)	MBE (%)	MAE (W/m^2)	MAE (%)	RMSE (W/m^2)	RMSE (%)	ρ (-)	σ (W/m^2)	σ_p (%)
Merced	4164	636.5	569.7	66.8	10.50	97.7	15.34	137.9	21.67	0.9241	120.7	19.0
Davis	9089	499.3	428.3	71.0	14.21	108.3	21.69	151.2	30.29	0.9278	133.6	26.8
Berkeley	8861	402.5	367.2	35.2	8.75	75.1	18.67	119.9	29.79	0.9557	114.6	28.5
San Diego	3187	383.3	407.8	−24.5	−6.39	92.4	24.12	161.9	42.24	0.9063	160.0	41.7

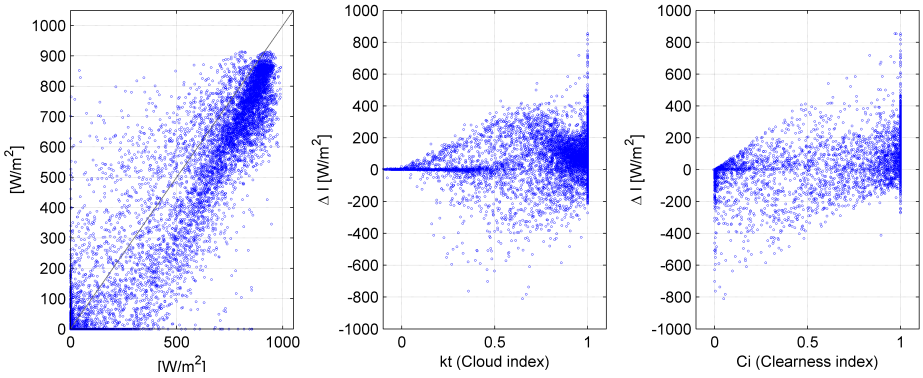

Figure 3.2: The scatter plot (left) shows ground measurements versus the satellite data for the whole data set in Davis. The MBE of 14.62% leads to an accumulation of points on the right side of the diagonal. The error versus kt plot (middle) shows that the magnitude of error increases from high cloud cover to clear conditions. The error versus Ci plot (right) leads to a rhombus shaped distribution of values. The plots are comparable to the results obtained for all the other locations.

3.4.2 Error versus cloud and clearness index

The plot relating the error to cloud index in Figure 3.2 (middle) shows an increasing error with decreasing cloud cover (increasing k_t). For low cloud cover, irradiance values are higher and therefore, the possibility of errors of higher magnitude increases. The clustering of values for high cloud index values ($k_t > 0.7$) on the positive side is caused by the underestimation of DNI by the SUNY model at this location.

The right plot of Figure 3.2 shows the magnitude of the error in Wm^{-2} related to Ci. Ci can be seen as a measure representing the clearness of the atmosphere. The maximum error for $Ci = 0$ is -800 Wm^{-2} which occurs when the satellite model wrongly detects clear conditions when it is in fact an overcast day. However, this does not occur very often. The maximum error for $Ci = 1$ is 800 Wm^{-2} when the satellite model senses overcast sky when it is in fact clear. This extreme case is not observed frequently. More clear days in the data set cause the clustering at high Ci values. For Merced and Berkeley the plots show similar characteristics for the error. Taken into account that the SUNY model

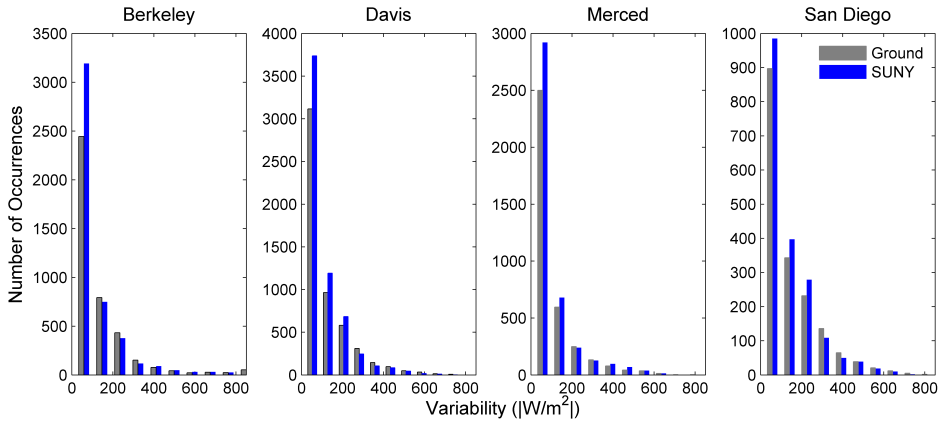

Figure 3.3: Comparison between variability in ground DNI data and DNI data derived with the SUNY model for all studied locations. Both data sets follow the same trend but variability events of small magnitudes are consistently overestimated in the SUNY model. For higher ramp rates the general performance is location dependent.

underestimates irradiance in San Diego the error plots are also consistent with the results shown in Figure 3.2.

3.4.3 Error in variability

Figure 3.3 shows the occurrence of variability events (V) in consecutive clusters of 80 Wm^{-2} for all four locations, derived from the satellite-to-irradiance model and ground measurements. Small variability events are more likely to occur and decrease with the magnitude of the variability event. In general, the trends of the ground measurements are well reflected in the SUNY model. However, the SUNY model tends to overestimate the occurrence of low magnitude variability at all four locations. The extend of overestimation varies for each location (e.g the occurrence of the lowest variability event for $15 - 80$ Wm^{-2} is overestimated in Berkeley by 30% whereas in San Diego only by 7%). The performance of the SUNY model in detecting higher ramp rates is location dependent with no obvious trend. The overestimation of variability with low magnitude can be explained with the observed error patterns, subject to discussion in 3.4.6.2. Two different measures of variability are used. The results are shown in figure 3.3 and 3.4. The attributes of figure 3.4 are obviously different from figure 3.3. The method of variability events

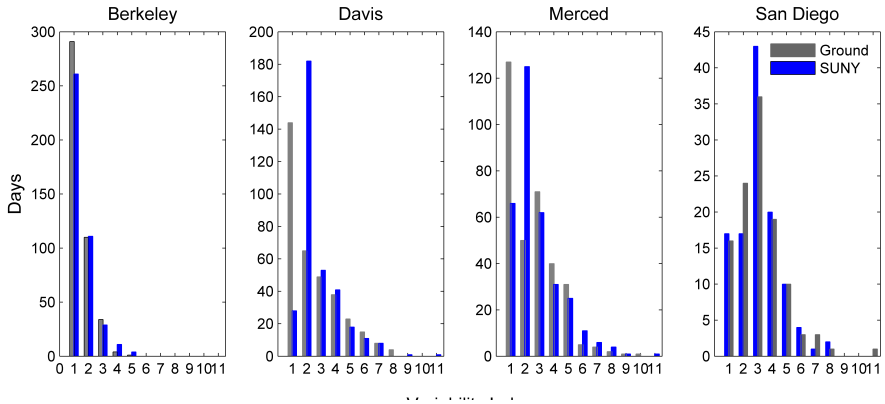

Figure 3.4: Histogram of magnitude and occurrence of VI for four locations. The variability in Berkeley is significantly lower than for the other locations. The SUNY model underestimates the occurrences of days with no or very low solar variability ($VI = 1$). The performance on capturing the occurrence of certain VI is location dependent. The error patterns described in 3.4.6.2 can explain the noticeable bias in Merced and Davis between $VI = 1$ and $VI = 2$.

shows the occurrence of ramps in Wm^{-2}. In contrast, the VI is more capable of showing the variance in solar variability time series. Since the VI is just a number without a perceivable physical representation, this index is less intuitive but still a good method to describe and compare the variability for different locations.

Figure 3.4 plots the occurrence of VI values of certain magnitude as daily values for all four locations. The values achieved for VI in Berkeley are of significantly lower range than for the other locations. In Berkeley the sky conditions are often either clear or entirely overcast. Therefore, there is a lack of variability in irradiance as compared to the other locations. Based on the figure, this behavior is represented well in the SUNY data with a slight underestimation of $VI = 1$ and $VI = 3$ and overestimation of $VI = 2$ and $VI > 4$. A VI of 1 indicates no solar variability, and thus a day that is either completely overcast or continuously clear. The identification of days with no variability by SUNY data worked especially well in San Diego and Berkeley. However, in Davis and Merced a $VI = 1$ is significantly more likely to occur than modeled by SUNY. Instead, a $VI = 2$ appears considerably more often at these locations. This bias can be explained by the error patterns described in 3.4.6.2, which are especially pronounced in arid areas. In general, the occurrence of VI values derived by ground data is estimated

well by the SUNY model. This is also due to the fact that small modeling errors of VI average out in long time series if there is no systematic bias. The statistical results from the VI analysis and the error between both data sets are summarized in Table 3.3.

Table 3.3: Comparison of time series of daily variability indices (VI) calculated by MFR-7 and SUNY DNI with 30 minute temporal resolution. In general, the SUNY models the average half-hourly DNI variability well. The RMSE is in the order of $\sim 30\%$ for all studied locations. To give an idea about the difference between ground variability derived from 1 minute MFR-7 DNI measurements to the VI of 30 minute averages, the mean and maximum of daily VI time series calculated with 1 minute temporal resolution ground data has been added to the table. It can be seen that the VI varies strongly on the different temporal resolutions.

Location	Days in data set	$Mean$ MFR-7	$Mean$ SUNY	max MFR-7	max SUNY	MBE	MBE_p (%)	MAE_p (%)	$RMSE_p$	ρ	σ	1 minute $Mean$	1 minute max
Berkeley	440	1.82	1.92	5.88	5.53	-0.10	-5.46	19.18	30.04	0.77	0.54	6.17	29.06
Davis	346	3.03	3.18	8.57	11.22	-0.14	-4.78	22.99	30.91	0.84	0.93	18.47	104.00
Merced	333	3.07	3.21	13.47	11.57	-0.14	-4.71	27.37	36.52	0.78	1.11	8.55	64.65
San Diego	114	3.65	3.57	8.80	11.83	0.08	2.19	20.70	30.01	0.76	1.10	14.78	67.30

3.4.4 Variability smoothing

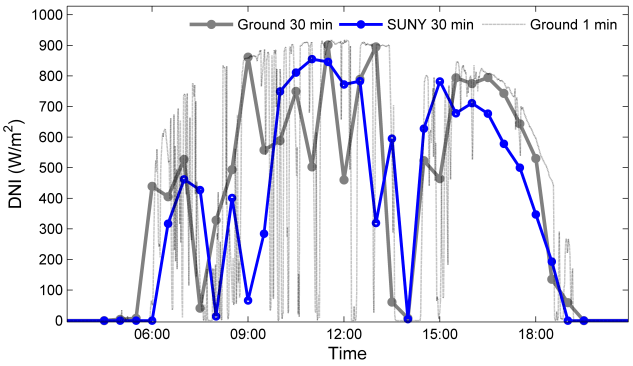

Figure 3.5: Example of the diurnal irradiance of a highly variable day in Berkeley for 25 May 2012. The variability on a 1 minute resolution is significantly higher in change of frequency and amplitude than represented by the 30 minute values. This also becomes clear by looking at VI for the different data sets: ground data with 30 minute resolution: $VI = 7.6$, SUNY data with 30 minute resolution: $VI = 6.6$ and ground data with 1 minute resolution: $VI = 57.2$.

The calculation of temporal averages disregards large portions of fine grain temporal variability. Figure 3.5 shows the diurnal cycle of DNI on a day with high solar variability with a 1 minute resolution, with 30 minute ground measured averages and with 30 minute SUNY data. The 1 minute DNI variability shows, as expected, much higher frequency and amplitudes than the 30 minute average data. The SUNY data has similar characteristics concerning the occurrence of ramps. However, there are inconsistencies and a time shift when compared to ground 30 minute values. The close match of VI for longer time series can be explained by the fact that small, unbiased deviations are averaged out over longer periods of time. Figure 3.6 shows the probability density distribution of variability for the SUNY data set, the 30 minute ground measured data sets and the 1 minute ground variability for all four locations. The 30-minute averages of the 1 minute ground DNI data smoothes out the frequent occurrence of large variability events. Furthermore, the maximum magnitude for variability occasionally reaches 900 Wm^{-2} on 1-minute resolution, whereas the maximum magnitude of the 30-minute averages only reaches 600 Wm^{-2}. A comparison of the 30-minute data sets shows that

the variability based on the SUNY model has the same features as the ground measured variability, however noticeable differences on a smaller scale occur. This is consistent with the behavior shown in Figure 3.4.

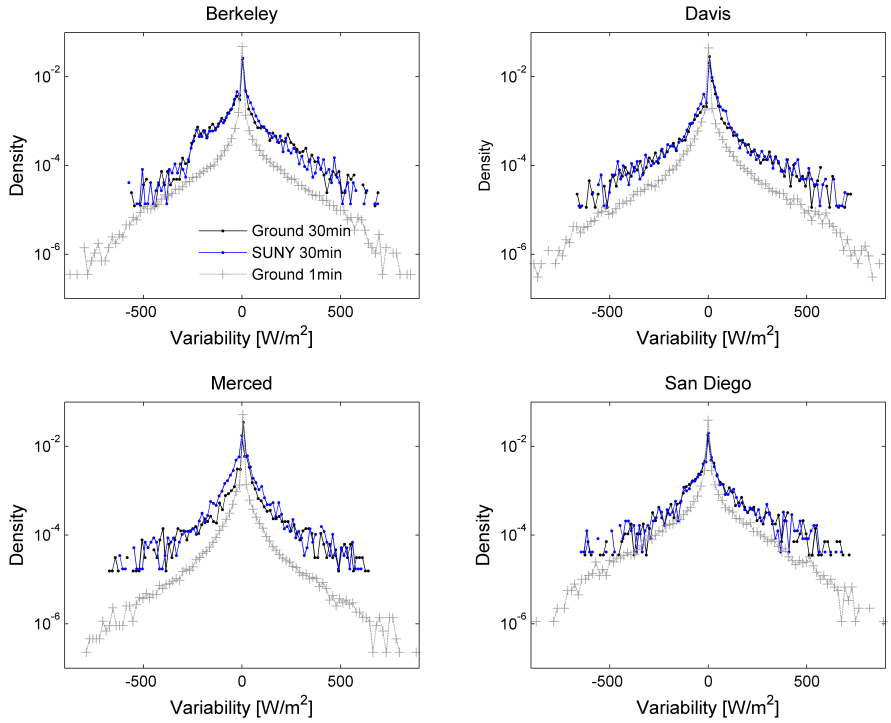

Figure 3.6: Probability density function of variability for four studied locations. The 30 minute solar variability is shown for ground and SUNY data sets in comparison to the ground measured variability with 1 minute temporal resolution. It can be seen that the 30 minute variability averages smooth out frequently occurring high solar variability events. Therefore, frequently occurring high solar variability events on the 1 minute timescale are 'summarized' into more frequently occurring lower variability events as 30 minute averages.

3.4.5 Correlation of ramp rates

The power output of a single-axis tracking PV array relates to both DNI and GHI. Therefore, the correlation coefficient between ramps in PV power output data and ramps in DNI (Rr_I) is limited, and fluctuations in DNI do not necessarily cause ramps in power output (Rr_{PO}). However, large Rr_I imply strong ramps in

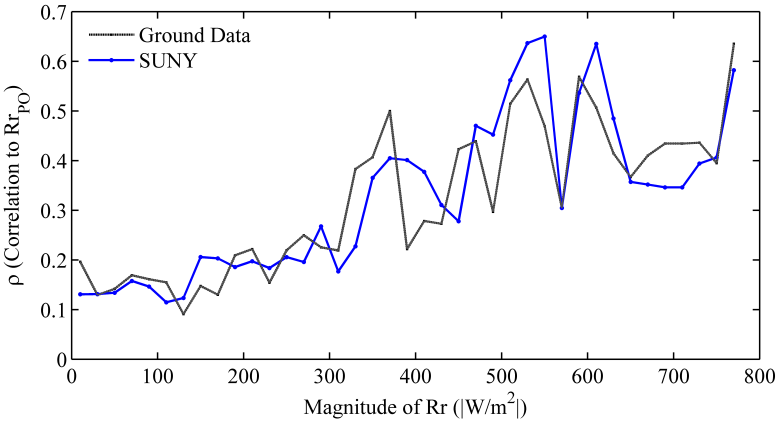

Figure 3.7: Correlation coefficient (ρ_{PO}) of power output data and the two irradiance data sets versus the magnitude of ramp rates derived for ground measurements and satellite data. For small ramps ρ is very low. The correlation is generally better for higher ramps.

power output from the PV array and therefore cause higher values of Rr_{PO}. This is illustrated in Fig. 3.7, where the correlation coefficient, calculated according to equation 3.6, between (Rr_{PO}) and Rr_I, is shown in clusters of Rr_I of 20 Wm^{-2}. The correlation for small and medium ramp rates ($Rr_I < 400\ Wm^{-2}$) does not exceed 0.3 which indicates a weak linear relation. This can be explained by the fact that small Rr_I are often caused by advection of clouds with a low optical thickness (e.g dispersing contrails). Under these conditions, GHI ramp events are small. However, for higher ramp rates ρ_{PO} is higher, hence a stronger linear relation between Rr_{PO} and Rr_I exists. Both models follow the same trend while it is not clear which DNI data set generally performs better. We can assume that both data sets would agree in terms of resourcing for sizing the solar array in Merced.

3.4.6 Sources of errors and possible corrections

3.4.6.1 Clear sky model

A common source of error of the SUNY model is the underlying clear sky model. Figure 3.8 shows samples for some selected clear sky days for all four locations over time normalized to the length of the days (Sunrise= -1, Sunset= 1). For

Berkeley, Davis and Merced, the clear sky model used in the SUNY model, tends to underestimates clear sky DNI. This might be the explanation for the general trend that the SUNY model underestimates the long term average DNI at these sites. Correcting for this, by implementing more accurate clear sky models, could significantly improve the performance of the SUNY model. For San Diego, the underlying clear sky model seems to perform better than for the other locations. However, correct modeling of clear sky DNI is a rather complex task with inherent difficulties due to the large number of variables determining clear sky DNI magnitude [70] [47]. It is not possible to determine the AOD with satellite imagery with the required accuracy. DNI clear sky models with accuracy comparable to high quality irradiance measurements can be achieved. These high performance clear sky DNI models are heavily dependent on ground based measurements, especially AOD (e.g REST2 model by [31]).

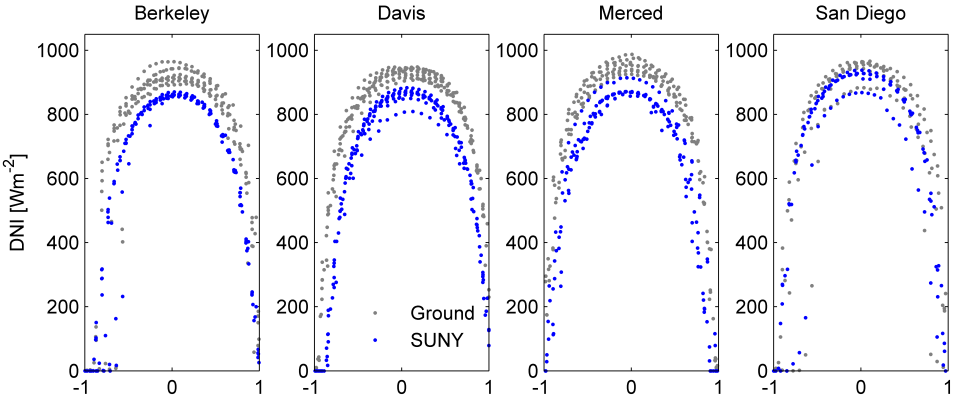

Figure 3.8: Days with very clear atmospheric conditions for Berkeley, Davis, Merced and San Diego (from left to right) versus normalized time. -1 indicates sunrise and 1 sunset. It becomes clear that local corrections for the clear sky model could reduce the error significantly. Note that the plots were produced with different numbers of clear days due to availability (Berkeley: 9 days, Davis: 10 days, Merced: 8 days, San Diego: 6 days).

3.4.6.2 Observed error patterns

Besides the described errors due to the inaccuracies in the clear sky model, another frequent source of error appears to be the assessment of the ground albedo.

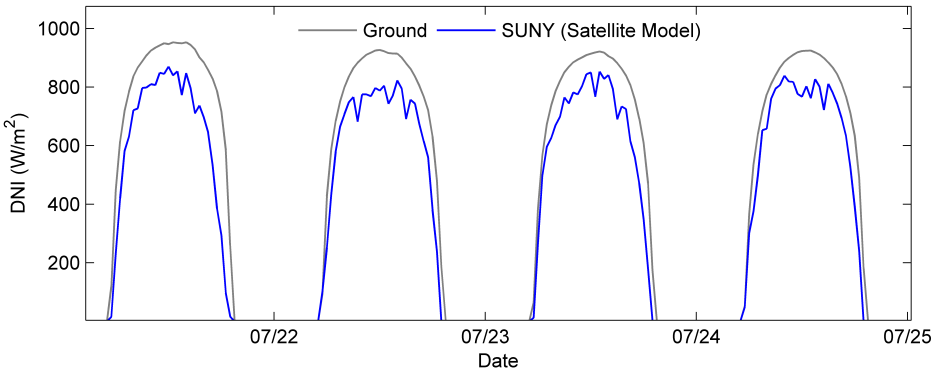

Figure 3.9: The diurnal cycle of DNI on four consecutive days are shown for Merced. While the ground measurements show a clear day, the SUNY model shows variability during midday in the DNI data. This is most likely caused by an incorrect correction for changing ground albedo. Similar error patterns were found in the data sets of all other locations.

Figure 3.4.6.2 shows four consecutive days of ground and SUNy data from Merced. There is a discrepancy between both data sets during midday. While the ground measurements show a clear day, the SUNY model assumes a certain amount of variable cloud cover or higher AOD. These patterns were found in 59 out of 339 days in Merced with a distinct accumulation between July and October. Data from the other locations show comparable characteristics, whereas the magnitude is about the same in Davis and moderately weaker in Berkeley. This effect also occurs in San Diego but is less pronounced. Issues caused by certain ground albedo effects are known (e.g [98]) and can be corrected for if their properties are well defined. However, part of the albedo characteristics are caused by vegetation with a seasonal cycle with strong yearly variations and are therefore hard to address.

3.5 Summary

In this chapter, we described the post measurement data quality control tools, applied to our solar irradiance measurements (described in chapter 2). The Merced observatory was used as a control and calibration site, since measurements

from two redundant setups are available at this location. An automatic scheme for data quality control was compared to a supervised (semi-automatic) data quality control approach for the same location in order to test the quality control methodology (Table 3.1). It was shown that it is possible to identify high quality DNI data without redundant measurements, but the data inspection process is labor intensive and needs a good understanding of the measurement process and the instrument characteristics. Based on the high quality ground data, we validated the accuracy of satellite based DNI models (the SUNY v2.0 model, in particular), at four locations in California (Merced, David, Berkeley and San Diego). This validation includes statistical measures as well as an investigation of solar energy variability in both data sets. Additionally, the correlation between ramps in both irradiance data sets to the ramp rates of a single axis, 1 MW PV array was carried out.

The main conclusions of this chapter are: (1) Data obtained with the SUNY model represents well the ground truth concerning DNI variability and magnitude with the statistical characteristics shown in Table 3.2 for these regions where cloud cover and snow do not persist over long periods (weeks). Long periods of cloud or snow cover introduce systematic errors. The inter-annual DNI variability was not studied here (this is discussed in [66] and [33]). (2) More accurate clear sky models improve substantially the performance of satellite-to-irradiance models. However, the errors caused by the ground albedo effects are difficult to address. (3) Whereas the occurrence of small magnitude variability events is overestimated by the satellite derived data, the frequency and amplitude of variability events are represented well by the SUNY model. Because most satellite-to-irradiance models are cognate, we can assume that they show similar characteristics in providing DNI variability data as shown in this study. (4) The utilization of SUNY data for sizing single axis tracking solar energy systems would result in a over- or underestimation of yearly yields depending on the location and time specific bias. However, based on the presented results concerning ramp rates in the output of a single axis tracking PV array, we conclude that the SUNY data performs well for sizing tracking solar energy systems on a 30-minute resolution. (5) Considering the associated cost of

maintaining DNI ground measurements, the SUNY modeled data is a valuable resource to assess the DNI at half-hourly rates. Accurate high quality ground data collection at high temporal resolution is still needed to assess and quantify the variability on shorter timescales, to calibrate clear sky models and to calibrate short-term solar forecasting methods.

Note: This chapter contains work, previously published in:

- L. Nonnenmacher, A. Kaur and C.F.M. Coimbra "Verification of the SUNY direct normal irradiance model with ground measurements,", *Solar Energy*, pp. 246-258, 2014.

Chapter 4

Intra-day solar irradiance forecasting

In chapter 3, we validated the satellite-to-irradiance model for DNI and found it to be in good agreement with ground data. In this chapter, we shows how to implement a GHI forecast for $1h-$, $2h-$ and $3h-$ahead, utilizing online, near real-time, processed satellite images derived from the visible channel ($0.55 - 0.75\mu m$) of the Geostationary Operational Environmental Satellites West and East ($GOES - W$ and $GOES - E$). Currently, the direct use of satellite images is not very common due to difficulties concerning image availability, albedo correction, resolution, cloud segmentation and tracking and real time processing of images. Three methodologies utilizing satellite images for solar forecasting have been proposed by [38, 37] and [76]. Our approach builts up on these previous findings, summarized in section 4.1. The surface resolution of our input images is approximately $1km\ x\ 1km$. Images are combined with a fast cloud segmentation algorithm. Two consecutive frames of cloud index images (ηs) are the foundation for the application of an advanced optical flow algorithm proposed by [115], applied to derive cloud motion vectors (CMV). This approach also enables the derivation of cloud velocity. Optical flow was found the most suitable approach for cloud tracking for the used images, while other cloud tracking methods were the topic of several previous publications ([23, 36, 24]). The CMV field and velocities are utilized to calculate the streamline of the flow field reaching the location of inter-

est. This streamline enables the identification of an area of pixels most likely to propel to the location of interest. All of these inputs are deterministic and therefore provide a method that can be applied without any training for every location covered by satellite images. This method is heavily based on the performance of a satellite-to-irradiance model that translates the identified region of cloud intensity values into forecast values of GHI at the region of interest. In this context, a ground measurement enhanced semi-empirical satellite-to-irradiance model has been developed.

This chapter is divided into two main parts, the implementation of a improved satellite-to-irradiance model and the introduction of a forecasting model. Section 4.1 gives an overview of previously proposed methods covering the same forecast horizons for GHI and highlights the purpose for this study. Section 4.2 focuses on the processing of the satellite images provided by National Oceanic and Atmospheric Administration ($NOAA$), the applied cloud segmentation and the satellite-to-irradiance model. Section 4.3 includes the selection of a cloud tracking method, cloud tracking with optical flow and the deterministic solar irradiance forecasting approach. Section 4.4 contains the evaluation metrics for the satellite-to-irradiance model and for the forecasts. Results of the overall methodology for the location of San Diego, California are discussed. Section 4.5 includes conclusions, prospective applications and open research questions based on the results.

4.1 Previous work

The field of solar irradiance and photovoltaic power output prediction increased rapidly within the last decade. Various previous studies covered (multiple) hour ahead GHI forecasts, based on several different methods. In general it can be distinguished between statistical, machine learning, image based and numerical weather prediction (NWP) based methods. Satellite image based forecasts are among the most promising approaches for $1h - 3h$ ahead forecasts. An early approach in satellite based solar irradiance forecasting was proposed by [38] where clouds are segmented from images captured by the Meteosat satellite and

tracked based on a statistical algorithm. The cloud motion is then extrapolated and prospectively advected cloud regions are translated into the forecast by the satellite-to-irradiance model. [67] showed that the forecasting accuracy based on satellite images outperforms NWP based predictions for forecast horizons up to $4h$ ahead. [101] followed this general approach and applied it for images form the GOES satellites. Based on a evaluation covering seven locations, [101] found that the satellite based model outperforms NWP derived forecasts for up to 5 hours ahead. [76] combined the CMV based approach with artificial neural networks (ANNs) to create a hybridized forecast. The performance of the hybrid approach is at par or improves previously obtained results.

Motivated by the results presented in [38, 67] and [101], an advanced implementation of previously proposed deterministic satellite-based forecasting techniques with various crucial refinements, necessary to achieve good forecast performance in a highly variable solar micro-climate are proposed in this chapter. An unrefined application of deterministic, linear cloud advection based on precise cloud tracking and without decision heuristics leads to a negative forecasting skill for the test location in San Diego. This is partially due to the impact of frequently forming inversion layers over the Pacific Ocean.

4.2 Data processing

Figure 4.1 summarizes the data flow through this chapter, including the derivation of cloud index images (η) from satellite images pre-processed by $NOAA$. The cloud index images are used for the satellite-to-irradiance model and the forecast model. The forecast model includes cloud tracking based on optical flow to derive the cloud motion vectors ($CMVs$). The $CMVs$ are used for streamline and velocity calculations. Both are utilized to identify advecting cloud regions. The last step consists of the validation of the methodology by means of ground telemetry.

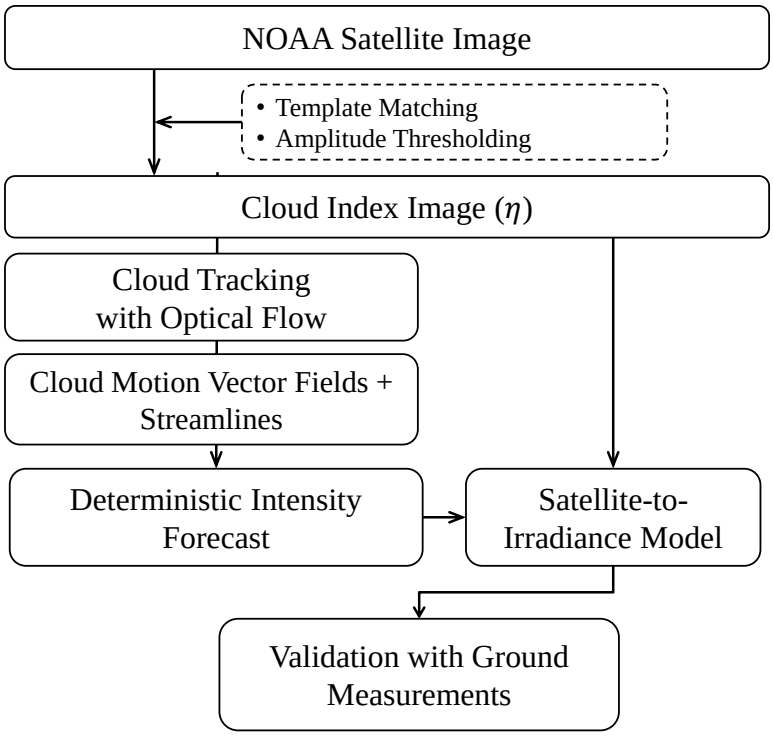

Figure 4.1: Schematic of data processing for the satellite-to-irradiance model based solar forecasting system.

4.2.1 Irradiance measurements

Ground measurements obtained at the San Diego solar observatory with a MFR-7 are used in this chapter (see section 2.3.2.2 for more details on data aquisition). This data is considered to represent the ground truth. Data sets were collected on a 1 minute sample rate and averaged to provide 15 minute values.

4.2.2 Satellite images

Relevant satellite images are accessed via $NOAA$ every 15 minutes during daylight times with an automated download script. The time interval of 15 minutes is chosen since the ground truth validation location (San Diego, California) lies in a narrow band where the recorded areas of the $GOES-West$ and $GOES-East$ satellites overlap. Images are available every 15 minutes. The most recent satellite image is accessible at http://sat.wrh.noaa.gov/satellite/1km/sandiego/vis1san.gif.

The period of study ranges from March 2013 to March 2014. The images are pre-processed by *NOAA*. This enables a clear distinction between clouds and earth surface without additional correction for the changing sun elevation angle during the diurnal cycle. The images are downloaded as Portable Network Graphics including a superimposed land mask. The land mask lines are replaced by not-a-number values based on their color. These images are used to derive cloud segmented images, also called cloud indexed images (ηs). Cloud segmentation to derive ηs is important for two purposes: (1) irradiance modeling at the Earth surface, and (2) computationally optimized cloud motion detection and cloud speed calculations. This step is crucial for the application of a satellite-to-irradiance model and the difference centroid algorithm based cloud tracking. It additionally reduces computation costs for cloud tracking based on optical flow. The location of the ground based solar observatory in the satellite image has been identified with triangulation based on distinct geographical features. This estimation has been optimized and verified by applying the satellite-to-irradiance model described below for all pixels in a 30 by 30 pixel area by identifying the one with the best correlation to the ground data. The downloaded satellite image is cut to a domain size of 200 by 200 pixels with the location of interest in the center to reduce computation costs. This domain size was chosen empirically based on the observation that it is very unlikely that clouds from outside of this domain are propelled to the location of interest within the studied time horizons.

4.2.3 Cloud segmentation

While the general idea of cloud tracking goes back to the first imagery from satellites, cloud extraction by image segmentation as part of an automated weather forecasting system was introduced much later by [64]. To be able to translate a *NOAA* satellite images into η, only the following two steps out of the originally 6 steps mentioned by [64] are necessary:

(1) Template matching to identify pixels showing the ground with its region specific albedo. The template has been generated from about 150 manually selected images from clear days. The average albedo image can than be calculated

with the equation:

$$\overline{\alpha} = \frac{1}{N} \sum_{i=1}^{N} Im_{clear}, \tag{4.1}$$

where $\overline{\alpha}$ indicates the derived average ground albedo map and Im_{clear} stands for the manually selected satellite images with no clouds (clear images). If certain regions over the Pacific Ocean have never been free of clouds, the cloud covered areas are replaced with values of cloudless regions over the ocean. A well known problem in irradiance modeling based on satellite images is caused by areas with snow cover due to irradiance reflectivity similar to clouds as discussed in chapter 3. While this is a problem in certain areas and interferes with cloud detection, the error introduced by this effect is neglected since the areas of occurrence are not in proximity to our areas of interest.

(2) Amplitude thresholding to separate clouds from ground pixels. To filter the noise introduced by the mismatch of the average ground albedo template to the background, the threshold filter can be set empirically:

$$\eta_{x,y} = \begin{cases} \eta_{x,y} = 0 & if\ |(Im_{x,y} - \overline{\alpha}_{x,y})| \leq T, \\ \eta_{x,y} = Im_{x,y} & if\ |(Im_{x,y} - \overline{\alpha}_{x,y})| > T, \end{cases} \tag{4.2}$$

where η represents the derived cloud indexed image, Im stands for the latest available satellite image, pre-processed by $NOAA$ and T is the applied threshold filter. For this study, $T = 3$ has been chosen. As mentioned above, $\overline{\alpha}_{x,y}$ indicates pixel intensity values from the average albedo image at the $x-$ and $y-$location.

Figure 4.2 shows $\overline{\alpha}$, calculated according to equation 4.1, Im as downloaded form the $NOAA$ website and the derived η, calculated with equation 4.2 as an example for 13-June-2013 20:45 coordinated universal time (UTC). It can be seen that the cloud separation works well in most regions. However, difficulties exist due to the threshold filter in areas where thin clouds are present (e.g. in the north east area of the example shown in Figure 4.2). Since the threshold filter only affects very thin clouds and the GHI attenuation by thin clouds is limited, the error introduced by this procedure can be neglected. Additionally to the ηs, a binary cloud fraction image (β) is calculated as follows:

$$\beta_{x,y} = \begin{cases} \beta_{x,y} = 0 & if\ \eta_{x,y} = 0, \\ \beta_{x,y} = 1 & if\ \eta_{x,y} > 0, \end{cases} \tag{4.3}$$

this β is important for the decision heuristics listed under section 4.3.6.

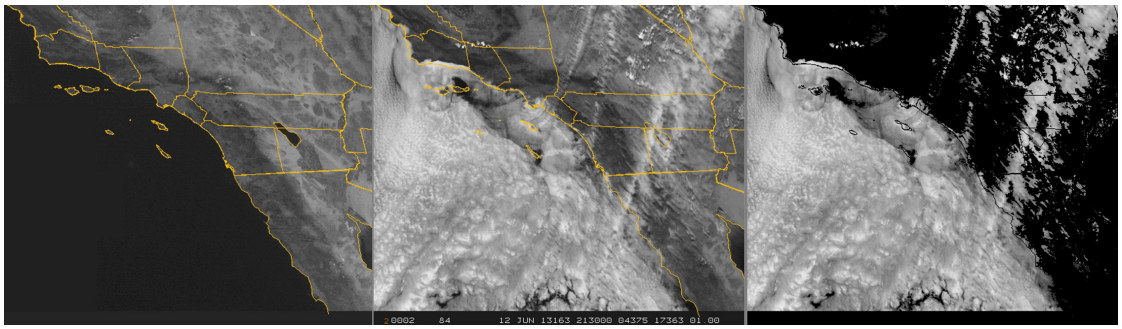

Figure 4.2: Example of the applied image processing steps to derive the cloud index image (η). The left image shows the average ground albedo image ($\overline{\alpha}$). The middle image shows the used $NOAA$ satellite image (Im). The right image shows the η derived by removing areas that match the albedo template. In general, this approach works well but thin clouds are challenging to detect. This effect can be seen by comparing the middle and the right image especially in the north east area. In these areas there are also difficulties in distinguishing between ground and clouds with the unaided eye.

A common approach for a satellite-to-irradiance model is to relate the pixel intensity values to irradiance conditions (e.g. [10], [97], [110] and [100]). This is also utilized in previous studies covering satellite based solar irradiance forecasting models (e.g. [38, 76]). While most of the satellite-to-irradiance models are based on unprocessed satellite images, a big part of the image processing to derive η in those cases is dedicated to correct for the changing albedo with varying sun elevation angle. Since the images used in this study already appear to be corrected for changing albedo, this traditional approach can be easily applied to the ηs here. The traditional approach, as proposed by [10], models the irradiance based on the η by utilizing the concept of the linear cloud index as follows:

$$n = \frac{\rho - \rho_{min}}{\rho_{max} - \rho_{min}}, \tag{4.4}$$

where n presents the linear cloud index, ρ refers to the reflectance scanned by the satellite at an instant (also called instantaneous planetary albedo or intensity)

while ρ_{max} and ρ_{min} refer to the maximum and minimum occurring intensity value in a large image data base. The GHI can than be modeled by applying the following equation:

$$GHI_{M1} = GHI_{CS} \cdot (1 - n), \tag{4.5}$$

where GHI_{CS} represents the expected GHI values under clear sky conditions as calculated with the model developed by [47, 50], and [32]. This approach relies on a linear relationship and is frequently used e.g. for the Heliosat method [4]). Multiple approaches have been taken to improve the linear model to achieve higher accuracy [27, 77, 85]. The statistical results of the validation of the linear model with ground measurements are discussed in 4.4.1. To enhance the accuracy for the utilized $NOAA$ satellite images, Model 2 was created.

4.2.3.1 Statistical model (Model 2)

The model described above is popular and commonly applied to model solar irradiance if only satellite images are available. Nevertheless, the performance of this approach can be enhanced significantly with ground measurements. A high performance of the satellite-to-irradiance model is required since the error in the satellite-to-irradiance model propagates into the error of the forecast. Ground measurements are available hence, statistical values over longer periods can be calculated. [86] proposed the usage of a lookup table for a satellite-to-irradiance model for optimized accuracy and calculation costs. We pick up this approach and relate an intensity value ρ to the statistical mean of k_t calculated by:

$$k_{t,M2}(\rho) = \frac{\overline{GHI}_{GT}(\rho)}{GHI_{CS}} = (1 - n_{M2}) = \overline{k}_{t,\rho}, \tag{4.6}$$

where ρ is the intensity value from η ranging between 24 and 44 but including 0 which indicates clear sky conditions. $\overline{GHI}_{GT}(\rho)$ is the average measured GHI value occurring for ρ and GHI_{CS} is the clear sky value calculated with a clear sky model mentioned above. Therefore, the lookup table contains 22 elements (see table 4.1). GHI is modeled by:

$$GHI_{M2} = GHI_{CS} \cdot k_{t,M2}(\rho), \tag{4.7}$$

where $k_{t,M2}$ is used as assigned by the created lookup table and GHI_{CS} is the clear sky value. The lookup table used for this study has been created with 4700 satellite image frames and corresponding ground measurements for the San Diego region. Results of the two satellite-to-irradiance models are discussed and compared in section 4.4.1.

SolarAnywhere® provides irradiance time series covering the continental US and Hawaii based on the SUNY model v2.0 [100], the model discussed in chapter 3. To compare the accuracy, the results from the above proposed model are compared to the SUNY model in 4.2. SUNY data was accessed via SolarAnywhere® with a temporal resolution of 30 minutes. Due to data availability, the look-up table based model with data from 2014 was compared to SUNY data from 2013. Since the inter-annual performance variability is low, this still gives us a good picture of the performance.

Table 4.1: Lookup table for the satellite-to-irradiance model, created from mean k_t values, based on ground measurements in San Diego. While these k_t values are optimized for San Diego, they presumably also provide an improvement over Model 1 for other locations (validated for Davis, California).

Intensity Value ρ	k_t	Intensity Value ρ	k_t
0	1.00000	34	0.36192
24	0.65228	35	0.33400
25	0.61249	36	0.28652
26	0.58331	37	0.25848
27	0.56444	38	0.27137
28	0.53644	39	0.23905
29	0.52786	40	0.22012
30	0.48311	41	0.20566
31	0.47338	42	0.16433
32	0.41145	43	0.16804
33	0.34690	44	0.17806

4.3 Cloud tracking and forecasting method

4.3.1 Cloud tracking testbed

Cloud tracking is needed for velocity field calculations in both, ground-based-sky and satellite images. The general approach for CMV field calculations is always based on the calculation of displacement of image features between two frames. However, the features that are tracked as well as the optimization approach to identify the same feature in two similar but not identical images can be quite different. While various feature tracking algorithms exist, three have been pre-selected for an initial feasibility test on an artificial cloud tracking test bed. For pre-selection, a detailed description about the implementation of the algorithm had to be available and the algorithms had to be suitable for a local computer. The three commonly applied methods are: (1) Difference Centroid Algorithm (DCA), (2) Particle Image Velocimetry (PIV), and (3) Optical Flow. For details about the implementation of these methods see [111, 76] and [115]. Previous satellite based solar irradiance prediction methods calculate CMV fields solely based on statistical approaches as in [38] or PIV as in [76]. The CMV fields are the foundation for the calculation of a streamline that is used for forecasting as described below in this section. The feasibility of these algorithms has been tested on a test bed, covering three artificially created cloud movement cases. Case 1 represents the linear movement of a cloud field through consecutive satellite images. Case 2 represents linear movement of two distinct cloud fields in opposite directions. Case 3 resembles linear cloud movement under highly variable conditions with forming and dissolving parts of the cloud field. Multiple artificial η have been created manually by moving and modifying cloud fields with known displacements between two frames. Based on this tracking test bed, the DCA does not identify cloud movement in complex conditions. While the DCA has an advantage due to its simplicity in implementation, it lacks robustness under broken sky conditions to unambiguously identify the right centroids if the number varies between two frames due to cloud evaporation, condensation, and precipitation (test bed case 3). Therefore, the DCA is not suitable for more complex tasks of cloud tracking

and is not considered further during this study. The PIV and the optical flow algorithms continuously identify the displacement correctly based on this test bed and therefore perform equally well. However, since the optical flow algorithm is an open source code in contrast to the commercial PIV software that was used, from here on, the optical flow algorithm is used exclusively.

4.3.2 Optical flow algorithm

Many variations of optical flow methods exist, each developed and optimized for different purposes. Their optimization are subject of current research for many computer vision applications. However, little effort has been made to apply these methods to track clouds segmented from satellite images. [16] and [125] are the only publication that apply optical flow algorithms for cloud motion tracking known to the authors. A summary of the utilized algorithm as presented in [115] and [116] is given here. More specific details are given in the references [46, 5, 115]. A well documented, free implementation of the optical flow algorithm is provided by [115] as Matlab functions. The method named $classic++$ described in [115] was identified as the most suitable approach for the purpose of cloud tracking, especially with regards to accuracy and processing times. The selection was based on a small test set (approximately 10 days worth of satellite images) by the achievement of the highest forecasting skill for those days with the developed method. The optical flow implementation provided by [115] is based on the global formulation originally introduced by [46]. The following is a summary of the studies and included for completeness. The optical flow algorithm works on the following basics: the first main assumption of brightness constancy is simply that the brightness of an image feature at location (x, y) remains constant while it is displaced between two frames to the position $(x+\Delta x, y+\Delta y)$ (initial implementation of optical flow). This holds true for most situations present in η. However, two simplifications about the cloud fields are implied in this assumption: (1) The cloud field formation, deformation and evaporation is negligible compared to the horizontal displacement, (2) the velocity of the cloud field is constant over the thickness. Intensity is generally referred to as ρ for satellite-to-irradiance models

while the same variable is generally refereed to as brightness (I) in computer vision. To obey conventional nomenclature, we use I for the brightness when referring to optical flow calculations. We can write the following equation:

$$I(x, y, t) = I(x + u\Delta t, y + v\Delta t, t + \Delta t), \tag{4.8}$$

where I indicates the brightness at the location (x, y) at time t of the η. Δt is the time passing between two consecutively available ηs. Intensity values, representing the brightness, are referred to as I_1 (first image) and I_2 (consecutive image). This is the basic equation defining the general approach to the detection of optical flow. For this equation, a set of additional constraints are needed to allow for solution. These additional constraints can be derived via several ways, e.g. correlation methods, gradient methods or regression methods [5]. According to [115] the spatially discrete classical optical flow objective function can be written as:

$$\begin{aligned} F(u, v) = \sum_{x,y} \{ & \varrho_D(I_1(x, y) - I_2(x + u_{x,y}, y + v_{x,y})) + \\ & \lambda[\varrho_S(u_{x,y} - u_{x+1,y}) + \varrho_S(u_{x,y} - u_{x,y+1}) + \\ & \varrho_S(v_{x,y} - v_{x+1,y}) + \varrho_S(v_{x,y} - v_{x,y+1})]\}, \end{aligned} \tag{4.9}$$

where F refers to the calculated flow field with the u and v velocities in the $x-$ and $y-$ direction. The variables ϱ_S and ϱ_D refer to the spatial and data penalty functions. The penalty function ϱ combines the data term (subscript D) that assumes constant image properties with the spatial term (subscript S) that models how flow is expected to vary across the image. The combination of these terms is optimized with an objective function. λ is the regularization parameter. Based on the study of [115], $\lambda = 3$ was used based on the performance on the Middelbury test. As suggested in [8], a Charbonnier penalty function is used as:

$$\varrho(x) = (x^2 + \epsilon^2)^{0.45}, \tag{4.10}$$

for both, data and spatial penalty in the x-direction (y-direction similarly), ϵ is the variation parameter. Based on the used implementation $\epsilon = 0.001$.

4.3.3 Streamline and velocity

A key part of the deterministic forecast is based on the calculation of the streamline of the cloud field, passing through San Diego in the CMV field. Streamlines in the 2-dimensional space are calculated by definition as:

$$\frac{dx}{u} = \frac{dy}{v}, \tag{4.11}$$

where dx and dy are line elements of the streamline of arc length. The local velocity in the x and y direction are indicated by u and v and derived from the CMV field. After this application, we obtain a streamline passing through the location of interest as a vector of the from $\vec{\zeta} = (x_1...x_n, y_1...y_n)$. It is straight forward to only use the upstream part of the streamline. After the streamline has been obtained, the average velocity vector for the streamline between two frames can be calculated by:

$$\vec{V} = \frac{1}{N}\sum_{i=1}^{N}(u_i, v_i), \tag{4.12}$$

where u and v are indicating the $x-$ and y-velocities of the CMV field covered by the streamline $\vec{\zeta}$ $(i \in \vec{\zeta})$. This leaves us with a speed in vector form derived in the unit pixel per frame $(px/frame)$. The magnitude of the velocity can be obtained by taking $|\vec{V}|$ rounded to the next integer. From here on, we know the directions of cloud flow as well as the associated velocities.

4.3.4 Forecasting model

After the calculation of the streamline and the associated average velocity, a forecast can be issued under the assumption that the identified CMV field between η_t and η_{t+1} will persist and that the velocity $\vec{V}$ can be extrapolated to the time horizon of interest (frozen cloud assumption). Based on these parameters, the conditions likely to propel to the location of interest, in the time horizon of interest, can be identified. The cloud conditions over this region can be translated to an irradiance forecast based on the satellite-to-irradiance model discussed above.

Therefore, the forecast can be issued according to the following:

$$\widehat{\rho}_t = \eta(\vec{\zeta}(x_n, y_n)), \tag{4.13}$$

where x_n and y_n are the vector elements of the streamline that are presumably propelling to the location of the forecast. This leaves us with an intensity value $\widehat{\rho}_t$ that can be used for the satellite to irradiance model. To identify the pixel on the streamline that is likely to be propelled to the location of interest, we have to define the shift parameter $a = 1 + |v| \cdot \Delta t$. In this study, predicted values will be superimposed with a $\widehat{\cdot}$ -symbol, e.g. $\widehat{GHI}$. Since the previously mentioned assumptions are a simplification for a significantly more complex system, the forecasting skill can be enhanced by taking surrounding pixels into account. The basic function for a spatial averaging filter for a region of p *by* q pixels is given by [87] as:

$$g(x, y) = \frac{1}{p \cdot q} \sum_k \sum_l f(x - k, y - l), \tag{4.14}$$

where $f(x, y)$ is the input region and $g(x, y)$ is the averaged output region, while k and l represent the size of the averaging window in the x- and y-direction, respectively. The averaging area was chosen to be square ($k = l$) and was optimized with the development set. It has been found to be $k = 8$ pixels for the $1h$-ahead forecast, $k = 10$ pixels for the $2h$ ahead forecast and $k = 11$ pixels for the $3h$ ahead forecast. Averaging over a larger area leads to the effect that not only intensity values in the range $22 - 44$ can occur but also other values. For this purpose, a lookup table with this range as been created according to equation 4.6. Since the input region consists of an intensity image η and the output region is supposed to be only one average intensity value ρ, we can insert equation (4.13) in (4.14) to obtain equation (4.15)as follows:

$$\overline{\hat{\rho}}_t = \frac{1}{N} \sum_{i=-L}^{L} \sum_{j=-L}^{L} \eta\big(\vec{\zeta}(x_a) + i, \vec{\zeta}(y_a) + j\big). \tag{4.15}$$

The forecast can then be issued by applying:

$$\widehat{GHI}_{t+\Delta t} = GHI_{CS,t+\Delta t} \cdot k_t(\overline{\hat{\rho}_t}). \tag{4.16}$$

Based on the results obtained above (see table 4.2), Model 2 is used as the satellite-to-irradiance model translating the obtained intensity η from equation 4.15 to $k_t(\overline{\hat{\rho}_t})$.

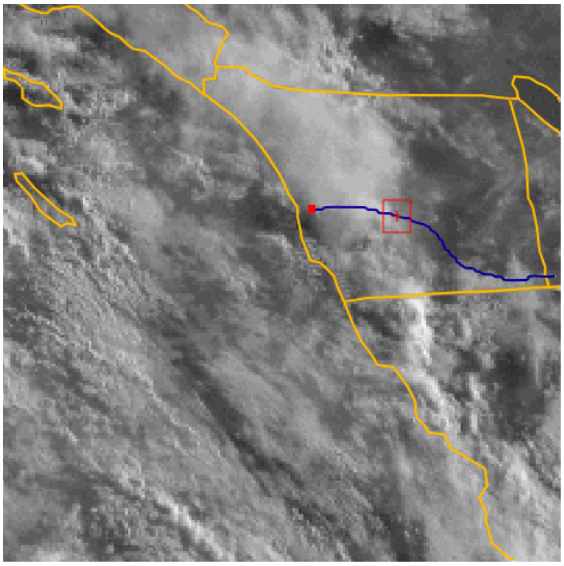

Figure 4.3: Example of a quality enhanced $Im_{t=2}$ frame with a superimposed streamline, calculated based on the flow velocity field. The solid line indicates the streamline while the small square shows San Diego (end of streamline). The dashed boxed area represents the region of interest that is likely to be propelled to San Diego within the next forecasting time step (here: 1h)

4.3.5 Persistence forecast

As a baseline forecast and an alternative when the streamline based forecast cannot be issued (e.g. due to corrupt satellite images), the persistence forecast is defined as:

$$\widehat{GHI}_{kt,t+\Delta t} = GHI_{CS,t+\Delta t} \cdot k_{t,t}, \tag{4.17}$$

where $GHI_{CS,t}$ refers to the GHI under clear conditions at the time of the forecast and k_t is the calculated clear-sky index with the latest available values. This forecast will be called k_t-persistence. This model is also used as a forecasting reference to evaluate the forecasting skill as discussed in section 4.4.2.

4.3.6 Decision heuristics

An essential step for the operational applicability of a forecasting model is the pre-classification of days to allow an automatized switch into different cloud cover modes. The heuristics to guarantee that the applied method is applicable for the existing and upcoming atmospheric conditions are implemented as follows:

4.3.6.1 Cloudless domain

In case that the domain of interest is free of clouds, it can be assumed that the clearness persists until clouds start to form or advect into the domain. The domain is assumed as clear if the number of cloudy pixels in the area is lower than 5 %. In this case, the model switches to k_t-persistence. This threshold was chosen empirically to allow for noise in the cloud identification process. The size of the input satellite image is a window of 200 by 200 pixels. Therefore, if $\sum_x \sum_y \beta < 2000$, the issued forecast is solely based on the clear sky model and the latest ground k_t value (k_t-persistence).

4.3.6.2 Negligible cloud movement speed

If the cloud movement is below 3 pixels per frame ($|\vec{V}| < 3px/frame$), the forecast algorithm also switches to k_t-persistence. This assumption can be made since it is very unlikely that clouds will be propelled in or out of the region of interest. These two assumptions have been found highly reliable in the implementation of operational forecasts.

4.3.7 Insufficient streamline

It can occur that a calculated streamline $\vec{\zeta}$ is shorter than the shift parameter (a) depending on the CMV field. In that case, the last available value of the streamline vector $\vec{\zeta}$ is taken as the identified pixel. This is only an approximation, nevertheless it is useful to continuously issue a forecast.

4.3.8 Data quality control

Occasionally, satellite images were not online, not downloaded correctly or the downloaded image was corrupt. Additionally, the stream of ground measurements could be interrupted by instrument malfunction, connectivity issues or maintenance work. If issues with the input data are detected, the forecasting system automatically switches to the k_t-persistence model. In this way, a forecast is continuously issued while the achieved skill for those days is zero. Approximately 10% of all days used for this study contained corrupt data of some sort and therefore have been excluded from the evaluation of the forecasting capabilities.

4.4 Model evaluations

To evaluate the performance of the proposed satellite-to-irradiance and forecasting model, they have been implemented for San Diego, California (longitude: 32.88; latitude: -117.23). The satellite-to-irradiance model has been evaluated for 100 days covering a time period from 20-March-2013 to 27-June-2013. The development of the forecasting method, including the implementation of the mentioned heuristics, has been done on a data set covering images and ground measurements from 13-October-2013 09:00 Pacific Daylight Time until 15-Jan-2014 15:45:00 for a total of 80 days in that period. This set is referred to as the development set. The method derived and implemented with the development set was then applied to a validation set covering the time period from 21-March-2013 09:00 until 07-July-2013 15:45 containing 110 days of data. The results obtained with both data sets for $1h$-, $2h$- and $3h$-ahead forecast horizons are discussed and analyzed in this section. A quantitative and qualitative error analysis, including a comparison to the results of previously proposed methods, covering the same forecast horizons are presented. The evaluation of the model is based on the metrics defined in chapter 3.

The statistics are calculated and presented in table 4.2 and 4.3. Additionally to the values calculated in Wm^{-2}, it is possible to calculate relative values of the forecast performance with the average ground truth value as a reference ($\overline{GHI}_{GT}$).

These relative values of the error are indicated with a prefixed r.

Additionally to the error metrics form chapter 2, the probability of occurrence of forecasting errors of different magnitudes, the cumulative distribution function (CDF) is used. The CDF of forecasting error magnitudes is be given by:

$$CDF_{Err.}(X) = P(Err. \leq X), \tag{4.18}$$

where $P(Err. \leq X)$ represents the probability that the error $Err. = GHI_{GT} - \widehat{GHI}$ lies below a certain X. The probability density function has been calculated for 75 probability increments (bins).

4.4.1 Satellite-to-irradiance model results

Results of Model 1 and Model 2 compared to ground measurements are shown in table 4.2, figure 4.4 and figure 4.5. Model 2 outperforms Model 1 continuously. Figure 4.4 shows the modeled data versus ground measurements for six consecutive days as an example for San Diego. While both models perform equally on clear days, the lookup table based model performs significantly better on overcast days. Table 4.2 shows the capabilities of the two satellite-to-irradiance models for the pre-processed satellite images, compared to the results from the SUNY model. Due to availability, the SUNY data covers the same days but for the previous year. After the exclusion of suspected outliers, the SUNY model shows similar characteristics to the results of our model. As shown in chapter 3, the SUNY model is intensively validated with ground measurements (e.g. [93, 35, 21, 121, 92]). This allows the assumption that both satellite-to-irradiance model approaches shown above are valid for all locations covered by $NOAA$ images if no snow cover is present. Therefore, this approach can be considered as a valuable tool for researchers to model GHI at any given location in North America near real time, while Model 2 outperforms Model 1. Figure 4.5 shows a scatter plot of GHI_{GT} versus GHI_{M1} as well as GHI_{GT} versus GHI_{M2}. Points where GHI_{M1} and GHI_{M2} coincide are highlighted. These values are equal since there are no clouds detected in the satellite image ($\rho = 0$). Errors of larger magnitude appear almost exclusively on the upper half of the 1:1 line. We can assume that

those errors are due to the image processing or cloud segmentation rather than in the satellite-to-irradiance model. During those times of large error magnitude, the satellite images appear to be clear while the GHI_{GT} signal is clearly attenuated by clouds.

Table 4.2: Comparison between results from the satellite-to-irradiance models used in this study and available data from the SolarAnywhere® data set. Note that the modeled data was derived for 2013 whereas the SUNY data was for 2012 due to availability. However, the mismatch of years does not interfere with the purpose to show the usability of the described and implemented satellite-to-irradiance model. Since the lookup table approach outperforms the other method, it is used for the proposed forecasting method.

San Diego	Mean Measured $[Wm^{-2}]$	Mean Modeled $[Wm^{-2}]$	MBE $[Wm^{-2}]$	$rMBE$ [%]	MAE $[Wm^{-2}]$	$rMAE$ [%]	$RMSE$ $[Wm^{-2}]$	$rRMSE$ [%]	$xcor$ [-]
NOAA GHI Model 1	493.49	495.73	-2.25	-0.46	71.72	14.53	124.53	25.24	0.934
NOAA GHI Model 2	493.49	516.78	-23.29	-4.72	61.72	12.51	107.41	21.77	0.95
SUNY *GHI*	385.31	455.16	-69.86	-18.13	106.40	27.61	213.14	55.32	0.825
SUNY *GHI* (outliers removed)	415.95	439.89	-23.95	-5.76	64.71	15.56	130.52	31.38	0.932

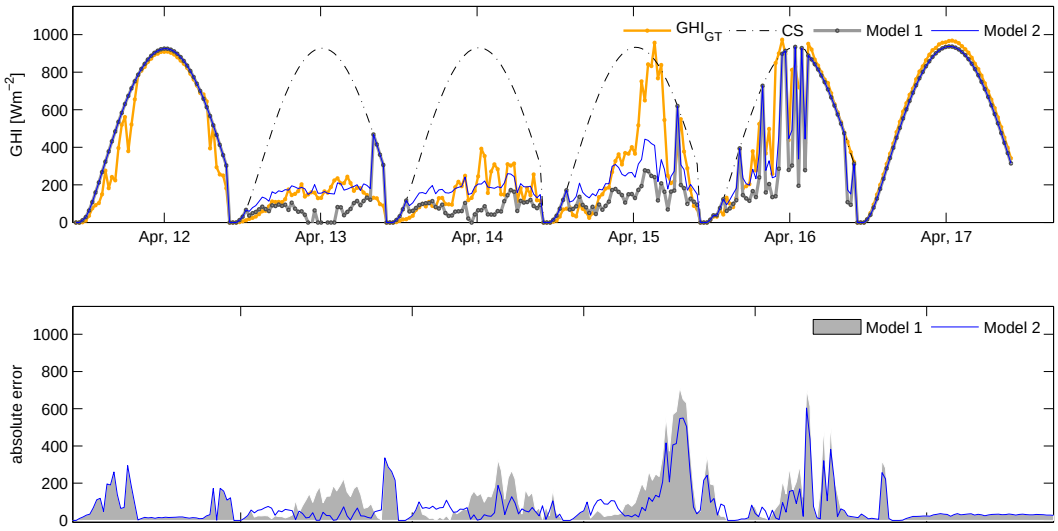

Figure 4.4: Comparison of six days in April 2013 of ground measured GHI_{GT} values (MFR-7) and values derived from the satellite-to-irradiance models described above (Model 1 and Model 2). Both satellite-to-irradiance models perform the same on clear days while the lookup table approach (Model 2) achieves better results on overcast days. CS indicates modeled GHI values under clear sky conditions.

4.4.2 Forecasting model results

The results of the described deterministic GHI prediction model are summarized in table 4.3 and visualized in figure 4.6 and 4.7. The skill achieved for continuous operation of this method is between 8% and 19% over the persistence model. The forecasting skill increases with the forecast horizon, mostly because the sky conditions are more likely to change over longer time horizons. Therefore, the usability of the k_t-persistence model decreases with increasing time horizon leading to a better relative performance of the forecast model. This also becomes clear by comparing the increasing surface between the CDF curves in figure 4.7 with increasing time horizon. The figure additionally shows that the achieved skill over persistence is only generated by reducing the occurrence of positive errors, while the proposed model is slightly worse than k_t-persistence for negative errors. The skill achieved with the proposed method is on the same order of magnitude

as of previously proposed satellite based methods ([76], [37]). However, the reported skill achieved with satellite images, ground telemetry and artificial neural networks (ANNs) are higher, between 18% and 25% ([76]). These methods rely heavily on ground measurements and extensive ANN training. The error for the $1h$-ahead (rMAE=8.83 % and 8.62 %) forecast is of lower magnitude than other solely deterministic models (e.g. [38] rMAE=12-15 %). A comparison of our results to the results mentioned by [101] suggests that our new method can be used in addition or as an alternative and provide similar or better results, depending on the location specific irradiance characteristics. Additionally, the temporal resolution of this forecast with an update every 15 minutes is higher than for the cited studies [38, 37, 76]. Figure 4.6 provides an example of the results of the proposed forecasting model compared to ground truth values and the k_t-persistence model. This sequence of consecutive days has been chosen as an example because it covers various sky conditions. In general, the forecasting method reduces the error compared to k_t-persistence. This characteristic is consistent with the positive forecasting skill for all forecast horizons (see table 4.3). However, there are several instances when rather large ramps in the GHI_{GT} are not predicted correctly. For example, on 16-October-2013 there is an non-captured strong ramp event in the GHI_{GT} signal mid-day. On that instance, the η appears to be clear. Therefore, we can assume that the image capturing or processing was erroneous. The other inaccuracies are presumably based on the simplifications made that do not completely hold true under real world conditions. Inaccuracies in the satellite-to-irradiance model can be a source of additional error. Due to the way of operation of this forecast, the forecasting performance including the forecasting skill is limited by the performance of the satellite-to-irradiance model.

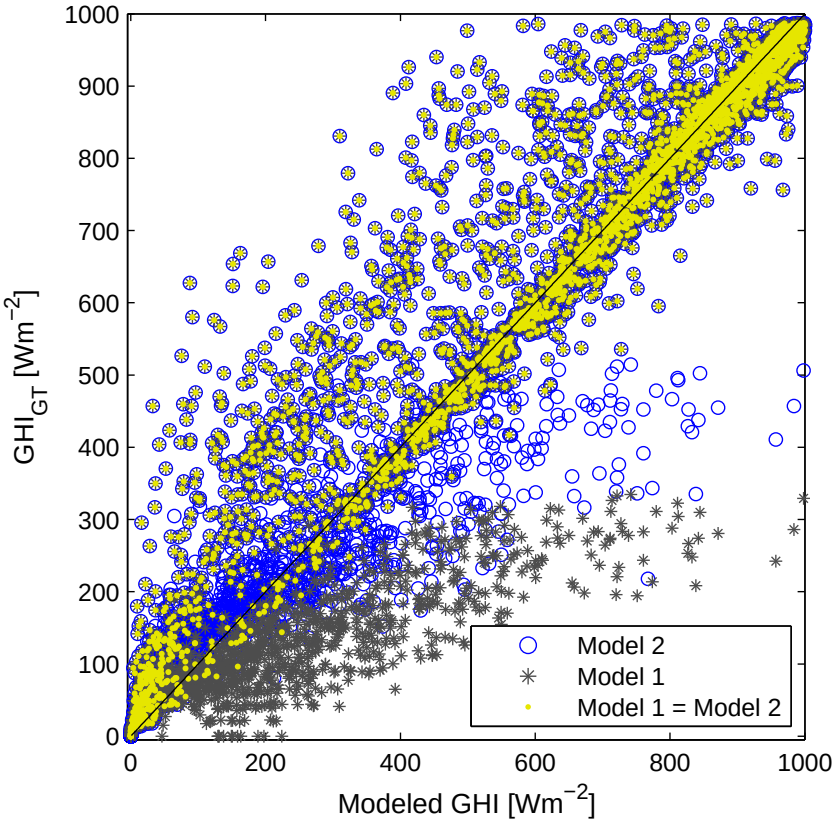

Figure 4.5: Scatter plot of GHI_{GT} against values obtained with GHI_{M1} and GHI_{M2}. Model 2 is generally smaller than from Model 1. Model 1 tends to understimate irradiance under overcast conditions. This is due to the fact that for Model 2 $k_{t,min} = 0.16$ while Model 1 allows for $k_{t,min} = 0$ which cannot occur during daylight times. Yellow markers indicate that values from Model 1 equal values of Model 2, obtained when $\rho = 0$ in the satellite image. In these cases, the resulting errors are large and due to undetected clouds in the satellite image.

Table 4.3: Results of the deterministic forecasting model, for forecast horizons of $1h$-, $2h$- and $3h$-ahead, results from k_t-persistence and the forecast skills.

	Data set size	Mean Forecast	Mean Measured	MBE	$rMBE$	MAE	$rMAE$	$RMSE$	$rRMSE$	$xcor$	Skill
Development Set	[-]	$[Wm^{-2}]$	$[Wm^{-2}]$	$[Wm^{-2}]$	[%]	$[Wm^{-2}]$	[%]	$[Wm^{-2}]$	[%]	[-]	[-]
60 min Sat	1371	442.21	442.32	-0.12	-0.03	39.04	8.83	78.98	17.86	0.90	9.01
k_t-persistence	1371	436.06	442.32	-6.26	-1.44	42.06	9.64	86.80	19.91	0.88	
120 min Sat	1180	427.53	441.25	-13.72	-3.21	45.10	10.55	86.14	20.15	0.89	11.64
k_t-persistence	1180	427.53	417.82	9.71	2.27	50.55	11.82	97.49	22.80	0.86	
180 min Sat	1019	285.43	275.94	9.49	3.32	38.90	13.63	71.34	24.99	0.93	18.74
k_t-persistence	1019	267.47	275.94	-8.47	-3.17	46.95	17.55	87.73	32.80	0.89	
Validation Set											
60 min Sat	2026	773.73	759.43	14.29	1.85	66.66	8.62	129.68	16.76	0.83	8.10
k_t-persistence	2026	745.69	759.43	-13.74	-1.84	73.99	9.92	141.11	18.92	0.81	
120 min Sat	1680	762.61	753.33	9.28	1.22	75.35	9.88	144.98	19.01	0.79	11.32
k_t-persistence	1680	730.99	753.33	-22.35	-3.06	88.60	12.12	163.48	22.36	0.74	
180 min Sat	1336	601.03	585.38	15.65	2.60	83.43	13.88	139.92	23.28	0.83	15.77
k_t-persistence	1336	568.04	585.38	-17.34	-3.05	99.03	17.43	166.11	29.24	0.76	

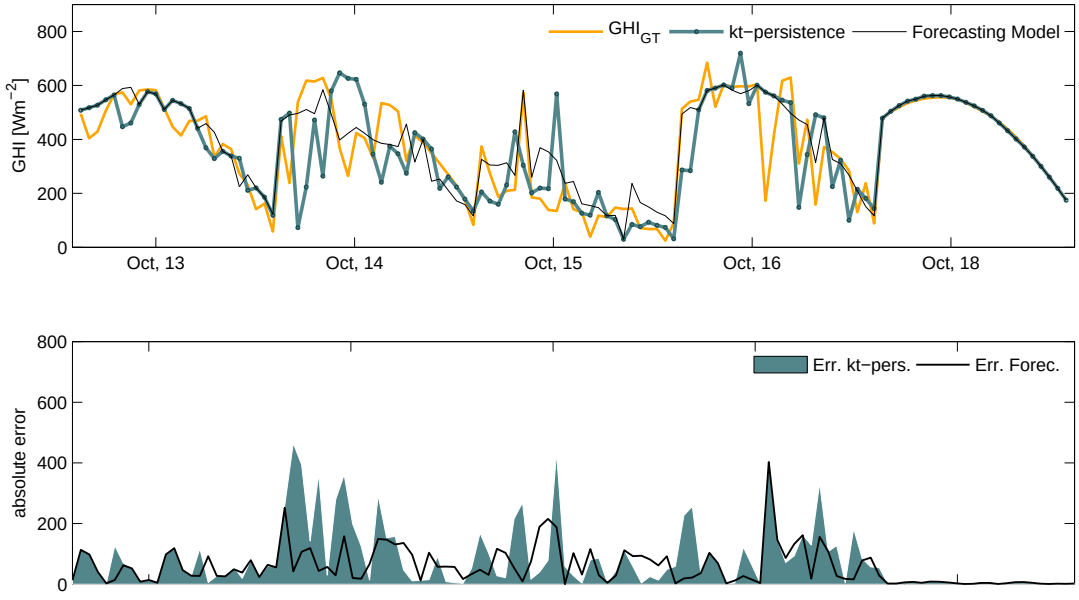

Figure 4.6: Comparison of five example days in October 2013 of ground measured GHI_{Gt}, results from the proposed $1h$-ahead forecasting method and results from the k_t-persistence model. The second part of the figure shows the error of both models. The proposed forecasting model reduces the error between ground truth and the forecasted values compared to the error of k_t-persistence.

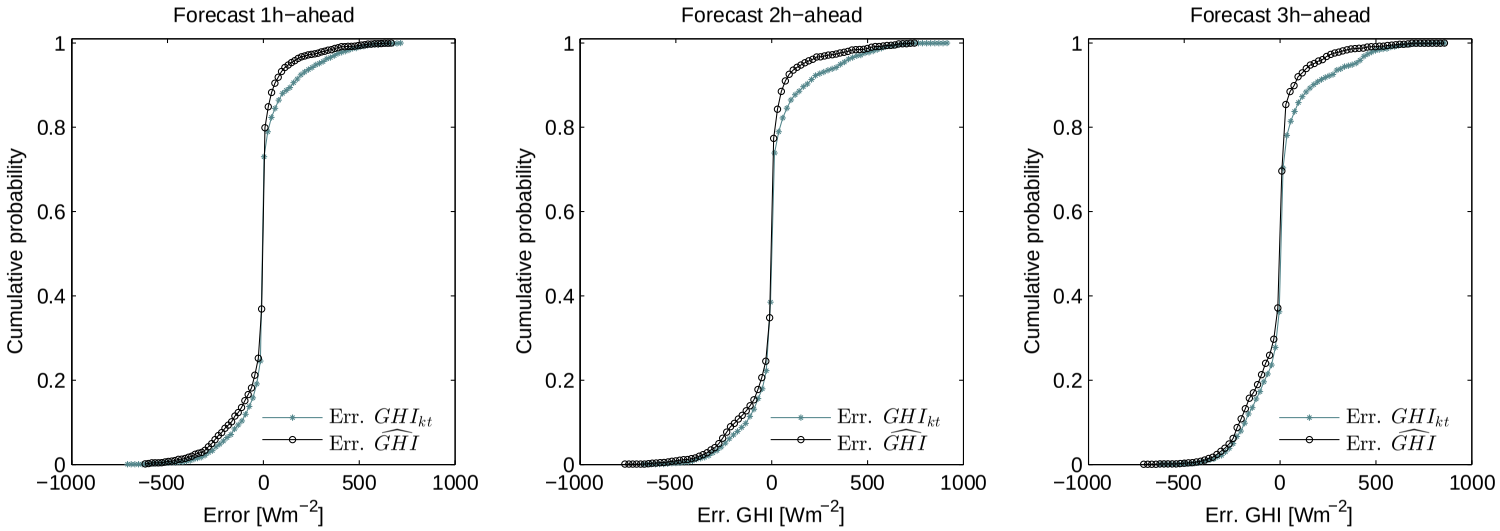

Figure 4.7: Cumulative distribution function for the errors obtained with the validation set for forecast horizons $1h$, $2h$ and $3h$ ahead, respectively. The overall performance increases with the time horizon (the surface between the curves increases). This is consistent with the increasing forecasting skill for longer forecasting horizons. In general, the errors from forecasting model are smaller than for the k_t-persistence model. However, the major improvement of the forecasting model over the k_t-persistence model is for positive errors of small to medium magnitudes (0 to $500Wm^{-2}$).

4.5 Summary

In this chapter, a remote sensing-based GHI forecasting methodology was proposed to predict 15 minute averages of GHI up to $3h$ in advance. This forecast method is based uniquely on satellite images and ground measurements with no other inputs. The overall methodology includes the following main steps: (1) Application of a fast cloud segmentation method on pre-processed satellite images. The method works reliably for optically thick clouds that are easily distinguishable from the background while problems with optically thin (opaque) clouds remain. Since the attenuation of GHI by optically thin clouds is limited, this caveat of the method introduces only limited errors to the forecasts (however, the attenuation of DNI through optically thin clouds are non-negligible). (2) Calculation of cloud movement vectors between two satellite frames with the optical flow algorithm. For cloud tracking, the optical flow approach is found to be superior to PIV and DCA. A direct evaluation of the cloud tracking method is not possible due to the lack of ground truth data for cloud velocities. However, the fact that a positive forecasting skill is achieved encourages the assumption that cloud tracking based on optical flow yields reasonable values for cloud transport. (3) Based on this cloud movement vector field, the streamline passing through the region of interest and the average speed is calculated. Therefore, a region of pixels that are most likely to move to the region of interest can be identified. (4) A satellite-to-irradiance model translates the intensity values of these pixels into the GHI forecast. Since this method relies on the accuracy of the satellite-to-irradiance model, a novel, fast processing approach to enhance the satellite-to-irradiance model with ground truth is proposed. The novelty of this approach lies in the utilization of online near-real time available pre-processed images combined with the fast assignment of clear sky index values from a lookup table. The provided lookup table can be used for all locations covered by the satellite images. If ground measurements are available for a specific location, the lookup table can easily be created to enhance accuracy. The proposed satellite-to-irradiance model outperforms the linear approach by reducing the $RMSE$ form $124.53 Wm^{-2}$ to $107.41 Wm^{-2}$.

While substantial heuristics have been used to achieve the highest possible fore-

casting skill on the development set, the implementation has been applied to an independent test set. This approach yields a forecasting skill ranging from 8% to 19% over persistence for San Diego for forecast horizons between 1-hour of up to 3-hours. Previously reported forecasting skills for the same forecast horizons are on the same order of magnitude between 5% and 25%, however they are not directly comparable to the results presented here due to different test locations. San Diego is a notoriously difficult region to forecast due to frequent inversion layers on the Southern California coast. While other methods yield comparable forecasting skills, the intra-day forecasting system proposed here is especially valuable due to the low computation costs and because it is solely based on satellite images and ground measurements. Our calculations also show that there is room for further optimization of this method, particularly in relation to the detection of optically thin clouds. Besides the need for accurate intra-day prediction, there is a need to predict solar irradiance values up to several days in advance. The next chapter addresses the method and value of day-ahead DNI forecasts.

Note: This chapter contains work, previously published in:

- L. Nonnenmacher, C. F. M. Coimbra, "Streamline-Based Method for Intra-Day Solar Forecasting Through Remote Sensing", *Solar Energy*, 108, pp. 447-459, 2014.

Chapter 5

Day-Ahead solar irradiance forecasting

As shown in chapter 4 and the literature, solar forecasting is a proven concept to reduce the uncertainty in the solar resource and hence, improves the grid integration characteristics, ultimately leading to higher market penetration of weather-dependent solar without resorting heavily on energy storage [52, 57, 71, 40]. So far, most studies on solar forecasting primarily focused on the prediction of global horizontal irradiance due to larger installed capacity of photovoltaic systems in most countries. CSP has roughly the same potential as PV on marginal lands in the U.S., and a higher potential than wind (4.5 PWh from PV, 4 PWh from CSP, 2.7 PWh from wind [83]). Rapid advances in concentrated solar power (CSP) technologies and the recent deployment of several utility-scale, grid connected CSP facilities reiterate the need for accurate predictions of direct normal irradiance for all time horizons. The day-ahead forecasting horizon is important in markets with day-ahead power trading [102] since they prevent false market bids and associated penalty charges (where applicable). While many NWP models directly provide GHI forecasts as a public output variable, day-ahead DNI forecasts are rarely available and only recently was included as an output of some NWP models. In this chapter, we propose and evaluate two models that utilize NWP output data as an input to predict hourly values of DNI for the day after, initiated at 4pm local time of the current day, out to 16-32 h ahead predictions. The first ap-

proach is the prediction of DNI based on a high performing GHI-to-DNI estimation model. The second approach directly translates predicted cloud cover into DNI by attenuating a clear sky model with cloud cover predictions. The clear sky model of this study uses monthly turbidity averages. Predicted cloud cover is used from the Regional Deterministic Prediction System (RDPS) and the North American Mesoscale (NAM) model (provided by the Canadian Meteorological Centre (CMC) and National Oceanic and Atmospheric Administration (NOAA), respectively).

The value of information for both DNI forecasting models is analyzed with pricing time-series for the Day-Ahead Market (DAM) and the Real Time Market (RTM) from the California Independent System Operator (CAISO). The value of both models is compared to a persistence model under three different grid-interconnection scenarios with and without deviation penalty charges. Based on the forecasting skill, value and NWP data availability, the proposed models can be utilized to serve as a benchmark for the accuracy of more complex and optimized DNI (multiple) day-ahead forecasting approaches.

This chapter is structured as follows: first, a literature review is presented in section 2 that summarizes relevant previous work for both, day-ahead GHI and DNI predictions. Section 3 describes the utilized data sets and the NWP models. Section 4 describes the proposed methods to forecast hourly values of DNI one day in advance. Section 5 includes error metrics, model evaluations and general findings. Section 6 shows the value of information of the proposed forecasting method under three interconnection scenarios. Section 7 contains the final conclusions of this chapter.

5.1 Previous work

This section covers relevant previous work for day-ahead DNI (and briefly GHI) solar forecasting methods. Here, we focus on DNI prediction, however a review of day-ahead methods for GHI forecasting studies since May, 2013 is included (one of our models to predict DNI is solely based on GHI prediction as an input). GHI is among the output variables of many operational NWP models. Due to

its known strength for predicting future states of the atmosphere, most (multiple) day-ahead forecasts are based on NWP. For solar forecasting, various NWP output parameters are used (e.g. pressure, humidity, wind speed, temperature etc.) and processed with various methods (e.g. machine learning methods, probabilistic analysis etc.). Previously, 12 studies covering (multiple) day-ahead forecasts of solar irradiance and/or power output based on various exogenous and endogenous variables are summarized in [52]. However, most previous studies covering the day-ahead time horizon focus on the prediction of GHI. A short discussion on the relevant GHI studies is included in section 5.1.1 and table 5.2 summarizes the latest NWP based GHI prediction approaches.

An extensive review of DNI forecasts with its application to solar thermal output was published by [63]. Previous studies, relevant for the day-ahead predictions of DNI are summarized in table 5.1 and are discussed in section 5.1.2. Section 5.1.3 discusses previously proposed methods to model DNI based on GHI.

5.1.1 Evaluation of NWP GHI predictions

Model 1 for DNI forecasting is based on GHI predictions. As stated previously, several NWP models provide GHI forecasts as an operational output. GHI as an NWP output variable was historically included as a control variable for the radiative transfer model of the NWP model [81]. The most common model to derive GHI in NWP is based on the parameterization approach by [113]. GHI predictions from NWP models are also referred to as down-welling surface short-wave radiation flux. Many previous studies focused on the evaluation of the accuracy of GHI from different NWP models, for different locations and various solar climates. The performance of multiple day-ahead GHI forecasts based on the NAM, GFS (Global Forecast System) and ECMWF (European Center for Medium-Range Weather Forecasts) model are well known [81, 79, 109, 94]. A general trend to overpredict clear conditions appears to be common.

Table 5.1: Summary of previous studies covering (multiple) day-ahead DNI forecasting methods with covered forecasting horizon, applied method and validation location.

Authors	**NWP**	$\widehat{I}$	**Horizon**	**Methods**	**Locations**
[117]	-	DNI		NWP output as radiative transfer model input	US Southern Great Plains
[61]	-	DNI	1d	MOS	Andalusia, Spain
[62]	WRF	GHI & DNI	1-3d	GHI evaluation, DNI modeling based on GHI forecast and satellite retrievals	Andalusia, Spain
[72]	NDFD	GHI & DNI	1-6d	ANN GHI and DNI modeling	Merced, California, USA
[7]	EURAD CTM	DNI_{CS}	2-3d	NWP and remote sensing based prototype irradiance forecasting system	Various locations, Europe

In general, the GHI predictions issued from the ECMWF model were found to be the most reliable. Model output statistics (MOS) is a proven method to reduce the biases associated mainly with the GHI output from the NAM and GFS model. Significant prediction improvements for intra-day and day-ahead forecasts are possible with an improved cloud-assimilating, high-resolution NWP model based on the Weather and Research Forecasting model [79] ([79] was specifically implemented to forecast the characteristic coastal low-altitude clouds in California). NWP output as an input for various radiative transfer models are used by [109] to validate the performance for three Italian sites. They found a relative mean absolute error (rMAE) ranging from 11% to 17% and a relative root mean square error (rRMSE) from 21% to 28% for data from all sites. The accuracy of solar irradiance forecast based on the mesoscale model from the Japan Meteorological Agency (JAM) for the Japanese Kanto region was evaluated in [94] Their findings include a mean bias error (MBE) of GHI in the range of $-50 Wm^{-2}$ to $50 Wm^{-2}$ for yearly data. The RMSEs have been found to be in the range of $90 Wm^{-2}$ to $150 Wm^{-2}$ with a strong seasonal dependence. Additionally, they related the error in the forecast to the occurring cloud type and cover. They showed that stratocumulus clouds cause an overestimation of GHI while significant underestimation is frequently related to the occurrence of cirrus clouds. The GHI forecasting capabilities for of 10 North American locations was investigated by [96] with application to photovoltaic power output forecasting. Their study is based on the Global Environmental Multiscale model from the Canadian Meteorological Centre from the high-resolution regional run for up to 48 h ahead with variable spatial resolution. Their findings include that GHI forecasts provides a significant performance gain compared to the reference persistence model as well as a reduction of RMSE through spatial averaging. The most recent and extensive evaluation of multiple NWP based GHI forecasting approaches with focus on the end-use accuracy is available in [102]. Their key findings include a better performance of the ECMWF model compared to the WRF models for all sites across North America and Europe.

Table 5.2: Summary of NWP based solar forecasting studies covering (multiple) day-ahead forecasting methods with important input parameters and validation location, published within a year (between June 2013 and June 2014). A comparison with table 5.1, that contains all important DNI studies published within seven years, shows that substantial more effort is made covering the day-ahead prediction of GHI compared to DNI.

Authors	**Numerical model**	$\widehat{I}$	**Horizon**	**Method**	**Location**
[79]	NAM	GHI		Satellite image based direct cloud assimilation in the NWP initial conditions	San Diego, California
[128]	PEARP	PV Output		Quantile regression forecast models, ensemble exploiting, post processing	28 PV arrays in France
[102]	GEM, ECMWF, WRF	GHI	1-7d	NWP GHI output evaluation	US, Canada, Europe
[109]	IFS/ECMWF, GFS/NCEP, LAMI, RAMS	DIF & GHI	3 days	NWP as input to radiative transfer model (six schemes)	Italy (three sites)
[94]	JAM	GHI	33h	NWP GHI output evaluation only	Kanto Region, Japan

5.1.2 NWP based DNI forecasting

Five journal publications known to the authors focused on the topic of (multiple) day-ahead DNI forecasts (see table 5.1). The key findings of these studies are summarized in this section. An additional, recent review of methods covering all DNI time horizons was published by [63].

5.1.2.1 WRF post-processing

A study explicitly focusing on an operational DNI forecast based on NWP data was published by [62]. Their proposed model is a physical post-processing scheme that utilizes multiple outputs from the WRF model and satellite data. The utilized exogenous variables are water vapor, water clouds and ice clouds data output of the WRF model as well as aerosol and ozone data derived from satellites. [62] compared results of their model with a method based on a clearness index (k_t) to identify three different sky conditions, clear ($k_t > 0.65$), cloudy ($0.4 < k_t < 0.65$) and overcast ($k_t < 0.4$). It was found that the WRF model tends to overestimate GHI by approximately 10%. The performance of their DNI model was validated with DNI data from two ground stations. A DNI rRMSE varying between 20% and 400% was found with a strong dependence on the cloud conditions.

5.1.2.2 NWS (NDFD) and ANN based forecasting

A method utilizing National Digital Forecasting Database (NDFD) retrievals, provided by the National Weather Service (NWS) as inputs to Artificial Neural Networks (ANNs) was proposed by [72]. While the NDFD is mainly based on NWP predictions, the data is compiled using predictions from all 122 NWS weather forecast offices. The weather forecast offices interpret NWP data manually, therefore, a human factor is involved in this data set. A key contribution of [72] is the optimized input selection based on a gamma test in combination with a genetic algorithm to forecast GHI and DNI for multiple days ahead. In the training set, the model with all derived inputs (maximum temperature, temperature, dew point temperature, relative humidity, sky cover, wind speed, wind direction, probability of precipitation, minimum temperature, solar elevation angle and normalized

hourly angle) performed the best. For the test set, models with less inputs outperformed the model with all inputs. This implies that more input parameters not necessarily enhance forecasting capabilities. For GHI, the model using sky cover, probability of precipitation, minimum temperature and sun elevation angle performed the best. For DNI, best results have been achieved by utilizing maximum and minimum temperature, dew point temperature, sky cover, probability of precipitation and normalized hour angle. The method has been evaluated with measurements from one location (Merced, California). This location is especially valuable since the data for our study also includes Merced, CA. Hence, the results can be compared.

5.1.2.3 State-of-the-art day-ahead CSP forecasting

A comparison of DNI predictions based on model output statistics (MOS) with a simple persistence model is available in [61]. Exogenous inputs of the MOS model are solely site-specific historical NWP outputs. Their DNI predictions have been obtained from the commercial provider Meteólogica. NWP data for this commercial product was obtained from both, ECMWF and High Resolution Limited Area Model (HIRLAM) provided by the Spanish national meteorological center. Findings of this study include a general improvement of the MOS model over the persistence model in terms of RMSE and rRMSE but with strong performance variations between different years which we consider unexpected in magnitude. Additionally, the study shows the reduction of penalty charges for more accurate power output prediction. Substantial improvements are reported in that study (up to 50% in terms of reduction of penalty charges).

5.1.2.4 Sun's estimation scheme

[117] proposed a fast estimation scheme to model DNI based on a radiative transfer model. NWP and satellite data can be used as an input to the radiative transfer model. The exogeneous input parameters utilized in their fast estimation scheme are precipitable water vapor, total column ozone, carbon dioxide mass mixing ratio, cloud water/ice visible optical depth, total cloud amount, surface

pressure and solar zenith angle. While the fast estimation scheme is supposed to be capable of issuing a prediction of DNI for several upcoming time horizons, their evaluation is solely based on instantaneous observation. However, the value of this study lies in the computational inexpensive approach to highly accurate DNI assessment based on NWP data. While the authors state the feasibility of this multi-input approach for an operational (multiple) day-ahead forecast, the detailed assessment of its performance is not provided. It presumably depends heavily on the accuracy of the NWP model.

5.1.2.5 AFSOL system

[7] developed a modeling system for the prediction of irradiance for application in the solar energy community. The developed system is called Aerosol-based Forecasts of Solar Irradiance for Energy Applications (AFSOL). This AFSOL system was developed for the prediction of GHI and DNI at high temporal resolution. The main routine of the AFSOL system is based on a radiative transfer library calculating ground irradiance based on atmospheric scattering, absorption and surface properties. The system varies the standard atmosphere of the radiative transfer model with additional input of aerosols, column-integrated atmospheric water vapor and cloud information. These inputs are taken from the ECMWF NWP model, air quality model outputs and satellite data. The focus of this study was placed on the accurate prediction of clear sky irradiance. For DNI, their findings include a reduction in RMSE compared to forecasts solely based on ECMWF outputs for clear sky situations. For cloudy conditions, the ECMWF outperforms the AFSOL irradiance forecast. For accuracy improvements, a hybridization of both approaches is suggested. The AFSOL system is utilized by [124] to study the use of DNI forecasts for optimized operations of solar thermal plants. Economic benefits based on the utilization of the AFSOL system were shown.

5.1.3 GHI-to-DNI modeling

Several models to derive DNI from GHI time-series have been proposed in the past, in part due to the fact that GHI measurements are significantly eas-

ier to obtain than DNI measurements. [3] compared the performance of seven models translating hourly GHI into hourly DNI values. In short summary, two different categorizes of GHI-to-DNI models exist, simple decomposition models and more advanced atmospheric transmittance models. While decomposition models are based on the calculated ratio of measured GHI to a reference (e.g. GHI/I_c solar constant), atmospheric transmittance models utilize various atmospheric parameters to estimate clear sky DNI attenuation through the atmosphere. Their findings include a generally better match of modeled DNI values with decreasing cloud cover. Additionally, they point out that there are difficulties in all approaches to parametrize the effects of clouds on DNI. The long term rRMSE was found to be in the narrow range of 20 and 22%. Their recommendations include the usage of decomposition models, if no turbidity information is available. A validation of three GHI-to-DNI models against 100,000 station hours of ground data is available in [48]. The performance of the three models varies between 24 and 33% with only small differences between the models. It appears that the characteristics of the location have a stronger impact on the accuracy than the choice of the model (concluded based on table 3 in [48]). Based on these findings, a GHI-to-DNI model based on a location specific regression model is presented in section 5.3.2 and used for Model 1.

5.2 Data

5.2.1 Ground measurements

Large scale concentrating solar power applications usually come with high quality solar irradiance instrumentation running on high sampling rates. For this study, DNI ground measurements, with coinciding NAM and RDPS forecasts, have been available from solar observatories in Berkeley, CA; Davis, CA; Merced, CA and San Diego, CA. Locations and deployed instruments are summarized in table 6.1. For a more detailed description of the deployed instruments, the local microclimates and the location characteristics, see chapter 2. The following validation data set sizes are used: 382 days for Berkeley, 404 days for Davis, 266 days for

Merced and 603 days for San Diego.

5.2.2 Acquisition of RDPS data

Raw data from the regional deterministic prediction system (RDPS) can be accessed via the Canadian Meteorological Centre (CMC) servers as GRIB2 files. The RDPS numerical data output has a 10 km resolution covering North America including adjacent oceans. The latest RDPS output for the locations of interest has been downloaded as sky charts provided online with an automated download script. The variable from RDPS referring to cloud cover in the sky charts is called total cloud, which is presented as column values given in 2.5 % increments. Therefore, the RDPS output distinguishes between 40 different levels of cloud cover in a grid element. The color coded representation of cloud cover in the sky chart has been translated into the corresponding percentage value via an automated image processing script. The cloud-cover to irradiance model is discussed in section 5.3.3.

5.2.3 Acquisition of NAM-WRF data

Another NWP system covering out regions of interest is the North American Mesoscale Weather Research and Forecasting (NAM-WRF) model in its current operational form as a Non-Hydrostatic Mesocale Model (WRF-NMM). Data has been downloaded as gridded files for North America for the time covered in this study from the 0:00 UTC run (00:00Z). The data sets representing the next 16 to 32 hours have been degribbed for the studied locations. To create matching data sets, data from all sources are time matched and night values (Solar Elevation Angel$< 5°$) excluded.

5.2.4 Acquisition of locational marginal pricing data

For the value of information analysis presented in section 6, time series of locational marginal prices (LMP) for the Day-Ahead Market (DAM) and the Real-Time Market (RTM) are used in settling scenarios. This data was downloaded for

nodes in Merced and Davis via the CAISO open access same-time information system. For the DAM, hourly values are directly accessible while the RTM provides data in 5 minute intervals. Averaging and time-matching was applied to synchronize the different data sets.

5.3 Methods and models

As discussed above, previous studies focused on the prediction of GHI from NWP data. However, little effort has been made to predict DNI based on NWP. To fill this gap, this section shows two simple models to derive DNI from NWP output, either cloud cover or GHI. Model 1 is a GHI-to-DNI model, Model 2 is a cloud-cover-to-DNI model. For completeness, a cloud-cover-to-GHI model is additionally included. Cloud and clearness index are defined since they are important modeling steps and commonly used in the solar energy assessment and forecasting. A simple persistence model with no exogenous inputs is also described since it is commonly used as a reference [72, 61]. The definitions from cloud (k_t) and clearness index (k_b) from chapter 3 are used frequently in this chapter.

5.3.1 Persistence GHI & DNI model

In chapter 4, a definition for intra-day persistence based on the persistence of k_t is given. The following persistence model is used for day-ahead predictions:

$$\widehat{GHI}_{D+1} = GHI_{Gt,D}, \tag{5.1}$$

and

$$\widehat{DNI}_{D+1} = DNI_{Gt,D}, \tag{5.2}$$

where the subscript D indicates the day. Hence, we assume that the time series from the previous day will persist and hence present the forecast for the upcoming day.

5.3.2 GHI-to-DNI model (Model 1)

As shown in section 5.1.3, several models with location dependent performance can be used to estimate DNI from GHI. A high performing GHI-to-DNI model, based on a second order polynomial fit is used to transfer the clear sky index k_t to k_b. After this step, NWP based GHI forecasts can be translated to DNI forecasts. The polynomial is $k_b = a_1 k_t^2 + a_2 k_t + a_3$, where k_t is the clear sky index and a_i are the coefficients. Additionally, the threshold $k_b(k_t < 0.4) = 0$ is applied (under overcast conditions, DNI is zero). The parameter k_b can then be used to calculate predicted DNI as:

$$\widehat{DNI} = DNI_{CS} \cdot \widehat{k_b}, \tag{5.3}$$

where $\widehat{DNI}$ is the predicted DNI based on $\widehat{k_b}$ which is a function of predicted GHI. Table 5.3 shows the coefficients for the polynomial regression as well as the rRMSE of the GHI-to-DNI model, obtained for the different locations. These errors are similar or better than characteristic errors reported in the literature [69, 99, 48]. This model it referred to as Model 1 (M1).

5.3.3 Cloud-cover-to-irradiance model (Model 2)

As a simple approach to model GHI from predicted cloud cover percentage, we can utilize a linear model based on the cloud index. For GHI, we can assume a minimum $k_{t,min} = 0.17$. This value is the average value of the 10th percentile for the lowest occurring k_t-values in a data set covering several locations with a total of over 5 years of data. The upper bound is given by $k_{t,max} = 1$. Therefore, the equation we can write is:

$$\widehat{GHI}(cc) = GHI_{CS} \cdot (k_{t,min} + 0.0083 \cdot (100 - \widehat{cc})). \tag{5.4}$$

Here, $\widehat{cc}$ is the NWP cloud cover output variable, either from the NAM or the RDPS model. This model is a slightly modified version of the in [103] proposed approach. This approach is used as a reference GHI forecast in [72]. While the focus of our study is DNI, results of this model for GHI are additionally included

Table 5.3: Coefficients (a_1, a_2, a_3) of the second order polynomial regression to model k_b based on k_t. The rRMSE shows the modeling performance of the GHI-to-DNI model for the four locations. These errors are at par or slightly better than the errors for the generic models reported in the literature.

Location	a_1	a_2	a_3	**rRMSE** [%]
Berkeley	2.073	-1.119	0.2075	18.9
Davis	1.399	-0.208	-0.075	17.1
Merced	1.745	-0.822	0.047	19.0
San Diego	2.122	-1.333	0.2075	21.4

as a reference. As for GHI, Model 2 for DNI directly relates the predicted cloud cover percentage to attenuate the expected clear sky DNI. Therefore, we can write:

$$\widehat{DNI}(cc) = DNI_{CS} \cdot \frac{100 - \widehat{cc}}{100}, \tag{5.5}$$

where again, $\widehat{cc}$ is the predicted cloud cover and DNI_{CS} is the clear sky DNI. Cloud cover predictions from two different NWP models are used. As an input, Model 2a (M2a) utilizes RDPS, while Model 2b (M2b) is based on NAM input.

5.4 Evaluation and results

5.4.1 Statistical results

Based on the metrics defined in section 3.3, a summary of the statistical results achieved with the proposed models are shown in table 5.4 and 5.5 for all 4 locations. The average cloud index ($\overline{k_t}$) is included, representing the ratio of clear versus cloudy conditions. Additionally, the table contains average ground truth values ($\overline{DNI}_{Gt}$ and $\overline{GHI}_{Gt}$). Since various validations for GHI forecasts are available, the performance for GHI has additionally been added to table 5.4 as a reference. The error of the NAM GHI forecast, M1) is within the range of the previous studies (e.g. [94, 81]). The NAM GHI output values show the overestimation described by [81]. The cloud-cover-to-GHI model with NAM predicted cloud cover usually performs significantly lower than the cloud-cover-to-GHI model with

RDPS predicted cloud cover and the NAM GHI output variable (M1). A correlation analysis revealed a very low correlation of NAM predicted cloud cover to k_t, mainly due to frequently higher prediction of cloud cover than derived from the RDPS models.

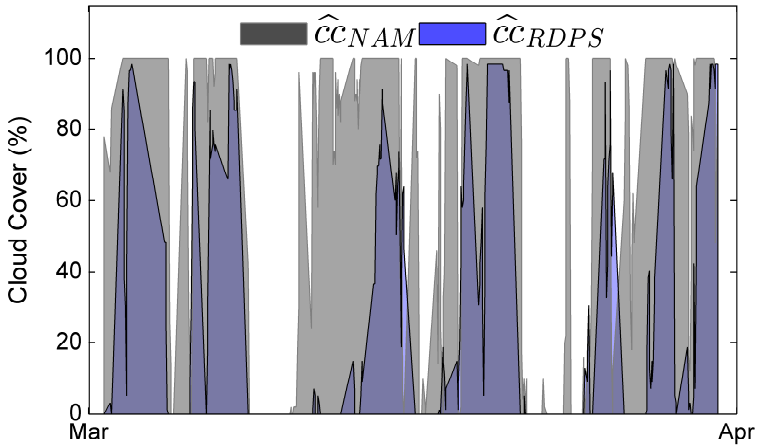

Figure 5.1: Comparison of predicted cloud cover in percent from the RDPS ($\widehat{cc}_{RDPS}$) and NAM ($\widehat{cc}_{NAM}$) NWP models for day-ahead forecasts as an example for March 2013 for the location of Berkeley, CA. The RDPS model ($\widehat{cc}_{RDPS}$) predicts significantly less cloud cover than $\widehat{cc}_{NAM}$. The impact of the NWP input model for the performance of the cloud-cover-to-DNI model is dependent on the location.

For DNI, Model 2 generally outperforms Model 1 independent of which NWP model is used as an input. In general, the NAM model tends to predict higher cloud cover than the RDPS model (see figure 5.1). This is likely due to the different penalties for cloud prediction given by the NWP models since they serve different purposes. In our experience the cloud dissipation times are challenging to model for all NWP models. While the RDPS cloud cover prediction is specifically a cloud forecast for astronomical purposes, the NAM model evolved as a generic tool for meteorological applications. This discrepancy in cloud cover prediction is reflected in the long term results shown in table 5.4. The RDPS performs better at locations with low cloud cover ($\overline{k_t} > 0.8$) while the NAM is more accurate at frequently cloudy locations ($\overline{k_t} < 0.8$). The long term errors of the two models

varies between 218.3 and 315.5Wm^{-2}. This error is within the range of the two previously proposed NWP based DNI models. [62] found a RMSE between 197 and 370Wm^{-2}. The ANN based approach proposed by [72] achieves long-term RMSEs between 156 and 171Wm^{-2}. A more detailed comparison of the results in Merced is given in section 5.4.2. Since all shown DNI models outperform the persistence model, and cloud cover predictions are available for most locations on the globe, we propose using one of the shown DNI forecasting methods as a benchmark to compare results of different models and calculate forecasting skill (see section 5.4.4).

5.4.2 Monthly performance

Results from Merced are especially valuable since they allow for comparison to the results obtained by [72]. While the ANN study was conducted from November, 2008 - November, 2009, this study covers data for Merced from September, 2012 - May, 2013. However, similar errors in the persistence model allow the assumption that the characteristics of both data sets are comparable. Figure 5.2 shows the monthly rRMSE for all models covered in this study in addition to the ANN based results. The best performing model varies by month. The long term statistics shown in table 5.4 are represented in this graph since Model 2a performs slightly better than Model 2b while both outperform Model 1. Model 1 has the strongest performance variations, showing the highest monthly error in October, but outperforming all other methods in December. The ANN based models using up to 10 input variables from the NWS database performs best during two month (November and March). The ANN model seems to have the lowest long-term error. While the reported errors of the ANN based approach are within 156 and 171Wm^{-2}, the error in this study for Merced varies between 225 and 245Wm^{-2}. The reported results [72] also cover July and August in the long term error. These months have not been included in the Merced data set due to a lack of ground measurements. Since July and August are very clear month in Merced, the reported error for a whole year of data can be assumed to be lower. However, the advantage of the proposed cloud-cover-to-DNI model roots in the simplicity with only

one exogenous input variable and the vast data availability (basically the whole globe).

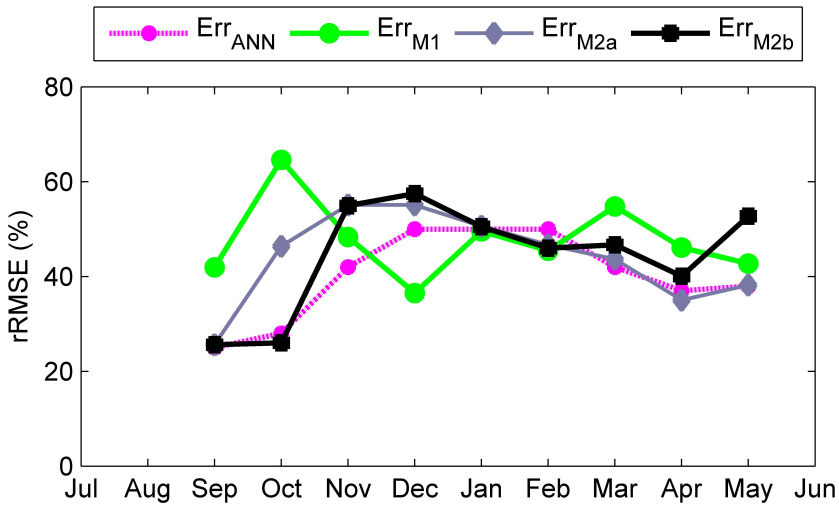

Figure 5.2: Occurring rRMSEs of the proposed day-ahead forecasts per month for the location in Merced from August 2012 until May 2013. Results are compared to the reported rRMSEs of the ANN based DNI model from [72] from November 2011 until November 2012. Note: in [72], the rRMSE is calculated against the yearly DNI average whereas the rRMSE by definitions of equation 3.5 is for the same period (here: monthly DNI average). To make results of the two studies comparable, rRMSE for this figure has been calculated against the yearly DNI average ($\overline{DNI} = 526 Wm^{-2}$). This applies for this figure only.

5.4.3 Clearness and error

Figure 5.3 shows the average MAE of the DNI forecasts as a function of k_b. In general, the cloud-cover-to-DNI model tends to be more accurate with lower cloud cover. This is especially valuable since all concentrated solar energy applications are ideally placed in locations with low cloud cover. At all locations, the GHI-to-DNI model outperforms the cloud-cover-to-DNI model for low k_b (approximately $k_b < 0.4$), however, the cloud-cover-to-DNI model performs better for high k_b ($k_b > 0.4$). Therefore, it can be concluded that a hybridization of both models would mitigate some of the occurring errors.

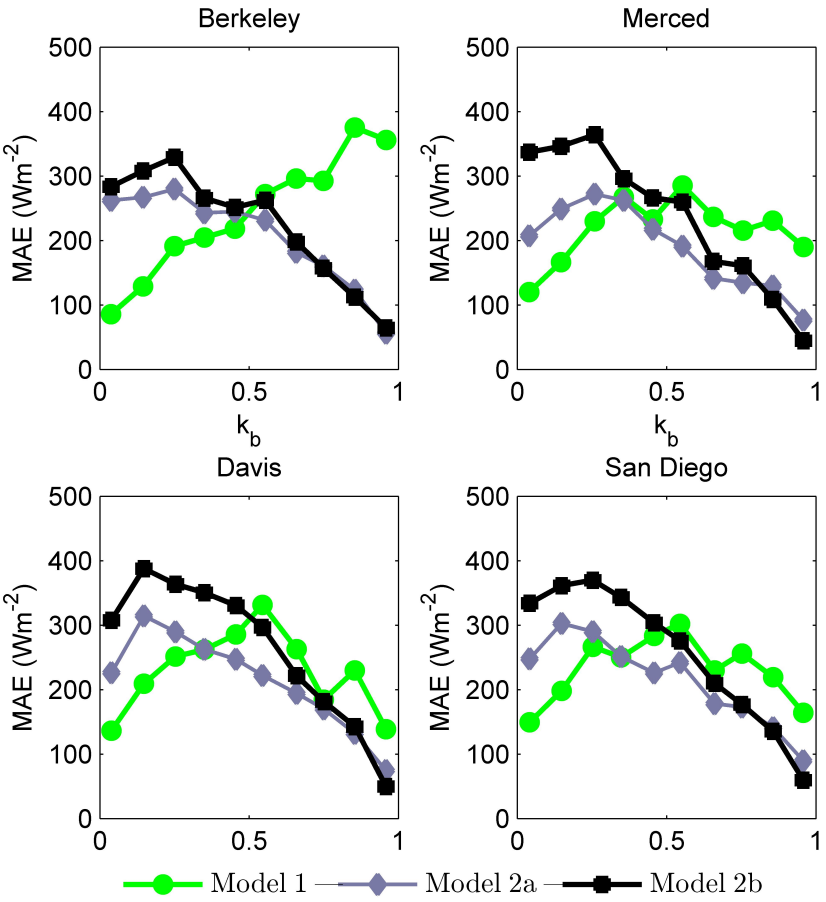

Figure 5.3: Ground truth clearness index (k_b) and average MAE for the forecasts for all four locations. As a general trend, the error decreases with increasing clearness. The MAE from the Model 2a is usually slightly smaller than the error from the Model 2b. This is in agreement with the results from 5.4. Consistently , Model 1 performs best for $k_b < 0.4$, however, the error increases with increasing clearness k_t.

Table 5.4: Part 1: Statistical results for the GHI and DNI predictions for all locations covered in this study. M1 relates to GHI from NAM and DNI modeled with Model 1. M2a are GHI and DNI predictions based on the cloud-cover-to-irradiance model (Model 2) with RDPS predicted cloud data as an input. M2b is as M2a but with cloud cover predictions from the NAM model.

		GHI						**DNI**					
		$\overline{\widehat{GHI}}$	MBE	MAE	RMSE	rRMSE	Skill	$\overline{\widehat{DNI}}$	MBE	MAE	RMSE	rRMSE	Skill
Location		$[Wm^{-2}]$	$[Wm^{-2}]$	$[Wm^{-2}]$	$[Wm^{-2}]$	[%]	[%]	$[Wm^{-2}]$	$[Wm^{-2}]$	$[Wm^{-2}]$	$[Wm^{-2}]$	[%]	[%]
Berkeley	M1:	466.6	-83.7	99.3	134.3	35.1	17.1	312.7	153.7	207.0	313.3	67.2	6.9
$\overline{GHI}$=382.9	M2a:	417.1	-34.2	70.1	122.7	32.0	**24.2**	540.4	-74.0	167.2	255.9	54.9	23.9
$\overline{DNI}$=466.4	M2b:	272.7	110.2	132.9	218.5	57.1	-35.0	541.8	-75.3	166.7	252.1	54.0	**25.1**
$\overline{k_t} = 74.8$	Pers.:	381.9	1.0	89.3	161.9	42.3	-	461.8	4.6	209.9	336.4	72.1	-
Davis	M1:	509.2	-81.6	98.4	124.1	29.0	-4.1	485.9	106.5	171.2	248.8	42.0	12.3
$\overline{GHI}$=427.7	M2a:	429.8	-2.2	49.4	93.0	21.7	**22.0**	549.6	42.8	156.6	218.3	36.9	**23.0**
$\overline{DNI}$=592.4	M2b:	395.2	32.4	68.8	133.3	31.2	-11.8	578.1	14.3	159.9	231.8	39.1	18.3
$\overline{k_t} = 87.5$	Pers,:	425.5	2.2	61.3	119.2	27.9	-	583.6	8.8	170.9	283.7	47.9	-

Table 5.5: Part 2: Statistical results for the GHI and DNI predictions for all locations covered in this study. M1 relates to GHI from NAM and DNI modeled with Model 1. M2a are GHI and DNI predictions based on the cloud-cover-to-irradiance model (Model 2) with RDPS predicted cloud data as an input. M2b is as M2a but with cloud cover predictions from the NAM model.

		GHI						**DNI**					
		$\overline{\widehat{GHI}}$	MBE	MAE	RMSE	rRMSE	Skill	$\overline{\widehat{DNI}}$	MBE	MAE	RMSE	rRMSE	Skill
Location		$[Wm^{-2}]$	$[Wm^{-2}]$	$[Wm^{-2}]$	$[Wm^{-2}]$	[%]	[%]	$[Wm^{-2}]$	$[Wm^{-2}]$	$[Wm^{-2}]$	$[Wm^{-2}]$	[%]	[%]
Merced	M1:	461.3	-72.3	87.9	115.5	29.7	4.0	406.3	92.5	169.9	243.8	48.9	21.1
$\overline{GHI}$=389.0	M2a:	366.3	22.7	59.4	100.0	25.7	**17.0**	480.1	18.7	167.7	225.1	45.1	**27.1**
$\overline{DNI}$=498.7	M2b:	324.2	64.8	85.8	151.5	38.9	-25.8	503.4	-4.7	181.1	244.5	49.0	20.9
$\overline{k_t}$ = 91.2	Pers.:	387.2	1.8	71.1	120.4	30.9	-	493.2	5.5	196.1	308.9	61.9	-
San Diego	M1:	475.9	-87.6	112.0	151.9	39.1	2.4	332.1	103.8	214.7	315.5	72.4	8.4
$\overline{GHI}$=388.3	M2a:	416.2	-27.9	80.9	141.5	36.4	**9.1**	547.2	-111.4	214.3	306.9	70.4	10.9
$\overline{DNI}$=435.8	M2b:	276.0	112.3	141.7	230.7	59.4	-48.2	540.9	-105.0	216.3	300.3	68.9	**12.9**
$\overline{k_t}$ = 77.3	Pers.:	392.3	-4.0	93.2	155.7	40.1	-	442.5	-6.7	230.7	344.6	79.1	-

5.4.4 Proposed benchmark

The possibility to relate achieved results and error characteristics of forecasting studies to a benchmark supports the comparability of different methods. This is especially important for forecasts with highly varying conditions between different locations. The error statistics shown in section 3.3, are commonly used in the solar energy field. However, it is known that the persistence model decreases in accuracy with increasing time horizons. This applies for GHI, but appears to be even more distinct for DNI. The day-ahead persistence assumption for DNI is very unlikely to hold true. Since all shown DNI models outperform the persistence model significantly, and cloud cover predictions are available for most locations on the globe, we propose using DNI forecasting Model 2 as a benchmark to compare results of future DNI prediction models. This leaves us with the suggested benchmark:

$$s = 1 - \frac{RMSE_{NewMethod}}{RMSE_{\widehat{DNI}(\widehat{cc})}}, \tag{5.6}$$

where s relates to the achieved skill, $RMSE_{NewMethod}$ is the achieved long-term RMSE from novel DNI prediction models and $RMSE_{\widehat{DNI}(\widehat{cc})}$ relates to the long-term RMSE of DNI forecasts based on cloud cover predictions from any available NWP model as described in section 5.3.3. Relating future models to this benchmark should support the evaluation and comparability of different DNI prediction models.

5.5 Summary

This chapter discussed recent advances in day-ahead DNI prediction and compared two novel approaches to predict DNI for day-ahead market participation. Both models to predict DNI time series one day in are based on NWP models as input data and are compared to a persistence model as a reference. Model 1 produces DNI forecasts based on predicted GHI. Models 2 produces DNI forecasts based on predicted cloud cover. The DNI prediction based on forecasted GHI was evaluated with NAM data. The cloud-cover-to-DNI model has been evaluated with cloud

cover predictions from two different NWP models (NAM and RDPS). The performance of these methods has been compared to ground truth DNI measurements. It was found that DNI forecasts based on cloud cover continuously outperform the forecast of DNI based on GHI while both provide significant improvements over the persistence model. This chapter showed that using RDPS cloud cover as an input is better suited for locations with lower yearly cloud cover (higher cloud index), whereas the NAM cloud cover output works better for locations with more frequent overcasts conditions. A comparison of the results from different locations shows that the forecasting accuracy for DNI is strongly depended on the solar micro-climate. Furthermore, the tendency to reliably predict clear-sky conditions found by the other authors in work related to GHI also applies for DNI. Both results were expected based on the experience with (multiple) day-ahead forecasts for GHI (e.g. [68]). Additionally, the obtained results are compared with previously suggested methods for (multiple) day-ahead DNI prediction. The ANN based model from [72] slightly outperforms the cloud cover model. However, the cloud cover model is valuable because no training data is required and cloud cover predictions are a standard output variable of many operational NWP models. The forecasts can be further optimized for local irradiance characteristics and hence increase the forecasting value beyond the benchmark level presented in this study.

Note: This chapter contains work, previously published in:

- L. Nonnenmacher, A. Kaur, C. F. M. Coimbra, "Benchmarking and Valuation of Day-Ahead Forecasts for Direct Normal Irradiance", (submitted), *Solar Energy*, Oct. 2014.

Chapter 6

Day-ahead DNI forecast optimization

It was shown in chapter 5, that several ways to predict DNI based on NWP inputs exist. In recent years, concentrated solar power (CSP) technologies, solely relying on direct normal irradiance (DNI), reached market maturity, resulting in the installation of several operational large scale CSP plants. Currently, the globally installed capacity is over 2500 MW with additional 2500 MW under construction and further 1400 MW under development [2]. Many of these projects do not facilitate the capability to store energy but are directly feeding electricity into the power gird. Hence, the power output of CSP plants without storage is non-dispatchable. Dispatchable resources have to be available elsewhere in the energy system to balance the power output fluctuations from CSP. There are many benefits for day-ahead DNI forecasting: Based on current market regulations in most countries, power producers have to schedule power production with the system operator, up to several days in advance (unit commitment). If storage is available, day-ahead DNI predictions can be used to increase revenue by dispatching energy to times of higher electricity prices [63],[40]. In this chapter, we evaluate and optimize the NWP based day-ahead DNI forecast proposed in chapter 6 for many locations in the United States. The optimization is important for day-ahead market participation [102] (e.g. in California, energy bids from renewable sources can be placed in the afternoon for the complete next day). The

basic forecast model uses predicted cloud cover from NWP (provided by the regional deterministic prediction system (RDPS) from the Canadian Meteorological Centre (CMSC)) and the Ineichen clear sky model as inputs. This combination of data and clear sky model was found to perform the best in chapter 5. The issued forecasts are evaluated at 8 locations in North America with ground measurements for over 200,000 hours. Additionally, the forecast has been applied to 15 locations with high and medium yearly DNI averages in the Southwestern United States with available satellite derived DNI data. The Southwestern United States are of special interest for the CSP industry due to its high deployment potential [82].

Furthermore, we propose two strategies to optimize the forecasts: (1) Clear sky model corrections. While clear sky GHI mainly relies on the longitude, latitude and sun elevation angle, the DNI component of solar radiation additionally relies heavily on the transparency of the atmosphere. Two common measures of atmospheric clearness are aerosol optical depth (AOD) and Linke turbidity (LT). For an accurate prediction of DNI, the clearness of the atmosphere has to be measured or estimated. The basic forecast approach relies on a clear sky model based on satellite derived monthly turbidity averages. To show the impact of the clear sky model, we deploy a second clear sky model, based on a clear sky recognition algorithm and assumed persistence of clear sky magnitude. (2) Re-forecasting methods are applied to enhance forecasts by extracting information of structured errors in a training set and applying the found model enhancements to the forecast.

6.1 Data

Publicly available data sets were used where possible. DNI data from the UCSD and ISIS ground observatories discussed in chapter 2 are used to verify the accuracy of the forecasts for all 8 locations shown in figure 2.6. For locations without ground measurements, data from the SUNY satellite model (the model evaluated in chapter 3), is used. For all obtained data sets, night values were removed and time matching was applied. Table 6.1 describes the length of the data set from the observatories from the Center for Energy Research at UCSD and

the locations maintained by ISIS.

Table 6.1: Locations with DNI ground instrumentation for evaluation. The first four locations are installed and maintained by the University of California, San Diego. The other locations are part of the ISIS network, maintained by NOAA.

Location	Lat.	Long.	El.	Days
Data from UCSD:				
BER - Berkeley, CA	37.9	-122.3	97 m	876
DAV - Davis, CA	38.5	-121.7	19 m	821
MER - Merced, CA	37.4	-120.4	64 m	761
SAN- San Diego, CA	32.9	-117.2	101 m	619
Data from ISIS:				
ABQ - Albuquerque, NM	35.0	- 106.6	1617 m	1865
HAN - Hanford, CA	36.3	-119.6	73 m	861
OAK - Oak Ridge, TN	36.0	-84.3	334 m	202
SLC - Salt Lake City, UT	40.8	-112.0	1288 m	3090

6.1.1 Satellite derived data

Due to the lack of ground measurements, satellite derived DNI data from the SUNY model is additionally used for evaluation purposes of the proposed model. Hence, data for 2012 provided from SolarAnywhere® deploying the SUNY v 2.4 model, for the locations in table 6.2 (public data set) is used.

6.1.2 Cloud cover predictions

Cloud cover forecasts ($\widehat{cc}$), representing the spatial cloud coverage of a grid element in percent, were obtained from the Regional Deterministic Prediction System (RDPS). The RDPS is a NWP model developed and deployed by the Canadian Meteorological Center (CMC). These data sets cover predictions for the 12h to 36h ahead time horizons in hourly increments, obtained from the daily NWP model run valid from 0:00 standard time (UTC). This input data delivered best performance in [91]. For the 8 locations with ground measurements, predicted cloud

Table 6.2: Locations with cloud cover data from RDPS and satellite derived DNI data from the SUNY v2.4 model in the Southwestern United States. Figure 6.1 maps locations with yearly average DNI resource.

#	Location	Lat.	Long.	Elevation	Days
Data from SUNY v2.4:					
1	Desert Rock, NV	36.7	-116.0	1160 m	364
2	Barstow,CA	34.8	-117.0	660 m	364
3	Las Vegas, NV	36.1	-115.1	600 m	364
4	Imperial, CA	32.8	-115.6	-18 m	364
5	Saint George, UT	37.1	-113.6	872 m	364
6	Seligman, AZ	35.4	-112.9	1600 m	364
7	Phoenix, AZ	33.4	-112.0	331 m	364
8	Tucson, AZ	32.1	-110.9	730 m	364
9	Green River, UT	38.2	-110.2	1243 m	334
10	Winslow, AZ	35.0	-110.7	1470 m	364
11	Farmington, NM	36.7	-108.1	1644 m	364
12	Las Cruces, NM	32.3	-106.9	1219 m	364
13	Denver, CO	39.7	-104.7	1691 m	364
14	Carlsbad, NM	32.5	-104.5	1000 m	364
15	Amarillo, TX	35.2	-101.8	1100 m	364

cover data was available from January 2005 until October 2014. Additionally, gridded data from the run valid from 0:00 UTC was available for the year 2012 for the Southwestern United States.

6.2 Methods

As in the previous chapters, the forecasts are evaluated against the persistence model from section 5.3.1. Additionally, the day-ahead forecast from chapter 5 is used. To show the impact of the accuracy of the DNI clear sky model, the following variation of Model 2 (from section 5.3.3) is used:

$$\widehat{B}_{d+1} = B_{CS,d+1}(\tau) \cdot \frac{(100 - \widehat{cc})}{100}, \tag{6.1}$$

where $B_{CS}(\tau)$ is the DNI magnitude under clear sky conditions as a function of τ, the measured Linke turbidity value. While the general approach stays the same, we solely use a modified clear sky model with an in-feed of updating τ values.

6.2.1 Clear sky model correction

Previous studies investigated the characteristics and fluctuations of Linke turbidity values at various locations (e.g. [51, 107, 88]). Some previous studies also attempted to forecast Linke tubridity or AOD values [7, 62]. Usually, these forecasts are based on transport models and/or remote sensing. The necessity for near real-time measurements (or forecasts) of atmospheric clearness variables (AOD in particular) when reliable estimates of DNI are required was shown in [88]. We follow this approach by measuring the current values of τ and feeding them into the clear sky model. For Australia, [105] quantified the occurrence of dust storms with high impact on DNI to 5-10 a year. Since the variations of turbidity values in North America are on the order of days rather than shorter time horizons, we propose a method for real-time clear sky detection. The detected clear-sky values are then extrapolated to form an accurate clear sky model for the upcoming days. [51] proposed a method to detect DNI clear sky values in measured DNI time series based on a adjustment of the model proposed by [108] for the recognition of GHI

clear sky values in GHI time series and the findings of [29]. While their method to detect clear sky periods in time series is highly reliable for data with high sampling rates, it is unsuitable for hourly time series since the step changes vary broadly for hourly averages throughout the year. Therefore, a geometry and magnitude based clear sky detection algorithm is proposed as follows:

Based on the clear sky detection algorithm, the corrected clear sky DNI is extrapolated to the following days until a new clear day is identified. The impact of the two different clear sky models are shown in figure 6.4 and 6.5 and are discussed in section 6.3.4.

6.2.2 Re-forecasting

Re-forecast methods take an initial forecast and enhance the prediction accuracy by extracting information from the structure of occurring errors. Re-forecasting is used for many applications, e.g. for load prediction [58]. To enhance the performance of the DNI benchmark forecast, re-forecasting is applied to the locations where sufficient ground data is available. A large set of data and forecasts are important to capture the long term performance of the forecasts and to identify reoccurring error patterns. The data sets are divided into independent training, validation and test sets. The re-forecast is developed with training and validation sets and then applied to the test set to quantify the performance. Our approach for DNI re-forecasting is adapted from the approach in [58] for load forecasting adapted from [65]. The applied generalized re-forecast model (GM) is defined as:

$$\mathcal{A}(q)y(t) = \frac{\mathcal{B}(q)}{\mathcal{F}(q)}(q)u(t-n_k) + \frac{\mathcal{C}(q)}{\mathcal{D}(q)}(q)e(t), \tag{6.2}$$

where $\mathcal{A}(q)$, $\mathcal{B}(q)$, $\mathcal{C}(q)$, $\mathcal{D}(q)$ and $\mathcal{F}(q)$ are the n^{th} order polynomials as listed below, y is the output (here: $F_{Reforecast}$), u is the input (here: F_{Basic}), t is time, n_k the delay parameter, q the shift operator and e white noise. The polynomials used are:

$$q^{\pm N}\psi(t) = \psi(t \pm N), \tag{6.3}$$

$$\mathcal{A}(q) = 1 + a_1 q^{-1} + \ldots + a_{n_a} q^{-n_a}, \tag{6.4}$$

$$\mathcal{B}(q) = b_1 + \ldots + b_{n_b} q^{-n_b+1}, \tag{6.5}$$

$$\mathcal{C}(q) = 1 + c_1 q^{-1} + \ldots + c_{n_c} q^{-n_c}, \tag{6.6}$$

$$\mathcal{D}(q) = 1 + d_1 q^{-1} + \ldots + d_{n_d} q^{-n_d}, \tag{6.7}$$

$$\mathcal{F}(q) = 1 + f_1 q^{-1} + \ldots + f_{n_f} q^{-n_f}. \tag{6.8}$$

Depending on the application of the polynomials, and with the possibility to set them to unity, this generalized model transforms to the an auto-regressive model (ARX) if only $\mathcal{A}(q)$ and $\mathcal{B}(q)$ are used. If $\mathcal{C}(q)$ is used in addition, it represents an auto-regressive moving average model with exogenous input (ARMAX). The utilization of $\mathcal{B}(q)$, $\mathcal{C}(q)$ $\mathcal{D}(q)$ and $\mathcal{F}(q)$ represents a Box-Jenkins model.

Additionally to the above linear models, a non-linear auto-regressive (NARX) model was tested. Since best results are achieved with the generalized and the Box-Jenkins approaches (see 6.3.5), more details on the implementation of NARX model are not mentioned here but can be found in [58].

6.3 Optimization results and discussion

6.3.1 Locations with ground data

To evaluate the forecasts in this chapter, again the validation metrics from section 3.3 are used. The above error metrics have been applied to the persistence and the benchmark model at 8 locations with ground DNI measurements. Results are summarized in table 6.3. Again, the benchmark model clearly outperforms the persistence model at all locations in terms of RMSE, rRMSE, and $xcorr$. The achieved forecasting skills are in the range of 12.4% to 38.2%. The lowest RMSE occurs in Hanford, California, located in the San Joaquin Valley. This location has high yearly DNI averages ($542.1 Wm^{-2}$). The highest skill occurs in Oak Ridge, Tennessee, a location with low yearly DNI averages ($338.9 Wm^{-2}$) and strong variability. In Oak Ridge, the persistence model performs poorly since irradiance conditions vary heavily from day-to-day. However, the NWP based forecast achieves good performance. The results from Hanford, Albuquerque and Salt Lake City are of value since they are based on 2, 4 and over 6 years of ground

data. Long verification data sets are known to reduce random errors [34]. Low random errors are important for the re-forecast methods described applied below.

6.3.2 Locations with satellite data

Table 6.4 displays the results for all locations in figure 6.1. Achieved RMSE for the chosen locations with high and medium CSP potential vary between $170.3 Wm^{-2}$ and $275.4 Wm^{-2}$. The lowest RMSE occurs in Imperial, located in California's Colorado Desert with excellent yearly DNI averages and low variability. The highest skill is achieved in Saint George, UT with 33.9%, a location with relatively low variability and high DNI averages (location #5). In general, the RMSE increases with variability, a location specific parameter (see figure 6.2). The impact of satellite data compared to ground measurements are discussed in the sensitivity analysis below.

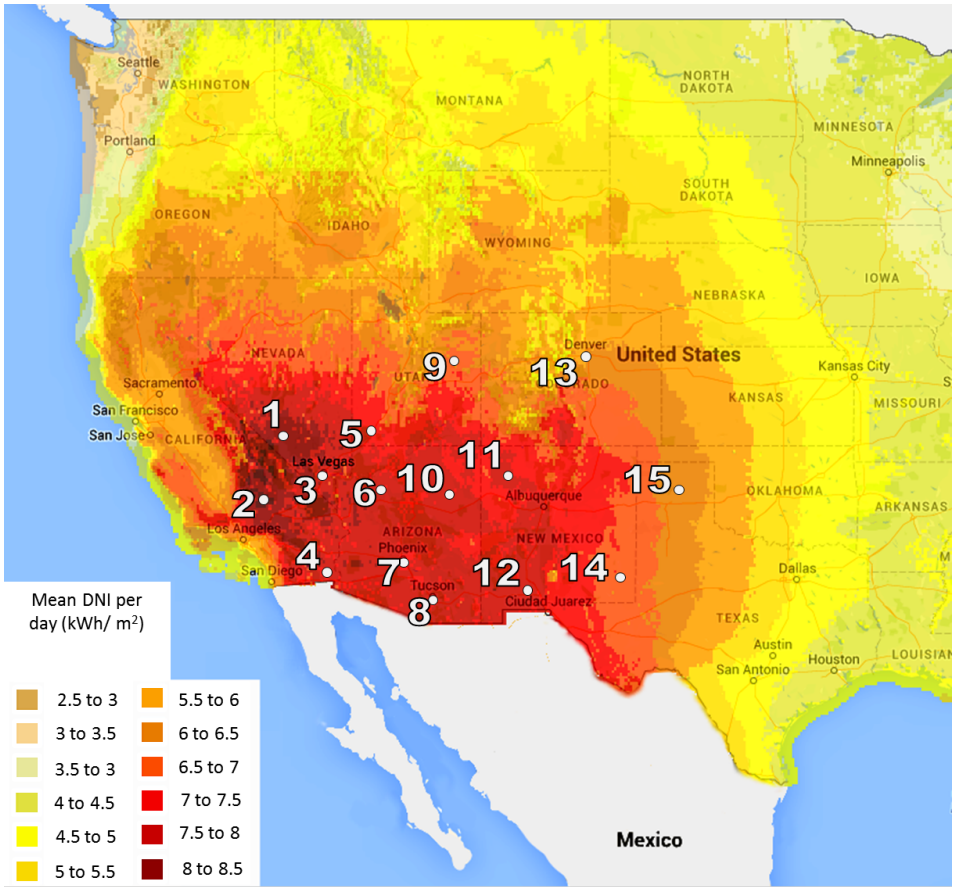

Figure 6.1: Map of sites with satellite data and the yearly DNI average in $kWhm^{-2}$. Data and map modified from http://maps.nrel.gov/prospect. Data obtained from SUNY v2.4 model for all 15 locations.

Table 6.3: Results from persistence (Pers.) and the basic model (F_{Basic}) for all 8 locations with ground data for daylight times (night values are taken off when the sun elevation angle $< 5°$).

Location	Model	$\overline{DNI}_G$	$\overline{DNI}_{Forecast}$	MBE	rMBE	MAE	rMAE	RMSE	rRMSE	*xcorr*	Skill
		Wm^{-2}	Wm^{-2}	Wm^{-2}	[%]	Wm^{-2}	[%]	Wm^{-2}	[%]	(-)	[%]
Berkeley	Pers.	505.5	504.4	1.01	0.2	212.3	42.0	348.5	68.9	0.56	-
	F_{Basic}		590.4	-84.9	-16.8	161.1	31.9	265.1	52.4	0.75	24.0
Davis	Pers.	589.4	588.5	0.86	0.14	173.2	29.4	287.1	48.7	0.59	-
	F_{Basic}		541.8	47.6	8.1	160.2	27.2	230.2	39.1	0.73	19.8
Merced	Pers.	508.7	509.3	-0.6	-0.1	187.1	36.8	302.5	59.5	0.61	-
	F_{Basic}		469.4	39.3	7.7	158.2	32.1	209.4	41.2	**0.80**	30.1
San Diego	Pers.	472.1	472.0	0.1	0.0	236.8	50.2	353.7	74.9	0.53	-
	F_{Basic}		552.1	-80.0	-16.9	220.8	46.8	309.9	65.6	0.60	12.4
Albuquerque	Pers.	638.2	636.7	1.5	0.23	246.9	38.1	372.9	58.4	0.41	-
	F_{Basic}		664.8	-26.7	-4.2	173.4	27.2	262.1	41.1	0.67	29.6
Hanford	Pers.	542.1	544.0	-2.0	-0.3	146.2	27.0	247.1	45.6	0.67	-
	F_{Basic}		549.4	-7.3	-1.4	**133.4**	**24.6**	**200.9**	**37.1**	0.76	18.6
Oak Ridge	Pers.	338.9	346.5	-7.6	-2.2	315.1	93.0	431.4	127.3	0.20	-
	F_{Basic}		419.0	-80.1	-23.6	181.0	53.4	266.7	78.7	0.70	**38.2**
Salt Lake City	Pers.	470.6	470.1	0.4	0.1	267.9	56.9	386.6	82.2	0.40	-
	F_{Basic}		460.4	10.2	2.2	182.8	38.8	254.1	54.0	0.71	34.3

Table 6.4: Part 1: Results from persistence (Pers.) and the basic model (F_{Basic}) for location 1-5 with satellite data for daylight times (night values have been taken off when the sun elevation angle $< 5°$. $\overline{DNI}_{Sat}$ is the average DNI assessed with the satellite model.

# Location	Model	$\overline{DNI}$	$\overline{\lvert V \rvert}$	$\overline{DNI}_F$	MBE		MAE		RMSE		σ	Skill
		Wm^{-2}	Wm^{-2}	Wm^{-2}	Wm^{-2}	[%]	Wm^{-2}	[%]	Wm^{-2}	[%]	Wm^{-2}	[%]
1) Desert Rock	Pers.	664.0	135.6	663.6	0.3	0.1	186.1	28.0	307.0	46.2	307.1	-
	F_{Basic}			622.9	41.1	6.2	154.1	23.2	224.4	33.8	220.7	26.9
2) Barstow	Pers.	678.9	130.2	678.2	0.7	0.1	135.8	19.9	245.7	36.2	245.7	-
	F_{Basic}			648.6	30.3	4.5	113.3	**16.7**	184.1	**27.1**	181.6	25.1
3) Las Vegas	Pers.	622.2	129.4	622.6	-0.4	-0.1	163.5	26.3	277.8	44.6	277.9	-
	F_{Basic}			606.7	15.5	2.5	126.8	20.4	196.1	31.5	195.5	29.4
4) Imperial	Pers.	618.4	125.4	619.3	-0.9	-0.1	133.1	21.5	229.6	37.1	229.6	-
	F_{Basic}			574.9	43.4	7.0	116.7	18.9	**170.3**	27.5	**164.7**	25.8
5) Saint George	Pers.	625.7	128.4	626.7	-1.0	-0.2	197.9	31.6	321.3	51.3	321.3	-
	F_{Basic}			614.8	10.9	1.7	134.1	21.4	212.4	33.9	212.1	**33.9**

Table 6.5: Part 1: Results from persistence (Pers.) and the basic model (F_{Basic}) for location 6-10 with satellite data for daylight times (night values have been taken off when the sun elevation angle $< 5°$. $\overline{DNI}_{Sat}$ is the average DNI assessed with the satellite model.

# Location	Model	$\overline{DNI}$	$\overline{\lvert V \rvert}$	$\overline{DNI}_F$	MBE		MAE		RMSE		σ	Skill
		Wm^{-2}	Wm^{-2}	Wm^{-2}	Wm^{-2}	[%]	Wm^{-2}	[%]	Wm^{-2}	[%]	Wm^{-2}	[%]
6) Seligman	Pers.	624.1	137.2	624.0	-0.1	0.0	208.3	33.4	335.3	53.7	335.3	-
	F_{Basic}			534.6	89.5	14.0	206.7	33.1	261.4	41.9	245.7	22.0
7) Phoenix	Pers.	603.1	128.3	604.7	-1.6	-0.3	146.6	24.3	255.7	42.4	255.7	-
	F_{Basic}			612.8	-9.7	-1.6	**112.0**	18.6	192.1	31.9	191.9	24.9
8) Tucson	Pers.	630.9	132.7	632.2	-1.2	-0.2	175.5	27.8	296.9	47.1	297.0	-
	F_{Basic}			617.5	13.5	2.1	129.0	20.4	209.7	33.2	209.3	29.4
9) Green River	Pers.	585.9	143.5	585.5	0.4	0.1	232.6	39.7	344.1	58.7	344.1	-
	F_{Basic}			495.1	90.8	16	219.7	37.5	273.5	46.7	258.0	20.5
10) Winslow	Pers.	618.1	139.0	620.1	-1.9	-0.3	224.6	36.3	340.9	55.2	341.0	-
	F_{Basic}			562.8	55.4	9.0	190.9	30.9	249.8	40.4	243.6	26.7

Table 6.6: Part 2: Results from persistence (Pers.) and the basic model (F_{Basic}) for all 15 locations with satellite data for daylight times (night values have been taken off when the sun elevation angle $< 5°$. $\overline{DNI}_{Sat}$ is the average DNI assessed with the satellite model.

# Location	Model	$\overline{DNI}$	$\overline{\lvert V \rvert}$	$\overline{DNI}_F$	MBE		MAE		RMSE		σ	Skill
		Wm^{-2}	Wm^{-2}	Wm^{-2}	Wm^{-2}	[%]	Wm^{-2}	[%]	Wm^{-2}	[%]	Wm^{-2}	[%]
11) Farmington	Pers.	615.3	145.5	613.7	1.6	0.3	241.9	39.3	361.2	58.7	361.2	-
	F_{Basic}			577.2	38.1	6.2	191.9	31.2	258.1	41.9	255.3	28.5
12) Las Cruces	Pers.	655.7	137.8	656.5	-0.9	-0.1	177.4	27.1	293.7	44.8	293.8	-
	F_{Basic}			538.0	117.6	18	193.7	29.5	236.3	36.0	204.9	19.6
13) Denver	Pers.	503.4	150.8	502.2	1.2	0.2	259.3	51.5	382.2	75.9	382.3	-
	F_{Basic}			485.6	17.8	3.5	201.1	39.9	275.4	54.7	274.8	28.0
14) Carlsbad	Pers.	568.0	145.5	568.2	-0.2	-0.0	218.3	38.4	345.2	60.8	345.3	-
	F_{Basic}			556.0	12.1	2.1	166.8	29.4	244.6	43.1	244.3	29.2
15) Amarillo	Pers.	529.0	134.3	529.1	-0.1	**0.0**	235.9	44.6	366.4	69.3	366.4	-
	F_{Basic}			519.2	9.8	1.9	175.2	33.1	252.1	47.7	252.0	31.2

6.3.3 Sensitivity analysis

Since all ISIS locations are also NSRDB locations, ground measurements from there are used to calibrate the satellite model. Only the sites in Berkeley, Davis, Merced and San Diego contain two independent sets covering ground measurements and satellite derived data. Hence, the impact of the data origin on forecast evaluation results can be studied. Table 6.7 provides results for the forecast at the four locations, validated with satellite derived data. In comparison to the results generated with ground data in table 6.3, the errors (RMSEs) from satellite validation are between 14.7% and 30.7% smaller. While satellite data is generally suitable to evaluate forecasting models, it seems to underestimates the uncertainty in the DNI resource. A previous validation of the SUNY model at the four UCSD sites found MAEs of 18.7% for Berkeley, 21.7% for Davis 15.3% for Merced, and 24.14% for San Diego [92]. These results are important to highlight the uncertainty introduced by the data source. This finding adds to other publications stressing the uncertainty in satellite DNI models [49]. Additionally, it is an attempt to show the sensitivity of forecast evaluation to input data since otherwise only the combination of input data and model performance can be evaluated as mentioned in [34].

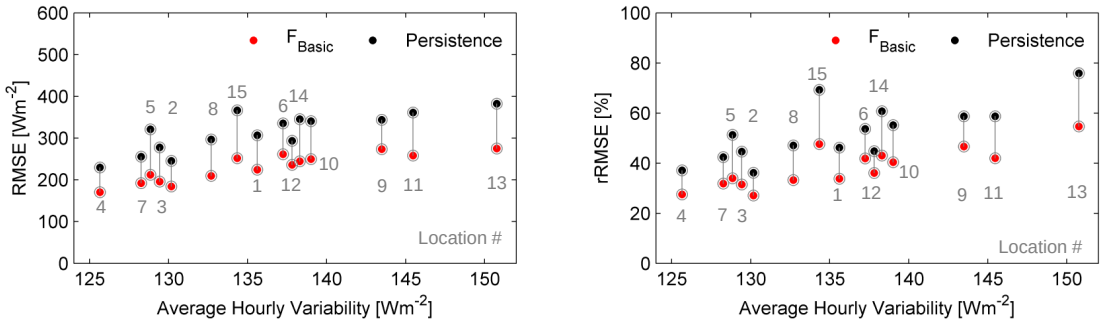

Figure 6.2: RMSE and rRMSE versus variability of the solar resource for locations shown in figure 6.1. F_{Basic} always outperforms persistence while the error in general increases with variability. The rRMSE is relative to the yearly DNI averages.

Table 6.7: Results from persistence (Pers.) and the basic model (F_{Basic}) for the 4 independent locations evaluated with satellite data. All locations show better error characteristics if the performance is assessed with satellite data than when ground data is used (compare to table 6.3).

Location	Model	$\overline{DNI}_{Satellite}$ Wm^{-2}	$\overline{DNI}_{Forecast}$ Wm^{-2}	MBE Wm^{-2}	MBE [%]	MAE Wm^{-2}	MAE [%]	RMSE Wm^{-2}	rRMSE [%]	$xcorr$ (-)	Skill [%]
Berkeley	Pers.	428.9	429.5	-0.6	-0.1	181.1	42.2	291.6	68.0	0.58	-
	F_{Basic}.		509.0	-80.2	-18.7	143.0	33.3	226.4	52.8	0.78	22.4
Davis	Pers.	499.9	500.0	-0.1	-0.0	137.4	27.5	251.3	50.3	0.66	-
	F_{Basic}.		510.4	-10.5	-2.1	88.9	17.8	159.9	32.0	0.86	36.3
Merced	Pers.	490.5	490.8	-0.3	-0.1	130.2	26.5	240.2	49.0	0.69	-
	F_{Basic}.		488.6	2.0	0.4	95.0	19.4	161.8	33.0	0.85	32.3
San Diego	Pers.	541.6	541.4	0.1	0.0	171.8	31.7	295.9	54.6	0.61	-
	F_{Basic}.		534.3	7.2	1.3	147.5	27.22	228.2	42.1	0.75	22.9

6.3.4 Clear sky model impact

The results of utilizing a $B_{CS}(\tau)$ instead of a B_{CS} are discussed in this section. The clear sky model correction frequently enhances the performance of the forecast under clear sky conditions and slightly reduces rMBE and rMAE (see table 6.8). Figure 6.5 shows a scatter plot for Imperial, where the clear sky correction enhanced the results noticeably. The first day in this set is recognized as clear, so an update of the clear sky model follows. This reduces the error of the forecast on the following day. However, the same correction increases the error on the third day when the sky conditions were non-clear and cloud cover was under-predicted. The proposed clear sky correction allows for clearness, higher than estimated via monthly turbidity averages and therefore opens up the error bounds. This effect is visualized in figure 6.4, showing data for Salt Lake City. The larger value range adds to the error when clouds are underestimated leading to larger RMSE for the whole data set. Hence, the improvements through clear sky model correction are limited. Figure 6.3 shows three consecutive days with ground measurements and forecasts from the basic model F_{Basic} and the model with the applied clear sky correction $F_{CS-Correction}$. This leaves us with the conclusion that the error in the DNI forecast is mainly due to the error in cloud cover forecasts ($\widehat{cc}$) rather than in the clear sky model or atmospheric clearness assessment. These results are consistent with [120] for the NWP model from the European Center for Medium Range Weather Forecasting (ECMWF). To significantly enhance the forecast performance, better cloud cover predictions are necessary. The high-resolution rapid refresh (HRRR) model from NOAA might provide just that, however, the model is barely operational (since September 2014) and historical data is unavailable.

6.3.5 Re-forecast results

Results for the best performing re-forecast of the five method variations introduced in section 6.2.2 are shown in table 6.9. In Hanford and Salt Lake City, the generalized model (GM) achieves the best results in terms of RMSE while in

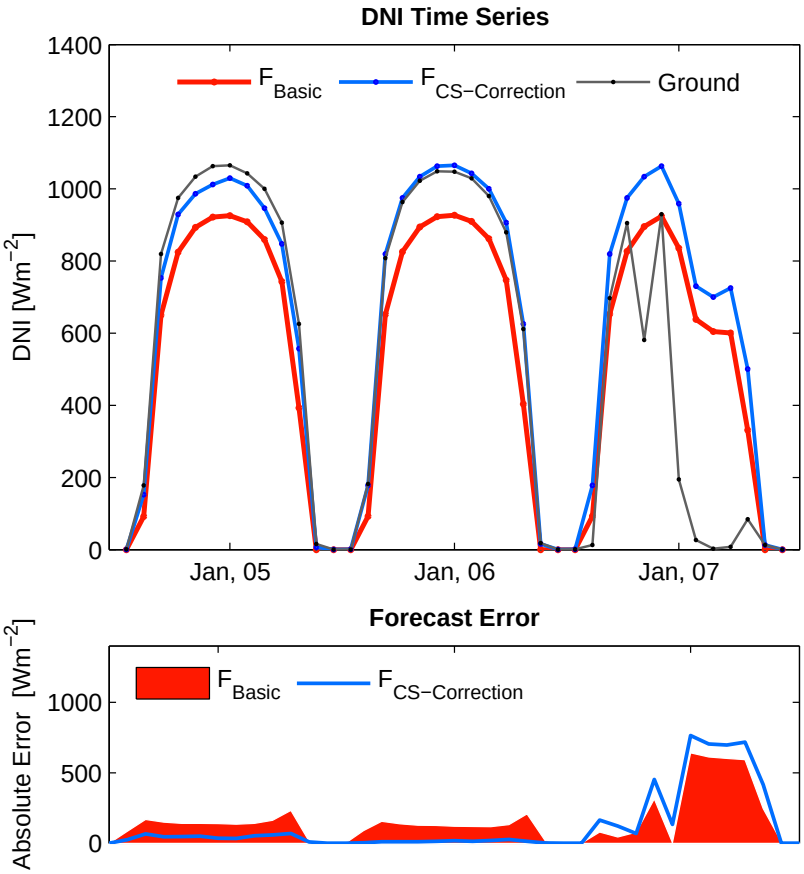

Figure 6.3: Example of three consecutive days of ground measurements in Albuquerque with F_{Basic} and $F_{CS-Correction}$. Clearness detection recognizes Jan, 05 as a clear day and updates the clear sky model. The correction leads to lower error on Jan, 06. While the error is reduced during clear sky periods, the RMSE for long data sets ($F_{CS-Correction}$) increases when cloud cover is under-predicted. Depending on the forecast application, both models are useful.

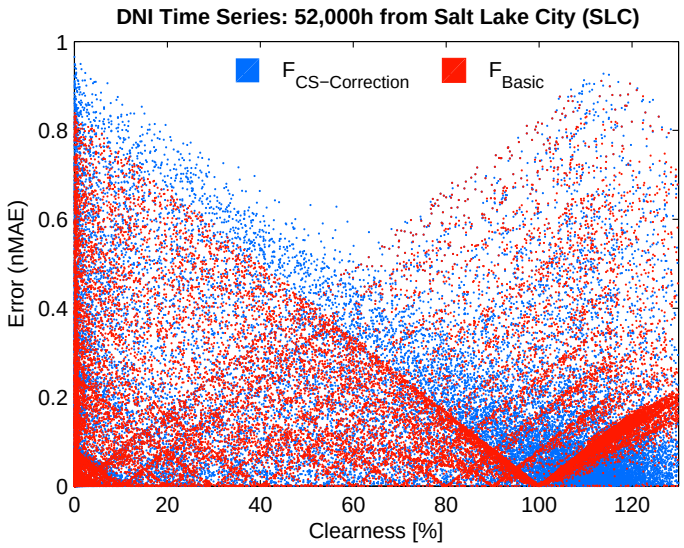

Figure 6.4: Normalized mean absolute error (nMAE) versus clearness for F_{Basic} and $F_{CS-Correction}$ for Salt Lake City. The clear sky model for F_{Basic} is based on monthly turbidity averages while $F_{CS-Correction}$ uses ground data for clearness assessment. $F_{CS-Correction}$ allows for highly clear atmospheres and therefore opens up the error bounds, leading to increasing RMSE but slightly lower MAE and MBEs (see table 6.8).

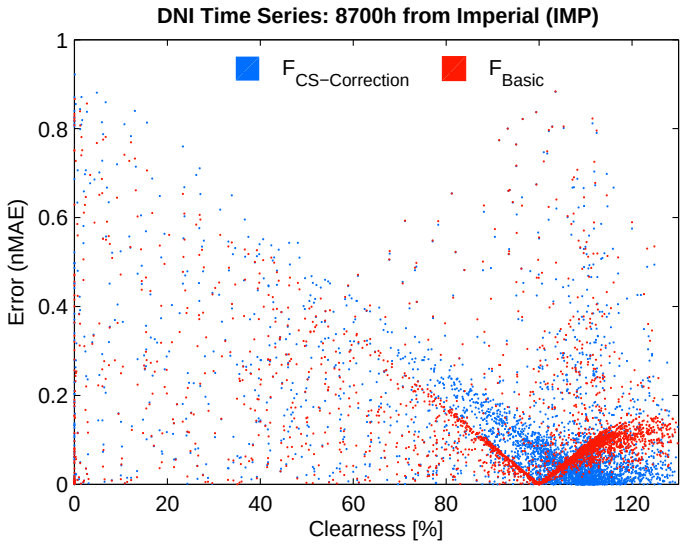

Figure 6.5: Scatter plot for the basic forecast F_{Basic} and the forecast with a corrected clear sky model $F_{CS-Correction}$. The corrected forecast appears to have a lower MBE and MAE but the RMSE increases slightly (see table 6.8).

Table 6.8: Impact of clear sky correction on errors at four sample locations. MBE and MAE are usually reduced with the proposed clear sky correction, but RMSEs increase at all locations. In general, MBE and MAE are easier to correct for than RMSE (e.g. [34]). $\overline{DNI}_G$ is the average DNI measured on the ground.

Method	$\overline{DNI}_G$ Wm^{-2}	rMBE [%]	rMAE [%]	RMSE Wm^{-2}	rRMSE [%]
		Albuquerque (ABQ)			
F_{Basic}	592.2	-5.34	31.6	269.4	45.5
$F_{CS-Correction}$		-4.68	30.2	278.1	47.0
		Imperial (IMP)			
F_{Basic}	618.1	7.1	18.8	170.0	27.5
$F_{CS-Correction}$		-1.6	16.6	173.8	28.1
		Salt Lake City (SLC)			
F_{Basic}	434.6	10.1	41.4	253.5	58.3
$F_{CS-Correction}$		-11.7	39.8	273.0	62.8
		Hanford (HAN)			
F_{Basic}	576.6	7.3	24.6	189.7	32.9
$F_{CS-Correction}$		-6.1	21.3	206.7	35.8

Albuquerque, the Box-Jenkins model performs best. The strongest performance gain was achieved in Hanford, where re-forecasting lowers the RMSE about 13.9% as compared to the basic model. In Salt Lake City, improvements are 4.1% and in Albuquerque 4.5% in terms of RMSE.

Figure 6.6 provides a scatter plot of the normalized errors from the basic forecast F_{Basic}, the forecast with clear sky correction $F_{CS-Correction}$ and the re-forecast $F_{Reforecast}$ with the according mean error and the standard deviation for 13 clearness intervals (10% each). The overall performance gain through re-forecasting as well as the loss in performance through the clear sky model impact can be seen in both, the magnitude of the mean errors as well as the standard deviations. As the other two forecasts, the re-forecast has the lowest mean errors and standard deviations for high clearness.

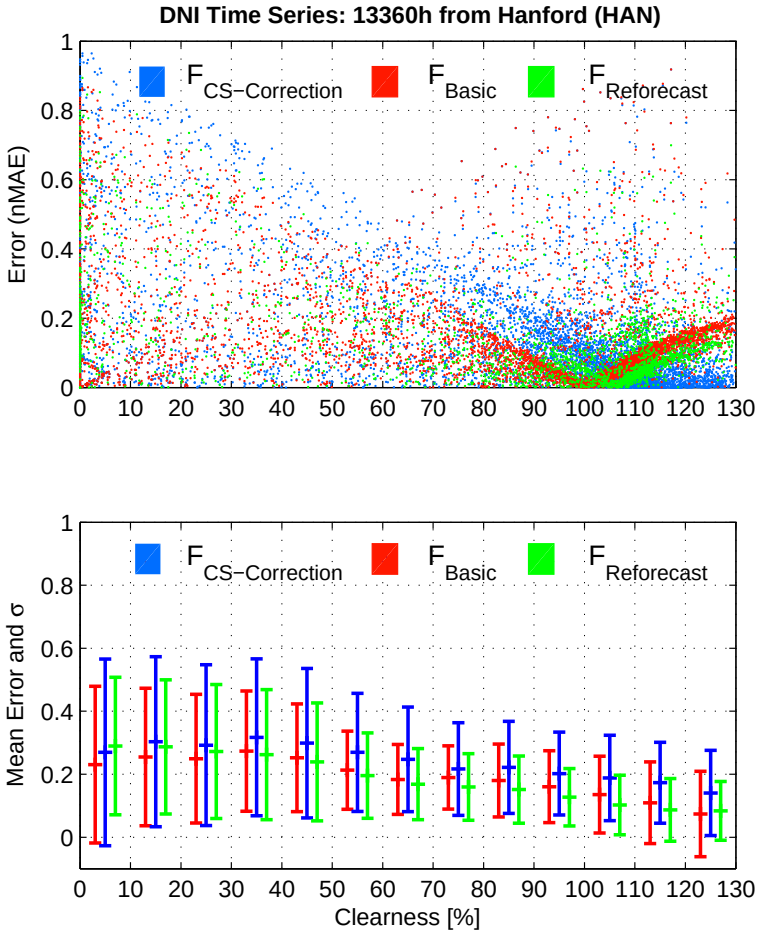

Figure 6.6: Scatter plot of error versus clearness for Hanford for the forecasts F_{Basic}, the forecast with clearness correction $F_{CS-Clearness}$ and the re-forecast ($F_{Reforecast}$) including the mean error with the standard deviation for clearness intervals of 10%. Re-forecasting reduces the mean errors as well as the standard deviation (error bars) for all clearness bins. Lowest errors occur for highest DNI values (under clearest atmosphere).

Table 6.9: Results obtained with the basic forecast and the applied re-forecasting methods. Re-forecasting reduces RMSE, hence enhances the performance at all locations, creating a skill over the benchmark forecast in the range of $4.1\% - 13.9\%$. The best performing re-forcast method was Box-Jenkins for Albuquerque, and the generalized model (GM) for Hanford and Salt Lake City. $\overline{DNI}_G$ is the average DNI measured on the ground.

Method	$\overline{DNI}_G$ Wm^{-2}	rMBE [%]	rMAE [%]	RMSE Wm^{-2}	rRMSE [%]
		Albuquerque (ABQ)			
F_{Basic}	594.8	-6.42	31.3	267.7	45.0
$F_{Reforecast}$		-6.31	30.9	255.6	43.0
		Hanford (HAN)			
F_{Basic}	587.5	10.7	25.7	204.9	34.9
$F_{Reforecast}$		4.7	21.4	176.4	30.0
		Salt Lake City (SLC)			
F_{Basic}	435.1	1.02	41.9	254.7	58.5
$F_{Reforecast}$		-2.8	41.8	244.1	56.1

Figure 6.7 shows the bias and standard deviation as error bars for the forecasts versus the hour of the day for the basic model and the re-forecast model for the location in Hanford. The results from re-forecasts are better, but errors remain rather large. While re-forecasting methods in general reduce biases and structured errors, unstructured errors remain unchanged. These results are a further indicator that forecasting errors are mainly due to errors in cloud cover predictions. The forecast age and therefore, the forecast error, is larger in the afternoon. This suggest that CSP capacity scheduling would benefit from market regulation that allow for updated capacity forecasts during the day.

6.4 Summary

This chapter leaves us with the following conclusions: (1) Validation at 8 inherently different solar micro-climates with ground measurements proves that the NWP based day-ahead benchmark DNI forecast always outperforms the persistence model, with a gain in skill between 12.4% and 38.2%. Additionally, applied

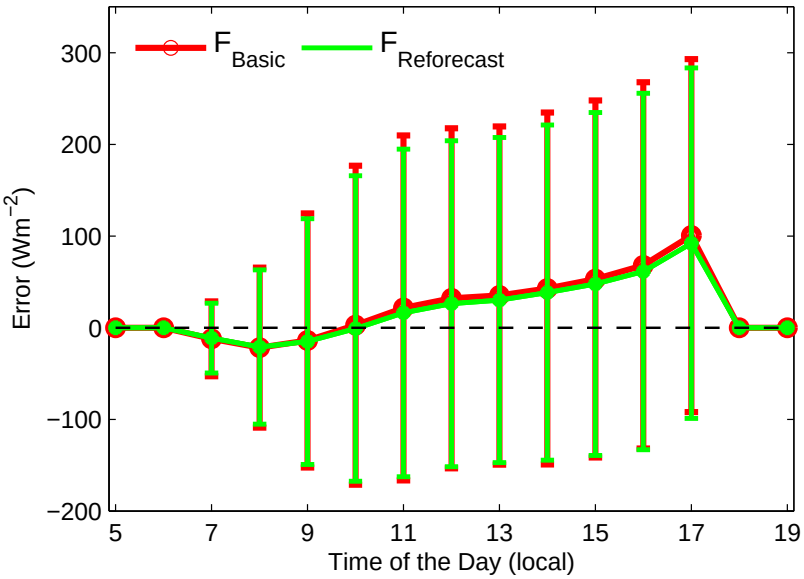

Figure 6.7: Long term performance for daily DNI predictions in terms of mean bias error and standard deviation versus the time of day. Errors are low for morning hours (also partially due to low DNI averages) and increases for later times with especially decreasing performance in the afternoon. It is likely that this is caused by the loss of accuracy of cloud cover predictions with increasing forecast age.

re-forecasting methods can further enhance this skill 4.1% to 13.9%. As for most other forecasts, the error increases with forecast age. (2) Evaluation of the basic forecast with satellite DNI data in 15 areas with high and medium CSP potential showed the general applicability to reduce uncertainty in the DNI resource. The forecasts achieve lowest errors at locations with low variability. The highest forecasting skill occurs at locations with high variability (because the persistence model performs low). (3) A sensitivity analysis indicates that forecast accuracy is overestimated when satellite data is used for evaluation (up to 71.3Wm^{-2} RMSE). (4) The comparison of two different, but highly accurate DNI clear sky models showed that the forecast error is mainly due to erroneous cloud cover predictions. The errors caused by variations in atmospheric turbidity are small. One clear sky model tends to reduces biases while the other one enhances the overall performance (in terms of RMSEs). (5) As a general result, it could be shown that NWP based DNI day-ahead forecasts can reduce the uncertainty in the solar resource at all

locations in North America with potential CSP deployment. Many implications of this for the integration of CSP are discussed in the following chapter.

Note: This chapter contains work, previously published in:

- L. Nonnenmacher, A. Kaur, C. F. M. Coimbra, "Day-Ahead Resource Forecasting for Concentrated Solar Power Integration", (submitted), *Renewable Energy*, Apr. 2015.

Chapter 7

Implications for CSP integration

The need for accurate DNI prediction is well known. Accurate DNI forecasts on short (< 5 h) and long (> 10 years) term scale help manage and assess future CSP establishments [105]. Using accurate 2-day ahead DNI forecasts can increase revenue and decrease penalty costs for CSP and includes a review of previous work on DNI forecasts [63]. Additionally, [11], [120], and [91] relate to the topic. Here, the standard deviation from equation 3.7 becomes important since it is the main variable to estimate the necessary required reserve allocation as discussed below.

7.1 Simplistic CSP power output model

DNI prediction is only dependent on atmospheric variables, whereas power output prediction is additionally a function of many CSP system characteristics. [84] has shown that the conversion rate between solar thermal power and DNI is linear with the slope depending on the solar multiple (normalized ratio of the solar field size in terms of the power block size). The exact DNI-to-power conversion is subject to many CSP system parameters, locations and several technology choices. It is known that the cost of uncertainty for CSP plants can be reduced significantly with energy storage (e.g. thermal energy storage [20]), however, direct steam systems do not have these capabilities. Hence, they heavily rely on the accuracy of forecasting to mitigate the impact of uncertainty for the grid integration. As in [71], we can use a simplified generic model to transfer irradiance to power output.

We assume a linear relation between DNI and generated electricity based on the peak generation capacity (MW_p) as a simplification. The following DNI-to-power output model is used to calculate hourly time series for a hypothetical $100 MW_p$ direct steam CSP plant:

$$E_{el,h} = \begin{cases} 0 & if\ DNI \leq 300, \\ \frac{DNI_m}{700} \cdot MW_p \cdot 1h & if\ 300 < DNI \leq 700, \\ MW_p \cdot 1h & if\ DNI > 700. \end{cases} \tag{7.1}$$

Where $E_{el,h}$ is the electric power output. This model assumes a threshold of $DNI > 300 Wm^2$ to start power production. Between $300 < DNI \leq 700 Wm^2$, this model inherits a linear translation between DNI, thermal power and power output. If the threshold of $DNI > 700 Wm^2$ is passed, the plant generates at peak capacity. This leaves us with the time series of solar power output of the hypothetical $100 MW_p$ power plant. Table 6 summarizes the results of this model for the available days. All other results in this section are extrapolated to represent a full year.

7.2 Value of DNI forecasts for CSP

The costs of integration of intermittent solar energy sources into the electricity system and market sums up from two parts: the costs of solar power variability and the costs from solar power uncertainty. While the costs of solar power variability are determined with the citing decisions, the costs of uncertainty can be mitigated by accurately forecasting power output. Depending on the power purchase agreement (PPA), the rates and conditions under which solar energy is sold into the power grid vary strongly. [71] has shown that it is possible to benefit in terms of revenue from submitting biased forecasts for photovoltaic energy systems under certain conditions. It was shown that revenue benefits can be impeded if a penalty charge applies. [71] directly quantified the economic benefits for GHI forecasts in California, considering energy prices in California for 63 sites. [61] investigated the reduction in yearly penalty charges for a 50 MW_{el} parabolic trough plant in Spain considering the local energy prices and penalty regulations

based on a commercially available DNI forecast. Following the suggestion from [63] to research the benefits of DNI forecasts under different regulations, this section investigates the benefits of the mentioned day-ahead forecasting method for a hypothetical 100 MW_p direct steam solar power plant under three market participation scenarios at two locations in California (Merced and Davis). The first scenario covers a feed-in tariff with fixed rates at which energy is sold to the grid and deviations from scheduled energy output to real energy delivery is penalized with a fixed charge per MWh. To encourage an accurate scheduling of power output in the DAM, penalty charges apply per MWh of power output deviation. This settling scenario is currently common for the integration of intermittent sources in North America and for many locations in Europe. Scenario 2 builds on the initial analysis from [71] and applies the same market regulations to a hypothetical 100 MW_p CSP plant scheduling power output based on the proposed DNI forecasts. Under this scenario, energy is sold in the DAM and deviations from the scheduled energy output are settled in the RTM. The third scenario investigates the impact of penalty charges per MWh based on the DAM and RTM price discrepancies to promote that the most accurate power scheduling generates the highest revenue. This settling scenario is important based on the assumption that the share of intermittent sources in the utility grid will significantly increase in the next decade(s) prospectively posing bigger operational challenges if power scheduling is inaccurate.

Table 7.1: Results from the DNI-to-power output model. The capacity factors for Merced and Davis are within the range of typical CSP plants.

	Davis	Merced
Valid Days	290	173
Simulated PO (MWh)	238,642	109,276
Capacity Factor [%]	34.3	26.5

7.2.1 Settling scenario 1

The first settling scenario assumes a fixed contracted price at which energy is sold and a fixed penalty charge that applies per MWh deviation from the scheduled energy sales. This scenario is currently common for feed-in tariffs and power purchase agreements between solar power producers and utilities. To assess the revenue generated by selling the produced solar energy into the grid, we first assess the maximum revenue that could be generated with a perfect forecast. This maximum possible revenue for settling scenario 1 (Sc1) can be calculated by:

$$R_{max,Sc1} = \sum_{h=1}^{8760} E_{G,h} \cdot P_{PPA}. \tag{7.2}$$

Here, $E_{G,h}$ represents the energy delivered to the grid and P_{PPA} stands for the purchasing price as defined in the power purchase agreement. The revenue of the solar plant is the revenue from energy sales at P_{PPA} (based on the forecast) minus the penalty charges to settle energy delivery deviations. As an equation for this scenario, we can therefore write:

$$R_{Sc1} = \sum_{h=1}^{8760} \Big((E_{G,h} \cdot P_{PPA}) - PF \cdot P_{PPA} \cdot |E_{F,mod,h} - E_{G,h}| \Big), \tag{7.3}$$

where R_{Sc1} stands for the revenue generated given the different forecasting methods under settling scenario 1, E_F represents the forecasted energy output. $E_{F,mod}$ is the modified forecasted energy output under the assumption that excessive energy would not be sold when DNI is under-forecasted (to avoid penalty charges). Currently the prices for CSP in PPAs is typically around $\$100 - 150$ per MWh in the US. The PF is the deviation penalty factor. The values of PF are mostly in the range of 125% and 175% . For this study, we assume $PF = 1.5$ and $P_{PPA} = \$125/MWh$. The subscript h represents the hour of the year. The expression $PF \cdot P_{PPA,h} \cdot |E_{F,mod,h} - E_{G,h}|$ is the penalty under this settling scenario. If the data sets do not cover a full year, results are extrapolated to represent 365 days. The revenue ratio percentage is calculated as R/R_{Max}. This settling scenario rewards a pessimistic bid into the day-ahead market since penalty charges can be avoided when excessive energy is curtailed. Table 7.2 shows that under

this settling scenario, the revenue of the hypothetical solar power plant varies with the forecast used. The most accurate forecast (Model 2) achieves the highest revenue ratio at both studied locations. It might be counter-intuitive that the second highest revenue in both cases is generated with the persistence DNI model, which performs the lowest in terms of the long term error metrics (see table 5). This is due to the fact that this scenario punishes over-forecasts with a penalty while under-forecasts lead to a loss in revenue due to energy curtailment. Under this scenario, the proposed benchmark forecast has a revenue gain of 19% and 22% over the lowest performing forecast in Davis and Merced, respectively.

Table 7.2: Results from a settling scenario with fixed energy selling price and fixed deviation penalty charges (Scenario 1) from the location in Davis. While the best performing forecast (Model 2) leads to the highest revenue of energy sales, the second best forecast (Model 1) performs the lowest in terms of revenue. This shows that submitting a biased forecast under this settling scenario can be beneficial in terms of revenue and promotes to place conservative day-ahead market bids.

Scenario 1 **(Davis)**	Model 1	Model 2	Persistence
$R_{max,Sc1}$ with curtailment [$]	$34,344,758$ (based on simulated PO)		
R_{Sc1}[$]	$24,221,314$	$28,842,320$	$26,913,821$
Penalty charge [$]	$10,123,443$	$5,502,437$	$7,430,936$
[%] of R_{max}	70.5	83.9	78.4
Scenario 1 **(Merced)**	Model 1	Model 2	Persistence
$R_{max,Sc1}$ with curtailment [$]	$26,265,696$ (based on simulated PO)		
R_{Sc1}[$]	$17,824,576$	$21,724,108$	$18,172,282$
Penalty charge [$]	$8,441,119$	$4,541,587$	$7,765,792$
[%] of R_{max}	67.8	82.7	70.4

7.2.2 Settling scenario 2

Settling scenario 2 is characterized by selling the forecasted power output in the DAM and settling power output deviations under RTM conditions. This scenario is currently used for many wind power producers and was subject of a study

by [71] to investigate the value of GHI forecasting in California. As in [71], this energy trading procedure assumes the discontinuation of the participating intermittent resource program (PIRP) in California and assumes CSP to participate in the wholesale energy market like conventional sources. One of the finding includes that settling rules without the penalization of power output deviations enables a revenue increase by submitting a biased forecast. Under this scenario, we investigate energy deviation settling without penalty charges for energy deviations scheduled in the DAM market (scenario 3 covers the implementation of inaccuracy penalties under these market conditions). The following equation is used to calculate the revenue for energy sales including the settling costs:

$$R_{Sc2} = \sum_{h=1}^{8760} E_{F,h} \cdot (LMP_{DAM,h} - LMP_{RTM,h}) + E_{G,h} \cdot LMP_{RTM,h}. \tag{7.4}$$

where R_{Sc2} represents the revenue generated under scenario 2, $LMP_{DAM,h}$ represents the locational marginal price in the DAM at hour h while $LMP_{RTM,h}$ is the locational marginal price in the RTM. As shown in the original study [71], the following four cases are possible under these market participation rules: Case 1 occurs when the RTM is higher than the DAM price and the forecasting bias is positive (over-forecast). In this case, the energy deficit has to be settled at the higher RTM price and therefore generates a loss in revenue. Case 2 is as case 1 but with a negative forecasting bias (under-forecast). In this case, without a deviation penalty charge, sales at the higher RTM price would generate additional revenue and encourages the submission of a biased forecast. As in [71], this is only a potential revenue gain since it is not guaranteed that the excessive energy from the under forecast can be fed into the grid. Therefore, under these market conditions, the RTM price is set to zero. Case 3 represents instances when the DAM price is higher than the RTM and an over-forecast of power output occurs. This leads to a gain in revenue, since excessive energy could have been sold at the higher DAM market. Case 4 is as case 3 but applies for a negative forecasting bias. When no penalty charge applies, non-delivered energy can be bought at the lower RTM price and therefore leads to a gain in revenue since the bid was placed on the higher DAM price. In the investigated data sets, it never occurred that

the RTM matches the DAM price exactly. Table 7.3 summarizes the results for this scenario. Model 2, as the best performing DNI forecasting model, generates the highest revenue under these market conditions at both locations. However, in Davis, persistence generates higher revenue than Model 1. This is again due to the fact that under certain conditions a biased power production forecasts is beneficial (Case 4 mentioned above). Hence, not only the error statistics of a forecast but the time of occurrence of the error defines the value of information in terms of revenue for the solar plant operator. This result is consistent with the results from [71] for photovoltaic plants biding into the DAM with a day-ahead GHI forecast.

Table 7.3: Results from a settling scenario where energy is sold in the DAM and settled under the RTM price without a deviation penalty charge (Scenario 2) for the location in Davis and Merced. While the best performing forecast (Model 1) leads to the highest revenue of energy sales, the second best forecast (Model 2) performs the lowest in terms of revenue. The DNI forecast model that performs the lowest (Persistence) creates almost the same revenue as the best performing model. This shows that submitting a biased forecast under this settling scenario can be beneficial in terms of revenue and promotes to place biased day-ahead market bids.

Scenario 2 **(Davis)**	Model 1	Model 2	Persistence
$R_{max,Sc2}$[\$]	$13,022,970$		
R_{Sc2}[\$]	$12,033,780$	$12,656,270$	$12,448,200$
[%] of R_{max}	92.4	97.2	95.6
Scenario 2 **(Merced)**	Model 1	Model 2	Persistence
$R_{max,Sc2}$[\$]	$9,323,123$		
R_{Sc2}[\$]	$8,821,909$	$9,142,963$	$8,354,923$
[%] of R_{max}	94.6	98.1	89.6

7.2.3 Settling scenario 3

As suggested by [71] the implementation of a deviation penalty factor can ensure that the highest quality (most accurate) forecast leads to the highest revenue of the solar energy plant and therefore is the most valuable. In the original study, solar energy revenue with a penalty charge was calculated as:

$$R_{Sc2,P} = \sum_{h=1}^{8760} E_{F,h} \cdot (LMP_{DAM,h} - LMP_{RTM,h}) + E_{G,h} \cdot LMP_{RTM,h} - P_{dev,h}, \tag{7.5}$$

$P_{dev,h}$ is the deviation penalty charge as assessed by:

$$P_{dev,h} = PF \cdot max(LMP_{DAM,h} - LMP_{RTM,h}) \cdot |E_{G,h} - E_{F,h}|, \tag{7.6}$$

where PF represents the deviation penalty factor. In the original study, $PF = 150\%$. However, this approach is strongly dependent on the maximum value of $(LMP_{DAM,h} - LMP_{RTM,h})$. Therefore, outliers in DAM and RTM price discrepancies can heavily impact the revenue of a solar energy generator. In the analyzed data set for Davis, $max(LMP_{DAM,h} - LMP_{RTM,h}) = 173.5[\$]$. With the suggested $PF = 150\%$, the occurring penalty charges lead to a negative revenue in any case. To circumvent this, we investigate the penalty deviation charge per MWh required to promote that the most accurate forecast is the most valuable in terms of revenue under real market conditions. Additionally, this modification leads to a more robust penalty charge regulation against outliers in price variations between the DAM and RTM. Hence, we modify equation 7.6 to:

$$P_{dev,h} = PF \cdot \overline{(LMP_{DAM,h} - LMP_{RTM,h})} \cdot |E_{G,h} - E_{F,h}|, \tag{7.7}$$

together with equation 7.4, the revenue becomes a function of the PF. Additionally, as suggested by [71] the restrictions to sell for RTM prices under case 2 are lifted. Since the average of $\overline{(LMP_{DAM,h} - LMP_{RTM,h})}$ is \$15.8 for Davis and \$13.1 for Merced during the considered hours. Figure 7.1 shows the forecasting revenue ratio for $PF = 1$ (no Penalty) to $PF = 7$ for Merced (700% of the DAM to RTM price discrepancy). Note: These PFs are significantly higher than in scenario 1, however, they are on a significantly lower base price. It becomes clear that the most accurate DNI forecast (Model 2) has the highest revenue ratio closely followed by Model 1. As expected, the revenue ratio is a linear function of the penalty charge but the slope varies with forecasting accuracy. For a $PF > 6.1$ the revenue generated with the persistence model would be zero while the most

accurate model still generates 58% of the maximum possible revenue. Under this settling scenario, the most accurate forecast is rewarded. For Davis, Model 2 always generates the highest revenue, while the lift of the sales restriction under case 2 enables the persistence model to generate higher revenue than Model 1 for a lower PF. For a $PF \leq 4.5$, the revenue ratio rewards the accuracy of the DNI forecast. Therefore, the appropriate penalty factor to reward the most accurate forecast with the highest value of information depends on the location specific performance of the forecast and the persistence characteristics of irradiance. Table 7.4 shows the results under this settling scenario for a $PF = 4.5$.

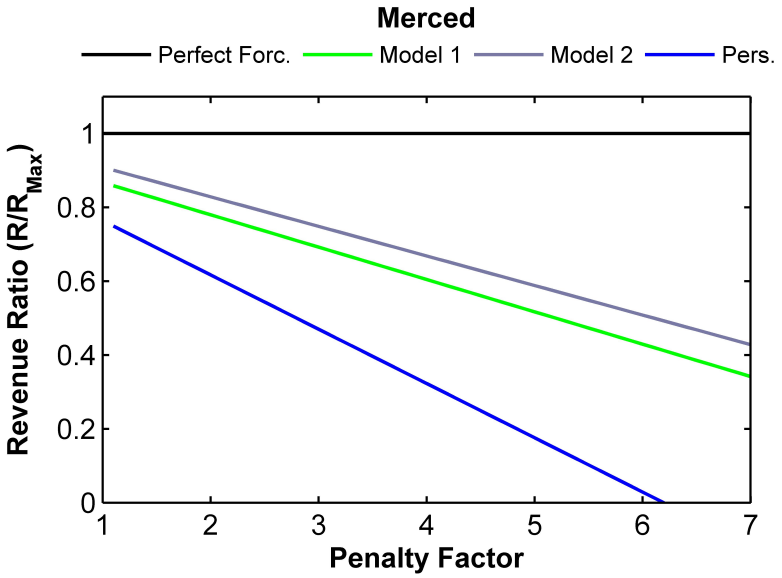

Figure 7.1: Penalty ratio versus penalty factor for the location in Merced as calculated for settling scenario 3. The most accurate forecast generates the highest forecasting revenue. The slope of the line depends on the forecasting accuracy. High forecasting accuracy is more robust against power deviation penalty charges. Therefore, the value DNI forecasting can be expected to increase under high penetration and penalization scenarios.

7.3 Required reserve allocation

Day-ahead DNI forecasts are an operational necessity for capacity scheduling and dynamic reserve allocation. The impact of forecasting on capacity bids

Table 7.4: Results from a settling scenario where energy is sold in the DAM and settled under the RTM price with the implementation of a deviation penalty charge (Scenario 2). The penalty factor ($PF = 4.5$) is high enough to punish inaccurate market bids to prevent strategic market bids. With this penalty factor, the best performing forecast (Model 2) leads to the highest revenue ratio, followed by the second best forecast (Model 2) with persistence performing the lowest. This shows that a carefully investigated penalty factor is capable of establishing market participation regulations rewarding forecasting accuracy.

Scenario 3 **(Davis)**	Model 1	Model 2	Persistence
$R_{max,Sc3}$[$]	$13,022,970$		
R_{Sc3} (with PF=4.5) [$]	$7,706,616$	$8,823,252$	$7,616,643$
[%] of R_{max}	59.2	$67,7$	58.5
Scenario 3 **(Merced)**	Model 1	Model 2	Persistence
$R_{max,Sc3}$[$]	$9,323,123$		
R_{Sc3} (with PF=4.5) [$]	$5,145,756$	$5,747,630$	$2,186,343$
[%] of R_{max}	55.2	61.6	23.5

is discussed in our previous work ([90]). Here, we investigate the impact of uncertainty reduction through forecasting on reserve allocation necessary for CSP plants. We follow the approach suggested by [45] called the $n - sigma$ method to determine operating reserves. It was originally introduced to study the impact of wind variability on dynamic reserves. To cover variability in the DNI resource the required reserves are:

$$\Delta Res = n\Big(\sigma(err)\Big), \tag{7.8}$$

$\sigma(err)$is the standard deviation of the error in DNI (see equation 3.7), n is typically set to 3 (99% confidence interval). To make results comparable, all locations are normalized by the location specific mean DNI. This leaves us with the relative reserve requirements as:

$$rRes = \frac{\Delta Res}{\overline{B_G}}. \tag{7.9}$$

The relative reserve requirements are used to compare the benefits of DNI forecasting to reduce CSP uncertainty, discussed in section 7.3.

7.3.1 CSP with thermal energy storage (TES)

Many previous studies covered the benefits of concentrated solar power with thermal energy (TES) (e.g. [104], [18], [20]). If storage is available, day-ahead DNI forecasts enable the optimization of energy dispatch, since it provides a decision aid to the plant operator when to charge and discharge the TES. The capabilities of dispatch optimization for a photovoltaic-battery storage system have been shown [40]. DNI forecasts enable a similar technological approach, but for CSP with TES. [11] studied costs of balancing a parabolic trough concentrated solar power plant in the Spanish electricity spot markets with and without storage. Their findings include that balancing on day-ahead markets is more cost effective than balancing against intra-day prices. Their forecast was based on the persistence model. They state that further work should improve solar forecasts and show further optimization strategies. Our validation of NWP based day-ahead forecasting (F_{Basic}) outperformed the persistence model at all locations and re-forecasting has proven beneficial to further enhance accuracy. Hence, the balancing costs calculated by [11] could be reduced.

7.3.2 CSP without storage

Many operational and planned CSP plants do not facilitate energy storage mostly due to high costs (e.g. [19] has shown that TES is mostly valuable under high renewable penetration scenarios). CSP plants without storage are feeding electricity directly into the power system, where generation (and demand) fluctuations have to be balanced to maintain grid stability. The impact of locational characteristics and forecast performance on reserve allocation based on the $n - sigma$ method (see section 7.3) is discussed here. Figure 7.2 shows the impact on reserve requirements for location and forecast approach. Again, F_{Basic} outperforms persistence as expected. The worst integration characteristics of the studied locations occur in Denver (location #13) where the required reserve allocation reaches 75.9% of the DNI average. F_{Basic} reduces this reserve requirement to 54.6%. The required reserves, utilizing F_{Basic}, at this locations are higher than at many other locations without forecasting (e.g. Phoenix, location #7). Hence, the location in

Denver has unfavorable integration characteristics, despite being a location with general suitability of CSP deployment ($DNI > 6.0\frac{kWh}{m^2 \cdot day}$). The location in Imperial (location #4) causes the lowest relative reserve requirements (36.2% without forecasting). This can be reduced to 26.7% with F_{Basic}. At all locations, F_{Basic} lowers the required relative reserve, with an average reduction of 28.6% from the initial percentage value. In summary, this implies that site specific DNI variability is an important independent siting parameter along with high yearly averages and grid infrastructure. F_{Basic} can significantly reduce required relative reserves and therefore, the impact of DNI variability. Additionally, $F_{Reforecast}$ can further enhance accuracy to reduce required reserve allocation.

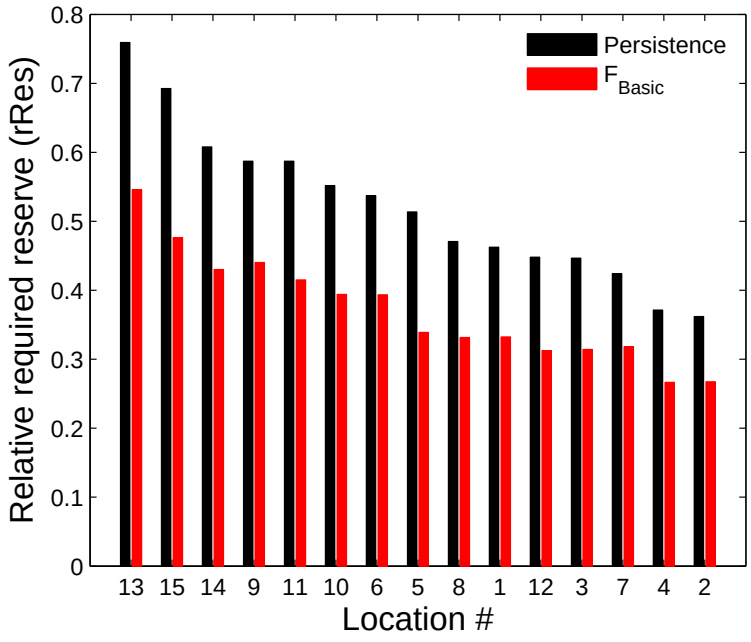

Figure 7.2: Bar plot for relative required reserve allocation for persistence and F_{Basic} for the location #s in figure 6.1. Bars are normalized to the local mean DNI values. F_{Basic} reduces the required reserves to balance resource uncertainty for CSP at all locations.

7.4 Summary

This chapter shows the benefits of DNI forecasts for the integration of CSP with two examples: value of information and reduction in required reserve allocation. The value of information analysis for the three discussed day-ahead DNI forecasting models showed that DNI forecasting accuracy is not necessarily promoting the highest revenue for a CSP plants. However, the best performing forecast increases revenue $19-22\%$ over the lowest performing forecast under current market conditions. Several market regulations and associated optimized bidding strategies allow to increase revenue with biased forecast submission. These results are consistent with previous findings form [71] for PV generated power. While current interconnection rules are mainly in place to promote renewable energy generation, we expect increasing penalization for discrepancies between scheduled and delivered energy with increasing grid penetration of intermittent sources. It could be shown that accurate day-ahead DNI forecasting becomes crucial with the implementation of high penalization of biased or inaccurate day-ahead market bids. Our DNI forecast is able to mitigate uncertainty and allows for increased revenue. Furthermore, CSP plants profit from market regulations allowing to update capacity bids without penalization. The required relative reserve for the reliable operation of the power grid is low for locations with high yearly yields. They can be reduced further with the proposed forecasting methods. On average, 28.6% lower relative reserves are required when the NWP based DNI forecast is deployed. Hence, the uncertainty introduced by concentrated solar power on day-ahead electricity trading is lower than previously estimated.

Note: This chapter contains work, previously published in:

- L. Nonnenmacher, A. Kaur, C. F. M. Coimbra, "Day-Ahead Resource Forecasting for Concentrated Solar Power Integration", (submitted), *Renewable Energy*, Apr. 2015.

- L. Nonnenmacher, A. Kaur, C. F. M. Coimbra, "Benchmarking and Valuation of Day-Ahead Forecasts for Direct Normal Irradiance", (submitted), *Solar Energy*, Oct. 2014.

Chapter 8

Conclusions

The experimental part of this dissertation covers the assessment of ground truth solar irradiance data with a strong focus on the acquisition of ground truth DNI. Based on the acquired data and strict quality controls, a remote sensing based irradiance model was evaluated with regards to DNI and its variability. The evaluated remote sensing model is crucial for the assessment of the solar resource and associated siting and sizing decisions for solar plants. It was shown that the satellite based assessment represents well the magnitude of DNI and its variability, with a tendency to overestimate small ramps. However, the errors for DNI are larger than for GHI due to larger range of values and the higher impact of aerosol fluctuations.

After the verification of the irradiance models, a solar forecasting method was proposed to cover forecast horizons 1 to 3 hours ahead as a strategy to mitigate the uncertainty of GHI. This intra-day forecast is based on freely available, near real time, pre-processed satellite images. Cloud movement is identified and extrapolated based on an optical flow algorithm, applied between two frames to determine the velocity vector field. The quality of the forecasts depends on the accuracy of the satellite-to-irradiance model. Therefore, ground measurements were used to develop a novel, lookup-table based satellite-to-irradiance model that outperforms the linear modeling approach. Satellite based intra-day forecasts are capable of reducing the uncertainty in the GHI resource. This was validated for San Diego, California, a highly variable solar micro-climate at the coast of the Pa-

cific Ocean. The validation was based on the images from the currently deployed GOES-West and East satellites. NASA schedules the space launch of the next generation of GOES satellites for the first quarter of 2016 and operational availability of next-generation satellite images for 2017. These new satellite images will have 5 minute temporal and sub-kilometer spatial resolution. We expect additional gains in forecast accuracy with the availability of the next-generation images as an input.

The operational grid interconnection of any power generator requires to strictly obey generation schedules. In most jurisdictions, the driving market clearing prices are decided based on the placement of a day-ahead market bids from all market participants. Hence, large-scale grid integration of solar generators requires day-ahead generation forecasts. For output scheduling of photovoltaic generators, NWP based GHI predictions are readily available. CSP technologies, relying on DNI, lack this option since most operational NWP currently do not include DNI as a forecast output. To fill in this gap, we proposed an accurate, globally valid, day-ahead DNI forecast to improve the accuracy of power bids from CSP generators. We quantify the monetary value of the reduction in uncertainty under three different market and settling scenarios with and without penalties. Our finding include that day-ahead forecasting of the solar resource significantly reduces the uncertainty in power output and can increase revenue of CSP plants. The good performance was validated for over 20 locations with high and medium potential for CSP in the Southwestern United States. Additionally, we showed that the impact of variability and uncertainty on the power grid, caused by large scale CSP deployment, can be mitigated through spatially distributed siting of CSP plants. This lowers the RMSE of predicted DNI time series from an average of 249 Wm^{-2} to 147 Wm^{-2}. With increasing accuracy of improved NWP cloud cover predictions, we expect that the accuracy of our proposed DNI forecasting model also increases. In short summary, we showed that a combination of optimized siting and solar forecasting are feasible technical solutions to significantly mitigate the uncertainty in power output from solar generators.

Bibliography

[1] Badescu, V. Modeling solar radiation at the earth surface. *Springer* (2008).

[2] Baharoon, D. A., Rahman, H. A., Omar, W. Z. W., and Fadhl, S. O. Historical development of concentrating solar power technologies to generate clean electricity efficiently a review. *Renewable and Sustainable Energy Reviews 41*, 0 (2015), 996 – 1027.

[3] Batlles, F. J., Rubio, M. A., Tovar, J., Olmo, F. J., and Alados-Arboledas, L. Empirical modeling of hourly direct irradiance by means of hourly global irradiance. *Energy 25*, 7 (2000), 675–688.

[4] Beyer, H., Costanzo, C., and Heinemann, D. Modifications of the heliosat procedure for irradiance estimates from satellite images. *Solar Energy 56*, 3 (1996), 207 – 212.

[5] Black, M. J., and Anandan, P. The robust estimation of multiple motions: Parametric and piecewise-smooth flow fields. *Computer vision and image understanding 63*, 1 (1996), 75–104.

[6] Bosch, J. L., Zheng, Y., and Kleissl, J. Deriving cloud velocity from an array of solar radiation measurements. *Solar Energy 87*, 0 (2013), 196 – 203.

[7] Breitkreuz, H., Schroedter-Homscheidt, M., Holzer-Popp, T., and Dech, S. Short-range direct and diffuse irradiance forecasts for solar energy applications based on aerosol chemical transport and numerical weather modeling. *Journal of Applied Meteorology & Climatology 48*, 9 (2009).

[8] Bruhn, A., Weickert, J., and Schnrr, C. Lucas/kanade meets horn/schunck: Combining local and global optic flow methods. *International Journal of Computer Vision 61* (2005), 211–231.

[9] Campbell Scientific, Inc. *App. Note Code: 2RA-A - Eppley PSP Precision Spectral Pyranometer*, 2001.

[10] Cano, D., Monget, J. M., Albuisson, M., Guillard, H., Regas, N., and Wald, L. A method for the determination of the global solar radiation from meteorological satellite data. *Solar Energy 37*, 1 (1986), 31 – 39.

[11] Channon, S. W., and Eames, P. C. The cost of balancing a parabolic trough concentrated solar power plant in the spanish electricity spot markets. *Solar Energy 110*, 0 (2014), 83 – 95.

[12] Chow, C. W. Intra-hour forecasting with a total sky imager at the UC San Diego solar energy testbed. *Solar Energy 85*, 11 (2011), 2881–2893.

[13] Chow, C. W., Urquhart, B., Lave, M., Dominguez, A., Kleissl, J., Shields, J., and Washom, B. Intra-hour forecasting with a total sky imager at the UC San Diego solar energy testbed. *Solar Energy 85*, 11 (2011), 2881–2893.

[14] Chowdhury, B. H., and Rahman, S. Forecasting sub-hourly solar irradiance for prediction of photovoltaic output. In *19th IEEE Photovoltaic Specialists Conference* (1987), pp. 171–176.

[15] Chu, Y., Pedro, H. T. C., and Coimbra, C. F. M. Hybrid intra-hour DNI forecasts with sky image processing enhanced by stochastic learning. *Solar Energy 98, Part C* (2013), 592 – 603.

[16] Collet, C., Quinquis, A., and Boucher, J. M. Cloudy sky velocity estimation based on optical flow estimation leading with an entropy criterion. In *Pattern Recognition, 1992. Vol.III. Conference C: Image, Speech and Signal Analysis, Proceedings., 11th IAPR International Conference on* (1992), pp. 160–163.

[17] Costa, A., Crespo, A., Navarro, J., Lizcano, G., Madsen, H., and Feitosa, E. A review on the young history of the wind power short-term prediction. *Renewable and Sustainable Energy Reviews 12*, 6 (2008), 1725 – 1744.

[18] Dallmer-Zerbe, K., Bucher, M. A., Ulbig, A., and Andersson, G. Assessment of capacity factor and dispatch flexibility of concentrated solar power units. In *PowerTech (POWERTECH), 2013 IEEE Grenoble* (June 2013), p. 1.

[19] Denholm, P., Wan, Y. H., Hummon, M., and Mehos, M. An analysis of concentrating solar power with thermal energy storage in a california 33% renewable scenario. *Contract 303* (2013), 275–3000.

[20] Denholm, P., Wan, Y. H., Hummon, M., and Mehos, M. The value of {CSP} with thermal energy storage in the western united states. *Energy Procedia 49* (2014), 1622 – 1631. Proceedings of the SolarPACES 2013 International Conference.

[21] Djebbar, R., Morris, R., Thevenard, D., Perez, R., and Schlemmer, J. Assessment of SUNY version 3 global horizontal and direct normal solar irradiance in canada. *Energy Procedia 30*, 0 (2012), 1274–1283.

[22] Dong, Z., Yang, D., Reindl, T., and Walsh, W. Short-term solar irradiance forecasting using exponential smoothing state space model. *Energy 55* (2013), 1104 – 1113.

[23] Endlich, R., and Wolf, D. Automatic cloud tracking applied to goes and meteosat observations. *Journal of Applied Meteorology 20*, 3 (1981), 309–319.

[24] Escrig, H., Batlles, F., Alonso, J., Baena, F., Bosch, F., Salbidegoitia, I., and Burgaleta, J. Cloud detection, classification and motion estimation using geostationary satellite imagery for cloud cover forecast. *Energy 55* (2013), 853 – 859.

[25] Ghonima, M. S., Urquhart, B., Chow, C. W., Shields, J. E., Cazorla, A., and Kleissl, J. A method for cloud detection and opacity classification based on ground based sky imagery. *Atmospheric Measurement Techniques 5*, 11 (2012), 2881–2892.

[26] Gilliam, H. *Weather of the San Francisco Bay Region*, vol. 63. Univ of California Press, 2002.

[27] Girodo, M., Mueller, R. W., and Heinemann, D. Influence of three-dimensional cloud effects on satellite derived solar irradiance estimation - First approaches to improve the Heliosat method. *Solar Energy 80*, 9 (2006), 1145–1159.

[28] Goh, T. N., and Tan, K. J. Stochastic modeling and forecasting of solar radiation data. *Solar Energy 19*, 6 (1977), 755 – 757.

[29] Gueymard, C. Aerosol turbidity derivation from broadband irradiance measurements: Methodological advances and uncertainty analysis. In *ASES Solar 2013 Conference* (2013).

[30] Gueymard, C. A. The suns total and spectral irradiance for solar energy applications and solar radiation models. *Solar Energy 76*, 4 (2004), 423 – 453.

[31] Gueymard, C. A. REST2: High-performance solar radiation model for cloudless-sky irradiance, illuminance, and photosynthetically active radiation validation with a benchmark dataset. *Solar Energy 82*, 3 (2008), 272 – 285.

[32] Gueymard, C. A. Temporal variability in direct and global irradiance at various time scales as affected by aerosols. *Solar Energy 86*, 12 (2012), 3544 – 3553.

[33] Gueymard, C. A. Temporal variability in direct and global irradiance at various time scales as affected by aerosols. *Solar Energy 86*, 12 (2012), 3544 – 3553.

[34] Gueymard, C. A. A review of validation methodologies and statistical performance indicators for modeled solar radiation data: Towards a better bankability of solar projects. *Renewable and Sustainable Energy Reviews 39*, 0 (2014), 1024 – 1034.

[35] Gueymard, C. A., and Wilcox, S. M. Assessment of spatial and temporal variability in the US solar resource from radiometric measurements and predictions from models using ground-based or satellite data. *Solar Energy 85*, 5 (2011), 1068 – 1084.

[36] Guillot, E. M. Haar, T. H. V., Forsythe, J. M., and Fletcher, S. J. Evaluating satellite-based cloud persistence and displacement nowcasting techniques over complex terrain. *Weather and Forecasting 27* (2012), 502514.

[37] Hammer, A., Heinemann, D., Hoyer, C., Kuhlemann, R., Lorenz, E., Müller, R., and Beyer, H. G. Solar energy assessment using remote sensing technologies. *Remote Sensing of Environment 86*, 3 (2003), 423–432.

[38] Hammer, A., Heinemann, D., Lorenz, E., and Luckehe, B. Short-term forecasting of solar radiation: a statistical approach using satellite data. *Solar Energy 67* (1999), 139–150.

[39] Handa, Y., Kurtz, B., Nguyen, D., Urquhart, B., Chow, C., Ghonima, M., and Kleissl, J. Solar irradiance forecasting using a ground-based sky imager developed at UC san diego. *Solar Energy 103*, 0 (2014), 502 – 524.

[40] Hanna, R., Kleissl, J., Nottrott, A., and Ferry, M. Energy dispatch schedule optimization for demand charge reduction using a photovoltaic-battery storage system with solar forecasting. *Solar Energy 103* (2014), 269 – 287.

[41] Heck, P. W., and Takle, E. S. Objective forecasts of solar radiation and temperature. *Iowa State Journal of Research 62* (1987), 29–42.

[42] Heinemann, D., Lorenz, E., and Girodo, M. Solar irradiance forecasting for the management of solar energy systems. *Energy and Semiconductor Research Laboratory, Energy Meteorology Group, Oldenburg University* (2006).

[43] Hicks, B. B., DeLuisi, J. J., and Matt, D. R. The noaa integrated surface irradiance study (isis)-a new surface radiation monitoring program. *Bulletin Of The American Meteorological Society 77*, 12 (1996), 2857–2864.

[44] Hoff, T. E., and Perez, R. Modeling PV fleet output variability. *Solar Energy 86*, 8 (2012), 2177–2189.

[45] Holttinen, H., Milligan, M., Ela, E., Menemenlis, N., Dobschinski, J., Rawn, B., Bessa, R. J., Flynn, D., Gomez-Lazaro, E., and Detlefsen, N. K. Methodologies to determine operating reserves due to increased wind power. *Sustainable Energy, IEEE Transactions on 3*, 4 (2012), 713–723.

[46] Horn, B. K., and Schunck, B. G. Determining optical flow. *Artificial intelligence 17*, 1 (1981), 185–203.

[47] Ineichen, P. Comparison of eight clear sky broadband models against 16 independent data banks. *Solar Energy 80*, 4 (2006), 468–478.

[48] Ineichen, P. Comparison and validation of three global-to-beam irradiance models against ground measurements. *Solar Energy 82*, 6 (2008), 501 – 512.

[49] Ineichen, P. Long term satellite global, beam and diffuse irradiance validation. *Energy Procedia 48*, 0 (2014), 1586 – 1596. Proceedings of the 2nd International Conference on Solar Heating and Cooling for Buildings and Industry (SHC 2013).

[50] Ineichen, P., and Perez, R. A new airmass independent formulation for the Linke turbidity coefficient. *Solar Energy 73*, 3 (2002), 151–157.

[51] Inman, R. H., Edson, J. G., and Coimbra, C. F. M. Impact of local broadband turbidity estimation on forecasting clear sky direct normal irradiance. *Solar Energy 110*, 0 (2015), 1. submitted.

[52] Inman, R. H., Pedro, H. T. C., and Coimbra, C. F. M. Solar forecasting methods for renewable energy integration. *Progress in Energy and Combustion Science 39*, 6 (2013), 535 – 576.

[53] Jensenius, J. Insolation forecasting. *Solar Resources* (1989).

[54] Jensenius, J., and Cotton, G. F. The development and testing of automated solar energy forecasts based on the model output statistics (mos) technique. In *1st Workshop on terrestrial solar resource forecasting and on use of satellites for terrestrial solar resource assessment, Washington, DC* (1981).

[55] Journe, M., and Bertrand, C. Quality control of solar radiation data within the RMIB solar measurements network. *Solar Energy 85*, 1 (2011), 72 – 86.

[56] Jung, J., and Broadwater, R. P. Current status and future advances for wind speed and power forecasting. *Renewable and Sustainable Energy Reviews 31*, 0 (2014), 762 – 777.

[57] Kaur, A., Pedro, H. T. C., and Coimbra, C. F. M. Impact of onsite solar generation on system load demand forecast. *Energy Conversion and Management 75* (2013), 701 – 709.

[58] Kaur, A., Pedro, H. T. C., and Coimbra, C. F. M. Ensemble re-forecasting methods for enhanced power load prediction. *Energy Conversion and Management 80*, 0 (2014), 582 – 590.

[59] Kern, E.C.J. and Augustyn, J. and Bing J. *Rotating Shadowband Radiometer*, 2008. revised February 1, 2008.

[60] Kottek, M.and Grieser, J., Beck, C., Rudolf, B., and Rubel, F. World map of the koppen-geiger climate classification updated. *Meteorologische Zeitschrift 15*, 3 (2006), 259–264.

[61] Kraas, B., Schroedter-Homscheidt, M., and Madlener, R. Economic merits of a state-of-the-art concentrating solar power forecasting system for participation in the spanish electricity market. *Solar Energy 93* (2013), 244 – 255.

[62] Lara-Fanego, V., Ruiz-Arias, J. A., Pozo-Vázquez, D., Santos-Alamillos, F. J., and Tovar-Pescador, J. Evaluation of the WRF model solar irradiance forecasts in andalusia (southern spain). *Solar Energy 86*, 8 (2012), 2200–2217.

[63] Law, E. W., Prasad, A. A., Kay, M., and Taylor, R. A. Direct normal irradiance forecasting and its application to concentrated solar thermal output forecasting a review. *Solar Energy 108*, 0 (2014), 287 – 307.

[64] Leung, I. J. H., and Jordan, J. E. Image processing for weather satellite cloud segmentation. In *Electrical and Computer Engineering, 1995. Canadian Conference on* (1995), vol. 2, IEEE, pp. 953–956.

[65] Ljung, L. *System Identification: Theory for the User*. No. ISBN 0-13-881640-9 025. Prentice Hall PTR, New Jersey, USA, 1999.

[66] Lohmann, S., Schillings, C., Mayer, B., and Meyer, R. Long-term variability of solar direct and global radiation derived from ISCCP data and comparison with reanalysis data. *Solar Energy 80*, 11 (2006), 1390 – 1401.

[67] Lorenz, E., Heinemann, D., Wickramarathne, H., Beyer, H. G., and Bofinger, S. Forecast of ensemble power production by grid-connected PV systems. In *Proceedings of the 20th European PV Conference, Milano, Italy* (2007).

[68] Lorenz, E., Remund, J., Müller, S. C., Traunmüller, W., Steinmaurer, G., Pozo, D., , Ruiz-Arias, J. A., Lara-Fanego, V., Ramirez, L., Romeo, M. G., Kurz, C., Pomares, L. M., and Guerrero, C. G. Benchmarking of different approaches to forecast solar irradiance. In *24th European photovoltaic solar energy conference* (2009), pp. pp. 21–25.

[69] Louche, A., Notton, G., Poggi, P., and Simonnot, G. Correlations for direct normal and global horizontal irradiation on a french mediterranean site. *Solar Energy 46*, 4 (1991), 261 – 266.

[70] Louche, A., Simonnot, G., Iqbal, M., and Mermier, M. Experimental verification of some clear-sky insolation models . *Solar Energy 41*, 3 (1988), 273 – 279.

[71] Luoma, J., Mathiesen, P., and Kleissl, J. Forecast value considering energy pricing in california. *Applied Energy 125* (2014), 230 – 237.

[72] Marquez, R., and Coimbra, C. F. M. Forecasting of Global and Direct Solar Irradiance Using Stochastic Learning Methods, Ground Experiments and the NWS Database. *Solar Energy 85*, 5 (2011), 746–756.

[73] Marquez, R., and Coimbra, C. F. M. Intra-hour DNI forecasting based on cloud tracking image analysis. *Solar Energy 91*, 0 (2013), 327 – 336.

[74] Marquez, R., and Coimbra, C. F. M. Intra-Hour DNI Forecasting Methodology Based on Cloud Tracking Image Analysis. *Solar Energy 91*, 0 (2013), 327–336.

[75] Marquez, R., and Coimbra, C. F. M. Proposed Metric for Evaluation of Solar Forecasting Models. *ASME Journal of Solar Energy Engineering 135*, 1 (2013), 0110161–0110169.

[76] Marquez, R., Pedro, H. T. C., and Coimbra, C. F. M. Hybrid solar forecasting method uses satellite imaging and ground telemetry as inputs to anns. *Solar Energy 92* (2013), 176–188.

[77] Martins, F. R., Pereira, E. B., and Abreu, S. L. Satellite-derived solar resource maps for brazil under SWERA project. *Solar Energy 81*, 4 (2007), 517 – 528.

[78] Marvin, C. F., and Kimball, H. H. Solar radiation and weather forecasting. *Journal of the Franklin Institute 202*, 3 (1926), 273 – 306.

[79] Mathiesen, P., Collier, C., and Kleissl, J. A high-resolution, cloud-assimilating numerical weather prediction model for solar irradiance forecasting. *Solar Energy 92* (2013), 47 – 61.

[80] Mathiesen, P., and Kleissl, J. Evaluation of numerical weather prediction for intra-day solar forecasting in the continental united states. *Solar Energy 85*, 5 (2011), 967–977.

[81] Mathiesen, P., and Kleissl, J. Evaluation of numerical weather prediction for intra-day solar forecasting in the continental united states. *Solar Energy 85*, 5 (2011), 967–977.

[82] Mehos, M., and Owens, B. An analysis of siting opportunities for concentrating solar power plants in the southwestern united states. In *World Renewable Energy Conference VIII, Denver, Colo* (2004), p. 1.

[83] Milbrandt, A. R., Heimiller, D. M., Perry, A. D., and Field, C. B. Renewable energy potential on marginal lands in the united states. *Renewable and Sustainable Energy Reviews 29* (2014), 473 – 481.

[84] Montes, M. J., Abnades, A., and Martnez-Val, J. M. Performance of a direct steam generation solar thermal power plant for electricity production as a function of the solar multiple. *Solar Energy 83*, 5 (2009), 679 – 689.

[85] Mueller, R. W., Dagestad, K. F., Ineichen, P., Schroedter-Homscheidt, M., Cros, S., Dumortier, D., Kuhlemann, R., Olseth, J., Piernavieja, G., Reise, C., Wald, L., and Heinemann, D. Rethinking satellite-based solar irradiance modeling: The SOLIS clear-sky module. *Remote Sensing of Environment 91*, 2 (2004), 160–174.

[86] Mueller, R. W., Matsoukas, C., Gratzki, A., Behr, H. D., and Hollmann, R. The CM-SAF operational scheme for the satellite based retrieval of solar surface irradiance a LUT based eigenvector hybrid approach. *Remote Sensing of Environment 113*, 5 (2009), 1012 – 1024.

[87] Nakariyakul, S. Fast spatial averaging: an efficient algorithm for 2d mean filtering. *The Journal of Supercomputing 65*, 1 (2013), 262–273.

[88] Nikitidou, E., Kazantzidis, A., and Salamalikis, V. The aerosol effect on direct normal irradiance in europe under clear skies. *Renewable Energy 68*, 0 (2014), 475 – 484.

[89] Nonnenmacher, L. Implementing a solar radiation measurement network in california and data quality assessment.

[90] Nonnenmacher, L., and Coimbra, C. F. M. Streamline-based method for intra-day solar forecasting through remote sensing. *Solar Energy 108*, 0 (2014), 447 – 459.

[91] Nonnenmacher, L., Kaur, A., and Coimbra, C. F. M. Benchmarking and valuation of day-ahead forecasts for direct normal irradiance. *Solar Energy, submittend Oct. 2014 0* (2014), 0 – 0.

[92] Nonnenmacher, L., Kaur, A., and Coimbra, C. F. M. Verification of the SUNY direct normal irradiance model with ground measurements. *Solar Energy 99* (2014), 246 – 258.

[93] Nottrott, A., and Kleissl, J. Validation of the NSRDB-SUNY global horizontal irradiance in california. *Solar Energy 84*, 10 (2010), 1816 – 1827.

[94] Ohtake, H., Shimose, K. I., Fonseca, J. G. D. S., Takashima, T., Oozeki, T., and Yamada, Y. Accuracy of the solar irradiance forecasts of the japan meteorological agency mesoscale model for the kanto region, japan. *Solar Energy 98, Part B* (2013), 138 – 152.

[95] Pedro, H., and Coimbra, C. F. M. Assessment of forecasting techniques for solar power production with no exogenous inputs. *Solar Energy 86*, 7 (2012), 2017–2028.

[96] Pelland, S., Galanis, G., and Kallos, G. Solar and photovoltaic forecasting through post-processing of the global environmental multiscale numerical weather prediction model. *Progress in Photovoltaics: Research and Applications 21*, 3 (2013), 284–296.

[97] Pereira, E. B., Martins, F. R., Abreu, S. L., Couto, P., Stuhlmann, R., and Colle, S. Effects of burning of biomass on satellite estimations of solar irradiation in brazil. *Solar Energy 68*, 1 (2000), 91 – 107.

[98] Perez, R., Ineichen, P., Kmiecik, M., Moore, K., Renne, D., and George, R. Producing satellite-derived irradiances in complex arid terrain. *Solar Energy 77*, 4 (2004), 367–371.

[99] Perez, R., Ineichen, P., Maxwell, E. L., Seals, R. D., and Zelenka, A. Dynamic global to direct irradiance conversion models. *ASHRAE Transactions-Research Series* (1992), 354–369.

[100] Perez, R., Ineichen, P., Moore, K., Kmiecik, M., Chain, C., George, R., and Vignola, F. A new operational model for satellite-derived irradiances: description and validation. *Solar Energy 73*, 5 (2002), 307–317.

[101] Perez, R., Kivalov, S., Schlemmer, J., Hemker, K., Renne, D., and Hoff, T. E. Validation of short and medium term operational solar radiation forecasts in the US. *Solar Energy 84*, 5 (2010), 2161–2172.

[102] Perez, R., Lorenz, E., Pelland, S., Beauharnois, M., Van Knowe, G., Hemker, K. J., Heinemann, D., Remund, J., Mller, S. C., Traunmller, W., Steinmauer, G., Pozo, D., Ruiz-Arias, J. A., Lara-Fanego, V., Ramirez-Santigosa, L., Gaston-Romero, M., and Pomares, L. M. Comparison of numerical weather prediction solar irradiance forecasts in the us, canada and europe. *Solar Energy 94* (2013), 305 – 326.

[103] Perez, R., Moore, K., Wilcox, S., Renn, D., and Zelenka, A. Forecasting solar radiation preliminary evaluation of an approach based upon the national forecast database. *Solar Energy 81*, 6 (2007), 809 – 812.

[104] Pfenninger, S., Gauché, P., Lilliestam, J., Damerau, K., Wagner, F., and Patt, A. Potential for concentrating solar power to provide baseload and dispatchable power. *Nature Climate Change 4*, 8 (2014), 689–692.

[105] Prasad, A. A., Robert, A. T., and Kay, M. Assessment of direct normal irradiance and cloud connections using satellite data over australia. *Applied Energy 143*, 0 (2015), 301 – 311.

[106] Quesada-Ruiz, S., Chu, Y., Tovar-Pescador, J., Pedro, H. T. C., and Coimbra, C. F. M. Cloud-tracking methodology for intra-hour {DNI} forecasting. *Solar Energy 102*, 0 (2014), 267 – 275.

[107] Remund, J., Wald, L., Lefèvre, M., Ranchin, T., and Page, J. H. Worldwide linke turbidity information. In *Proceedings of ISES Solar World Congress 2003* (2003), vol. 400.

[108] Reno, M. J., Hansen, C. W., and Stein, J. S. Global horizontal irradiance clear sky models: implementation and analysis. *SAND2012-2389, Sandia National Laboratories, Albuquerque, NM* (2012).

[109] Ronzio, D. A., Collino, E., and Bonelli, P. A survey on different radiative and cloud schemes for the solar radiation modeling. *Solar Energy 98, Part B* (2013), 153 – 166.

[110] Schillings, C., Mannstein, H., and Meyer, R. Operational method for deriving high resolution direct normal irradiance from satellite data. *Solar Energy 76*, 4 (2004), 475 – 484.

[111] Shi, H. Cloud movement detection for satellite images. In *Signal Processing Proceedings, 1998. ICSP '98. 1998 Fourth International Conference on* (1998), vol. 2, pp. 982–985 vol.2.

[112] Stein, J., Hansen, C., and Reno, M. J. The variability index: A new and novel metric for quantifying irradiance and PV output variability. In *World Renewable Energy Forum* (2012).

[113] Stephens, G. L. The parameterization of radiation for numerical weather prediction and climate models. *Monthly Weather Review 112*, 4 (1984), 826–867.

[114] Stoddard, L., Abiecunas, J., and O'Connell, R. Economic, energy, and environmental benefits of concentrating solar power in california. Tech. rep., National Renewable Energy Laboratory (United States), 2006.

[115] Sun, D., Roth, S., and Black, M. J. Secrets of optical flow estimation and their principles. In *Computer Vision and Pattern Recognition (CVPR), 2010 IEEE Conference on* (2010), IEEE, pp. 2432–2439.

[116] Sun, D., Roth, S., and Black, M. J. A quantitative analysis of current practices in optical flow estimation and the principles behind them. *International Journal of Computer Vision 106*, 2 (2014), 115–137.

[117] Sun, Z., and Liu, A. Fast scheme for estimation of instantaneous direct solar irradiance at the earths surface. *Solar Energy 98, Part B* (2013), 125 – 137.

[118] The Eppley Laboratory. *Normal Incidence Pyrheliometer, Model NIP.*

[119] The Eppley Laboratory. *Precision Spectral Pyranometer, Model PSP.*

[120] Troccoli, A., and Morcrette, J. J. Skill of direct solar radiation predicted by the ecmwf global atmospheric model over australia. *Journal of Applied Meteorology and Climatology 53*, 11 (2014), 2571–2588.

[121] Vignola, F., Harlan, P., Perez, R., and Kmiecik, M. Analysis of satellite derived beam and global solar radiation data. *Solar Energy 81*, 6 (2007), 768 – 772.

[122] Wendell, L. L., Wegley, H. L., and Verholek, M. G. Report from a working group meeting on wind forecasts for wecs operation. Tech. rep., Battelle Pacific Northwest Labs., Richland, WA (USA), 1978.

[123] Wiser, R., Barbose, G., and Holt, E. Supporting solar power in renewables portfolio standards: Experience from the united states. *Energy Policy 39*, 7 (2011), 3894 – 3905. Special Section: Renewable energy policy and development.

[124] Wittmann, M., Breitkreuz, H., Schroedter-Homscheidt, M., and Eck, M. Case studies on the use of solar irradiance forecast for optimized operation strategies of solar thermal power plants. *Selected Topics in Applied Earth Observations and Remote Sensing, IEEE Journal of 1* (2008), 18–27.

[125] Wu, Q. A correlation-relaxation-labeling framework for computing optical flow-template matching from a new perspective. *Pattern Analysis and Machine Intelligence, IEEE Transactions on 17*, 9 (Sep 1995), 843–853.

[126] Yankee Environmental Systems, Inc. *Bulletin MFRSR-7: Multi-Filter Rotating Shadowband Radiometer Model MFR-7*, 2004.

[127] Younes, S., Claywell, R., and Muneer, T. Quality control of solar radiation data: Present status and proposed new approaches. *Energy 30*, 9 (2005), 1533 – 1549.

[128] Zamo, M., Mestre, O., Arbogast, P., and Pannekoucke, O. A benchmark of statistical regression methods for short-term forecasting of photovoltaic electricity production. part ii: Probabilistic forecast of daily production. *Solar Energy 105* (2014), 804 – 816.